



Ville Nieminen

Characterization of hydromechanical properties of a rock fracture using numerical modelling

Thesis submitted for examination for the degree of Master of Science in Technology.

Espoo 20.05.2022

Thesis supervisor: Prof. Mikael Rinne

Thesis instructors: D.Sc. (Tech) Lauri Uotinen, M.Sc. (Tech) Masoud Torkan



Author Ville Nieminen

Title of thesis Characterization of hydromechanical properties of rock fracture using numerical modelling

Major/minor Geoengineering

Code ENG23

Thesis supervisor Prof. Mikael Rinne

Thesis advisor(s) D. Sc. (Tech) Lauri Uotinen, M. Sc. (Tech) Masoud Torkan

Date 20.05.2022

Number of pages 71

Language English

Abstract

The hydromechanical processes of a single rock fracture are dependent on the properties of that single rock fracture as well as the properties of the rock fractures that are connected to it, and their geometry, orientation and the effective stress of the fracture walls. Hydromechanical properties of a single rock fracture are governed by several parameters such as contact area, roughness, tortuosity, aperture, channeling, matedness, sample sizes, normal stress, flow regime, and flow boundary conditions.

Numerical modelling was used to compare the influences of roughness, aperture, water pressure, and different flow boundary conditions on fluid flow in an artificial granite fracture. Comprehensive fluid flow analyses were made to better understand the flow behaviour, including the streamlines, flow velocities and inner water pressure distributions. A simulation model for fluid flow in a single rough fracture was developed with the COMSOL Multiphysics finite element method software. The resulting model was numerically simulated with COMSOL using the Navier-Stokes equations.

In this thesis, 20 fluid flow simulations were performed on fracture model created from photogrammetry of rock block with the size of 250 mm × 250 × 110 mm containing artificial tensile fracture. Laminar fluid flow inside the fracture was simulated with fluid flow through x- and y-axis at increasing water pressure level at normal stress conditions of 0 MPa. Simulated water pressures were from 5 kPa to 50 kPa with 5 kPa interval. The numerical model was successfully verified against experimental laboratory work.

The numerical simulation results show that the relationship between water pressure gradient and the flow rate is nonlinear indicating turbulent flow behaviour. The channelling effect of the fluid flow as well as the pressure distribution along the fracture increase with the increase of water pressure. The growth of fluid flow velocity inside the fracture with the increase of water pressure is nonlinear and the growth rate of the fluid flow velocity decreases as the inlet water pressure increases.

Comparison between the numerical modelling results and the experimental solution confirms that the 3D roughness geometry has a crucial role in defining the transmissivity, especially for nonlinear flow. The presented method can be used to characterize flow properties of fractured rock and in evaluating different methods and implementation of underground rock engineering applications.

Keywords Aperture, rough fracture, fluid flow, flow simulation, COMSOL Multiphysics



Tekijä Ville Nieminen

Työn nimi Kallioraon hydromekaanisten ominaisuuksien arviointi numeerisen mallinnuksen avulla

Koulutusohjelma Geoengineering

Koodi ENG23

Työn valvoja Prof. Mikael Rinne

Työn ohjaaja(t) TkT Lauri Uotinen, DI Masoud Torkan

Päivämäärä 20.05.2022

Sivumäärä 71

Kieli Englanti

Tiivistelmä

Kalliorakoon vaikuttavat hydromekaaniset prosessit ovat riippuvaisia sen yksittäisen kallioraon ominaisuuksista sekä siihen liittyvien rakoverkostojen ominaisuuksista ja niiden geometriasta, suunnasta ja raon seinämiin vaikuttavista jännityksistä. Kallioraon hydromekaanisia ominaisuuksia säätelevät useat parametrit, kuten kosketuspinta-ala, karheus, mutkittelevuus, rakoavauma, kanavointi, koko, normaalijännitys, virtaustyyli ja virtauksen rajaolosuhteet.

Numeerista mallinnusta käytettiin tutkittaessa karheuden, rakoavauman, vedenpaineen ja erilaisten virtauksen rajaolosuhteiden vaikutuksia nesteen virtaukseen kallioraossa. Virtauslinjoja, virtausnopeuksia sekä raon sisäistä vedenpainejakaumaa käytettiin apuna tutkittaessa virtauksen käyttäytymistä kallioraossa. Simulointimalli kehitettiin COMSOL Multiphysics -elementtimenetelmäohjelmistolla ja malli simuloitiin numeerisesti käyttäen Navier-Stokes -yhtälöitä.

Tässä työssä muodostettiin 20 virtaussimulaatiota. Näytemateriaalina käytettiin 250 mm × 250 mm × 110 mm:n kokoista kivikuutiota, jonka halki kulki keinotekoinen kalliorako. Fotogrammetriaa käytettiin apuna mallin luomisessa. Laminaarinen nesteen virtaus kallioraon sisällä simuloitiin x- ja y-akselin suunnissa, nousevalla vedenpaineella, normaalijännityksen ollessa 0 Mpa. Simuloidut vedenpaineet olivat 5 kPa - 50 kPa, 5 kPa:n välein. Numeerinen malli tarkistettiin ja todennettiin laboratoriotutkimusten avulla.

Työn tulokset osoittavat, että vedenpainegradientin ja virtausnopeuden välinen suhde on epälineaarinen mikä näyttäisi osoittavan virteuksen olevan turbulenttista. Nesteen virtauksen kanavoimituminen sekä paineen jakautuminen kallioraon sisällä lisääntyvät vedenpaineen kasvaessa. Nesteen virtausnopeuden kasvu kallioraon sisällä vedenpaineen kasvaessa, on epälineaarista ja nesteen virtausnopeuden kasvunopeus laskee veden paineen kasvaessa.

Numeerisen mallinnuksen tulosten ja laboratoriotulosten vertailu vahvistaa, että kallioraon 3D-geometrialla on ratkaiseva rooli raon läpäisevyyden määrittelyssä, erityisesti epälineaarisessa virtauksessa. Työssä esitetyn menetelmän avulla voidaan luokitella rakoilleen kiven virtausominaisuuksia sekä arvioida erilaisia kalliotekniikan menetelmiä ja toteutusta.

Avainsanat Rakoavauma, karkea rako, virtaussimulointi, nesteen virtaus, COMSOL Multiphysics



**Aalto University
School of Engineering**

Aalto University, P.O. BOX 11000, 00076 AALTO
www.aalto.fi

Abstract of master's thesis

Foreword

This Master's thesis is part of ongoing RAKKA research project that studies fluid flow in fractured rock mass. The work for his thesis started with experimental laboratory work. Gradually, the emphasis of the thesis shifted towards numerical modelling, and after few iterations of the topic, the idea of fluid flow simulation was chosen as main study approach.

I would like to thank my instructors Dr. Lauri Uotinen and doctoral candidate Masoud Torkan for their guidance and valuable insights throughout the whole work. Also, Masouds work with the experimental tests was crucial. I would also like to acknowledge Dr. Alireza Baghbanan, who was the first one to introduce me to the subject, although the initial idea was slightly altered during the work. I'd like to give special thanks to my supervisor, Prof. Mikael Rinne for suggestions, comments and pushing me to finish the work.

The flexibility and support of my employers, AFRY Finland Oy and Labroc Oy, were very important during my studies and I am grateful for it. Finally, big thanks to my family and friends for support and encouragement.

Helsinki May 20th 2022

Ville Nieminen

Table of Contents

Foreword.....	5
Table of Contents.....	6
Symbols and abbreviations	7
1 Introduction	9
1.1 Background	9
1.2 Scope of the research	10
2 Physical background	12
2.1 Laminar and turbulent flow.....	12
2.2 Governing equations	13
3 Theoretical framework of fractured rocks.....	14
3.1 Definitions.....	14
3.2 Different types of fracture aperture.....	15
3.3 Variations in fracture aperture	16
3.4 Calculating and measuring the fracture aperture	16
4 Hydromechanical coupling in fractured rocks	17
4.1 Hydromechanical coupling	17
4.2 Hydromechanical behaviour of rock fractures	18
5 Research material and methods.....	20
5.1 Methodology	20
5.2 Research material and sample preparation.....	20
5.3 Photogrammetry	21
5.4 Water flow tests.....	22
6 COMSOL Multiphysics simulation model	26
6.1 Model tree and definitions	26
6.2 Geometry	27
6.3 Materials.....	41
6.4 Physical model	45
6.5 Meshing.....	49
6.6 Solver	51
7 Simulation results.....	52
7.1 Validation of the numerical simulation model.....	52
7.2 Physical and hydraulic aperture	54
7.3 Flow velocity.....	55
7.4 Streamlines.....	55
7.5 Pressure contours	59
8 Conclusion.....	63
References.....	65
Appendix.....	70
A Tabulated results	70

Symbols and abbreviations

Symbol	Explanation	Unit
a	Forchheimer viscous coefficient	$\text{kg/m}^5\text{s}$
b	Forchheimer inertial coefficient	kg/m^8
ρ	density	kg/m^3
μ	fluid viscosity	$\text{Pa} \cdot \text{s}$
∇P	pressure gradient	Pa/m
Q	flow rate	m^3/s
e_h	hydraulic aperture	mm
β	nonlinear coefficient	-
w	width	m
L	length	m
u	flow velocity vector	-
P	fluid pressure	Pa
V	velocity of flow	m/s
K	coefficient of permeability	-
I	hydraulic gradient	-

Abbreviation	Explanation
2D	Two dimensional
3D	Three dimensional
FEM	Finite element method
ISRM	International Society for Rock Mechanics
JRC	Joint roughness coefficient
LVDT	Linear variable displacement transformer
NAPL	Non-aqueous phase liquid
N-S	Navier-Stokes equation
Re	Reynold's number
THMC	Thermo-hydro-mechanic-chemical

1 Introduction

1.1 Background

Fluid flow and the behaviour of the fluid flow with different transport systems in fractured bedrock is essential issue in underground rock engineering projects such as tunnel excavation, hydraulic engineering, geothermal exploitation (Zhao & Brown 1992, Jing 2003, Rutqvist & Stephansson 2003, Zhao et al. 2011, Zhang & Nemcik 2013, Zhao 2014, Develi & Babadagli 2015, Singh et al. 2015, Xiong et al. 2018). The flow of groundwater in fractured rock can be regarded as a critical problem when considering the usage of rock mass as a barrier to prevent radionuclides escaping from a geological nuclear repository. The basis of the representation of fluid flow behaviour in fractured bedrock is formed by the knowledge acquired from the study of single fractures. Rock fracture geometry, contact area, surface roughness, tortuosity, channelling, normal stress, fracture aperture, water pressure, flow regime and different flow boundary conditions among others, are key parameters affecting the hydromechanical properties of a single rock fracture. The bedrock in depth is under significant loading due to the weight of the overlying rock and tectonic movements. The stress state of the bedrock will change during time and the excavations and filling of the tunnels will cause changes in the stress state of the bedrock. These are aspects that should be taken consideration in underground rock engineering applications.

Figure 1 presents illustration of hydromechanical processes in a single rock fracture, that are related to water pressure in the fracture and to the fracture aperture. The changes in water pressure affect the rock mass by deforming it and causing variations in fracture aperture which in turn alters the fluid flow rate and water pressure. Fractured rock masses comprise intact rock blocks and fractures, which work as main pathways for fluid flow and fracture aperture can vary either due to closures induced by normal stress or openings or due to shear stress-induced dilations (Min et al. 2004). According to Rutqvist & Stephansson (2003), the hydromechanical coupling can be either indirect, where the applied stresses produce changes in the hydraulic properties of the rock or direct, where the applied stresses produce changes in fluid pressure (Figure 1). The indirect hydromechanical coupling can be seen as particularly important in fractured rock masses because stress-induced alterations in permeability can be up to several orders of magnitude and irretrievable (Min et al. 2004). Hydraulic properties depend on the mechanical loading conditions which means that the hydraulic characteristics are almost completely coupled to the mechanical behaviour of fractures (Noorishad & Tsang 1996, Lee & Cho 2002).



Figure 1. Hydromechanical processes in rock fractures (modified after Jing & Stephansson 2007).

The flow path of groundwater varies when the stress field in bedrock undergoes changes and on the other hand, groundwater alters the effective stress state in rock fractures. Fluid affects the stress state in the rock and thus can create new flow paths and the stress state affects to the opening and closing of the flow paths as well the fracture aperture. In other words, fluid pressure can open fractures and bed rock stress can close fractures. In this sense, the situation can be regarded as coupled hydromechanical problem. In terms of nuclear waste management, hydromechanical modelling is part of thermo-hydro-mechanic-chemical

(THMC) modelling. Coupled hydromechanical problem has a two-way connection so it can be viewed separately from temperature and chemical processes when not operating in immediate vicinity of the repository tunnels. The hydromechanical processes of a single rock joint are dependent on the properties of that single rock joint as well as the properties of the rock joints that are connected to it and their geometry, orientation and the effective stress of the fracture walls (Zimmermann & Main 2004).

Theoretical, empirical and experimental works have been carried out about the fluid flow in fractured rock masses and the effects of three-dimensional stress field to a fluid flow through rock fracture (e.g. Brown et al. 1998, Tsang & Witherspoon 1981, Schrauf & Evans 1986, Zimmerman et al. 1992, Detwiler et al. 2000, Li et al. 2008 and 2016, Ishibashi et al. 2015, Chen et al. 2017, Rong et al. 2016, Stoll et al. 2019, Wang et al. 2019). Still, Chen et al. (2021) points out that there is clear need of information about how the streamlines and water pressure distribution inside the fracture alters the flow velocities throughout the aperture and the contact spots and what is the effect to the flow characteristics, especially under varying stress levels.

Numerical methods are effective and flexible tools when simulating complicated geometries and fluid flow conditions in fractured rock mass. Several different approaches have been used to simulate flow through rock fractures. The commonly used approaches are based either on 2D or 3D -fracture dimensions, hypothetical or real fracture types or the fluid flow models such as Reynolds equations, Cubic law etc. Previously mentioned approaches can provide conceptual understanding about the fracture surface behaviour under fluid flow, but they lack several features, such as the absence of the changes in geometry caused by mechanical, geochemical and thermal processes, that cannot be fully incorporated which ultimately can lead to incorrect interpretation of the flow characteristics inside a rock fracture (Chen et al. 2021). Studies by Zimmerman et al. (2004), Javadi et al. (2010), Zou et al. (2017), Kong & Chen (2018) and Chen et al. (2021) combined the effects of the fracture geometries and inertial terms and adopted the full Navier-Stokes equation in flow simulations in the 3D fractures. The importance and the influence of roughness, fracture geometries and inertial effects on fluid flow behaviour in 3D rock fractures was demonstrated by those studies.

This Master's thesis is part of an ongoing research project about fluid flow modelling in fractured rock mass (RAKKA). The project aims to understand the fluid flow behaviour in fractured rocks under different circumstances and the factors affecting it. The goal of the RAKKA project is to define the flow properties of rock fractures with hydromechanical experimental tests. RAKKA project is a continuation for the KARMO project (2014 – 2018) which created a photogrammetric method to measure and record the rock fracture surfaces with high precision.

1.2 Scope of the research

The objective of this thesis is to numerically model fluid flow in artificially induced tensile granite rock fracture at steady state flow conditions. Main research objectives are:

1. To compare the influence of increasing water pressure on fluid flow in rock fracture.
2. Comparization and validation of the results of the numerical flow simulations with the experimental laboratory test results.

3. To create a repeatable workflow for numerical modelling of fluid flow in rock fracture.

Firstly, the motivation for the thesis is to investigate the influence of water pressure on fluid flow in rough rock fracture. Secondly, the aim is to compare the results of the numerical flow model to the experimental laboratory test results and thus, validate the numerical analysis method. Thirdly, this thesis aims to create repeatable and pragmatic workflow for numerical modelling of fluid flow in rough rock fractures. Also, the thesis aims to create knowledge about the phenomena in bedrock since the stability of the bedrock as well as the flow properties of the bedrock are important aspects when judging the safety of the bedrock. This knowledge then can be used in evaluating different methods and implementation of underground rock engineering applications.

This thesis comprises of a literature review and empirical study. Theoretical framework of the topic is provided in the literature review, with short introduction to the physical background of the subject. Flow regime of steady-state flow is presented with the relevant governing equations. The two-part empirical part of this thesis comprises firstly of the presentation of the experimental fluid flow test methodology and secondly of the numerical analysis, including the introduction to the workflow of the numerical analysis. In the last part of the thesis, the results of the numerical analysis are presented and discussed with short conclusions.

Finnish Kuru grey granite is used as a research material for this thesis. 250 mm × 250 mm × 100 mm slab pair sample with a tensile crack in the middle was extracted from the mechanically splitted rock block. A photogrammetry-based method was used to reconstruct a 3D model of the fracture geometry and the resulting model was numerically simulated with COMSOL Multiphysics Finite element method (FEM) software, using the Navier-Stokes equation. Results of the fluid flow experiments, that are used to validate the numerical modelling results, were computed with the Forchheimer equation.

2 Physical background

2.1 Laminar and turbulent flow

The flow of solute material through various rock types occurs generally either by laminar flow or by turbulent flow (Singhal & Gupta 2010). The flow type depends on the coefficient of permeability of the flow and the prevailing hydraulic gradient (Singhal & Gupta 2010). Laminar flow is also known as viscous or streamline flow and it is characterized by parallel flow lines whereas high velocities and the formation of vortexes are typical for turbulent flow (Singhal & Gupta 2010). The velocity of flow is proportional of the first power of the hydraulic gradient in laminar flow (Eq. 1).

$$\begin{aligned} V &= -KI \\ I &= \frac{\Delta h}{\Delta l} \end{aligned} \quad (1)$$

where K is the coefficient of permeability, I is the hydraulic gradient, Δh represents the difference of the water head level in a given length Δl . The velocity of flow in turbulent flow is expressed as

$$V = -KI^\alpha \quad (2)$$

where α ($0,5 \leq \alpha \leq 1$) is the degree of nonlinearity of the flow.

Large pores, solution cavities and wide fractures may cause turbulent flow which in case indicates relatively high hydraulic gradient (Singhal & Gupta 2010). Singhal & Gupta (2010) present that the inertial forces are much smaller in laminar flow than viscous forces. The transition from laminar to turbulent flow depends on the Reynold's number (R_e). When assessing the flow characteristics of a rock fracture, the Reynolds number, which is defined as the ratio of inertial forces to viscous forces, is typically used to quantify the onset of nonlinear flow, where ρ is the fluid density, μ is the viscosity of water and w is the fracture width (Schlichting, 1968):

$$R_e = \frac{\rho Q}{\mu w} \quad (3)$$

The diameter of the pipe can be replaced by the hydraulic diameter in fractured rocks, which then can be expresses by

$$D_h = 4A / \rho \quad (4)$$

where A is the cross-sectional area of the fracture through which the flow takes place and ρ is the outside perimeter of the cross-section area of the flow (de Marsily 1986). According to de Marsily (1986), hydraulic diameter is equal to twice its aperture for very long fractures. Reynold's number for non- circular conduit such as fracture is given as

$$R_e = \frac{\rho V(4R_h)}{\mu} \quad (5)$$

where $R_h=A/P$ is the hydraulic radius which is the ratio of the cross-sectional area A to the wetted perimeter P. $D=4R_h$ for a circular cross-section. According to Singhal & Gupta 2010) natural fracture walls have varying roughness which might cause drop in pressure,

influencing the flow conditions. Fracture wall roughness is denoted by dimensionless number, R_r which is defined by

$$R_r = R_f / D_h \quad (6)$$

where R_f is the mean height of the asperities in the fracture. Determination of Reynold's number in fractured rocks might be difficult since depending on a flow type, it can vary greatly along the same fracture (Singhal & Gupta 2010). Usually, the flow regime is regarded as laminar for $Re < 2000$ and turbulent for $Re > 2000$ (de Marsily 1986). According to experimental data by Van Golf-Racht (1982), transition from laminar flow to turbulent flow in fractures start to take place already at very low values of Reynold's number of 600. It should also be noted that the transition from laminar flow ($\alpha=1$) to entirely turbulent flow ($\alpha=0,5$) is reasonably progressive with the exponent slowly changing from 1 to 0,5 while the Reynold's number changes for instance from 100 to 2300 (Louis 1974).

2.2 Governing equations

The Forchheimer equation (Qian et al. 2019) was adopted to characterize the fluid flow through a rough fracture (Eq. 7 to 9).

$$-\nabla P = aQ + bQ^2 \quad (7)$$

$$a = \frac{12\mu}{we_h^3} \quad (8)$$

$$b = \frac{\beta\rho}{w^2e_h^2} \quad (9)$$

where ∇P is the hydraulic gradient (Pa/m), a ($\text{kg/m}^2\text{s}$) and b (kg/m^8) denote viscous and inertial effects, respectively, Q is flowrate (m^3/s), w indicates the width of the fracture (m), e_h signifies the hydraulic fracture (m), μ is the dynamic viscosity of water ($\text{Pa}\cdot\text{s}$), L represents the length of the fracture (m) and β characterizes nonlinear coefficient, and ρ represents the fluid density (kg/m^3).

The numerical modelling was solved by the Navier-Stokes equations for water as incompressible and single Newtonian fluid flow in the COMSOL software (Eq. 10 to 11). Equations of mass and momentum conservation govern the Navier-Stokes equations, and for stable, incompressible and isothermal single Newtonian fluid flow, such as water fluid flow, the equations are written as (Bear 1972, Zimmermann & Bodvarsson 1996):

$$\rho(u \cdot \nabla)u + \nabla P = \mu \nabla^2 u \quad (10)$$

$$\nabla \cdot u = 0 \quad (11)$$

where u represent the flow velocity vector, P represent the fluid pressure, ρ represent the fluid density and μ represent the dynamic viscosity. In Eq. (27), the term $\mu \nabla^2 u$ represents the viscous force, and the convective acceleration terms $(u \cdot \nabla)u$, representing the inertial forces acting on the fluid, giving rise to the nonlinearity of the equation and increase the computational cost.

3 Theoretical framework of fractured rocks

3.1 Definitions

Rock fractures or rock joints can be regarded as any separation in geological formation. According to Singhal & Gupta (2010), rock fractures are planar surfaces where the loss of cohesion in the rock has taken place due to stress and they represent planes in the rock body. The scale of fractures varies from microscopical to fracture zones extending to several kilometers. The main cause for fracturing is stress which may have diverse origin, such as tectonic stress related to the deformation of rocks, residual stress due to the events prior to the fracturing, contraction due to shrinkage from magma cooling or desiccation of sediments, surface movements such as landslides or movement of glaciers, erosional unloading or weathering (Singhal & Gupta 2010). Fractures can be classified in many ways. Broadly, fractures can be categorized as systematic and non-systematic fractures with systematic fractures being planar and more regularly distributed and non-systematic being irregular and curved (Figure 2). Other ways to categorize fractures, are for instance geometric classification, classification in accordance with the extent of development or genetic classification (Singhal & Gupta 2010).

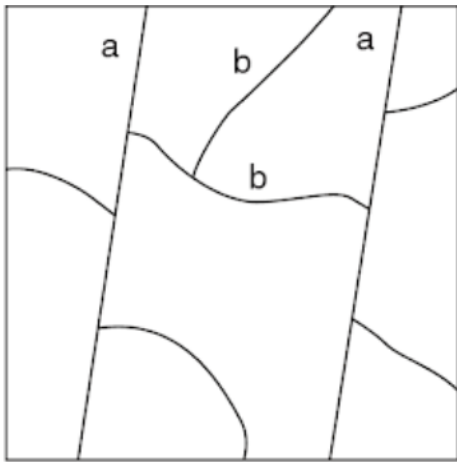


Figure 2. Systematic (a) and non-systematic (b) fracture types (Singhal & Gupta 2010).

According to Singhal & Gupta (2010), fractured rock mass comprises of three components which are the fracture network, matrix block and possible fracture infillings and single fracture in the fracture network is characterized by several parameters. Parameters characterizing single fracture are number of fracture sets present in the fracture network, orientation of the fracture, spacing between adjacent fractures in the fracture network, length of the fracture, linear, areal and volumetric density, area of fractured surface and its shape, number of fractures per cubic meter of rock volume, block size and shape resulting from the fracture network, connectivity of fractures in the fracture network, aperture of the fracture in the fracture network, asperity of the fracture in the fracture network and wall coatings and infillings of the fracture in the fracture network (Singhal & Gupta 2010).

Aperture is the perpendicular distance between the adjacent rock walls of an open fracture in which the open space is filled with fluid or air (Singhal & Gupta 2010). Aperture may vary from very tight to wide as presented in Table 1, and usually subsurface rock masses have relatively small apertures (Barton 1973, Singhal & Gupta 2010). Tensile stress commonly leads to larger apertures and shear fractures have usually much smaller apertures

than tensile fractures (Singhal & Gupta 2010). Dissolution and erosion may increase the aperture whereas the aperture may decrease with depth due to the lithostatic pressure, which means that fracture wall compression is an important parameter governing aperture, since lithostatic pressure has tendency to close the fracture opening (Singhal & Gupta 2010).

Table 1. Aperture classification by size (Singhal & Gupta 2010 after Barton 1973).

Aperture (mm)	Definition
< 0,1	Very tight
0,1 - 0,25	Tight
0,25 - 0,50	Partly open
0,50 - 2,50	Open
2,50 - 10,0	Moderately wide
> 10,0	Wide

Irregularities in the fracture walls are called asperities (Figure 3). Asperity reduces fluid flow in the fracture and leads to a local channeling effect of preferential flow which reduces the effective porosity and makes the flow turbulent (Singhal & Gupta 2010).

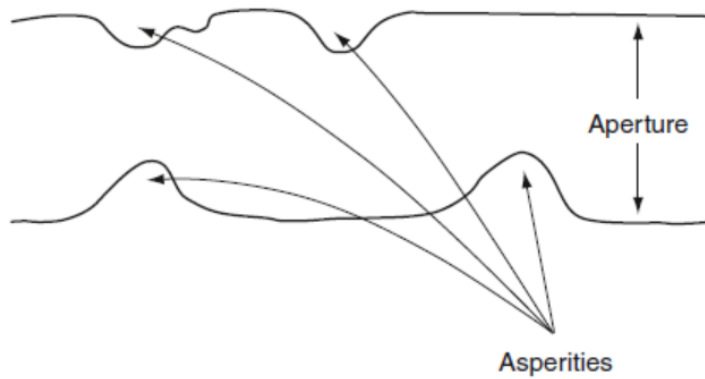


Figure 3. Asperities in the fracture walls (Singhal & Gupta 2010).

3.2 Different types of fracture aperture

Hakami (1995) and Hakami & Larsson (1996) point out that before going deeper into fracture networks and their properties, geometrical definition of single aperture should be made. Aperture can be defined by fracture surfaces, void space and a reference plane (Hakami & Larsson 1996). Concepts of hydraulic aperture and mechanical apertures have been extensively used to describe the deviations between the theoretically defined permeability and experimentally detected permeability (Barton et al. 1985, Tsang 1992, Esaki et al. 1998). Mechanical or physical aperture can be regarded as the degree of openness between the fracture walls. In other words, mechanical fracture represents the width of the fracture. According to Baghbanan & Jing (2007), hydraulic aperture represents the transmissivity of the fracture. Hydraulic aperture is the capability of fluid to flow through a rock fracture (Baghbanan & Jing 2007). Hydraulic aperture is generally smaller than mechanical aperture.

One of the simplest ways to describe water flow through fractures is assume laminar flow between parallel plates (Boussinesq 1868, Snow 1965). The parallel-plate model as a solution to Navier-Stokes equations leads to the widely used Cubic law (Snow 1965, Krantz et al. 1979, Tsang & Witherspoon 1981). The cubic law precisely describes the flow between

two plates that have smooth walls which creates a problem since natural fractures are most probably rough walled with asperities lowering the total flow (e.g. Brown 1987). It can be said that the corresponding aperture through which the fluid flows, called hydraulic aperture, is smaller than the actual opening displacement of the fracture which can also be called mechanical aperture (Schultz et al. 2010).

3.3 Variations in fracture aperture

Several different phenomena can have an impact on the fracture aperture. According to Singhal & Gupta (2010), these phenomena can be intrinsic such as fracture surface conditions and surface roughness or external such as environmental phenomena. Contact area of fracture surfaces and the distribution of the contact areas affect fluid flow types and fluid flow regime inside the fracture and that can be regarded as intrinsic also (Singhal & Gupta 2010). Especially selected fluid flow model is affected by the flow type and pressure with laminar or turbulent regimes. Scale effects can also have an impact on calculated or measured fracture aperture. Asperities usually affect the aperture size and render its measurement difficult in field conditions (Singhal & Gupta 2010). According to Singhal & Gupta (2010), apertures are defined in terms of flow properties when considering fluid flow since volumetric flow rate is governed by the cube of aperture. Aperture can be integrated with fracture density to give an integrated function representative of hydraulic conductivity (Singhal & Gupta 2010).

3.4 Calculating and measuring the fracture aperture

Measuring, calculation and characterization of the fractures and fracture apertures can be done mainly by two ways, either with direct or indirect methods or by combining these two. Direct techniques for detecting and imaging fractures in the field are for instance video imaging or geophysical methods such as seismic reflection studies, electric conductivity studies and ground penetrating radar (Keller 1998). Direct methods include for instance defining the fracture aperture in the laboratory by scanning the two surfaces of the fracture creating a map of the surface roughness or by injecting solidifying liquid to the fracture such as resin (Keller 1998). Keller (1998) states that the problem with these methods is that they might render the fracture useless for flow experiments. Computerized axial tomography X-ray scanning is a good method to study fluid flow in fractured rock and with CAT-scanning the resolution of the image is about 38 μm (Keller 1998). According to Keller (1998), CAT-scanning method is a good tool in studying the flow through fractured rock.

Indirect methods for defining fracture aperture comprise of using back calculation from hydraulic test in laboratory or numerical modelling. The accuracy of indirect methods varies and mainly they are used in detecting large rock features and can be used in the field or at the laboratory scale for higher resolution, but it should bear in mind that with higher resolution, the understanding of the controlling mechanisms and parameters for flow in fractured rock increases. Indirect techniques for defining fracture aperture can be for instance pumping and tracer injection tests where arithmetic mean, geometric mean and standard deviation of the fractures can be calculated using Boussinesq or cubic law (Keller 1998). Permeability and dispersivity of a fracture can be calculated from the statistics of the aperture distribution with the addition of calculating the streamlines for the fracture plane and predicting channelling and breakthrough, still it should be noted that the fracture aperture distribution can be very heterogeneous even for simple fractures (Keller 1998, Mohanty & Hsiung 2011).

Indraratna & Rajnith (2001) present several methods for measuring the fracture aperture which include feeler gauge, fluorescent dyes, impression packer, tracer test and hydraulic test. Vernier caliper or gauge can be used to measure the aperture in surface exposures and the measured opening is termed as the mechanical aperture (Singhal & Gupta 2010). In the laboratory, fracture aperture can be estimated by impregnating rock samples with dyes or resin and by studying the thin sections under the microscope (Singhal & Gupta 2010). In-situ spatial variation of fracture aperture can be estimated by two field techniques which are according to Steele & Lerner (2001) the conventional slug hydraulic testing using packers or the technique where NAPL (sunflower oil) is injected into isolated fractures in a borehole.

4 Hydromechanical coupling in fractured rocks

4.1 Hydromechanical coupling

Fractured rock masses comprise of intact rock blocks and fractures, which work as main pathways for fluid flow (Min et al. 2004). Fracture aperture can vary either due to closures induced by normal stress or openings or due to shear stress induced dilations (Min et al. 2004). Because of the previous notions, permeability of fractured rocks can be defined as stress dependent. According to Rutqvist & Stephansson (2003), hydromechanical coupling can be either indirect, where the applied stresses produce changes in the hydraulic properties of the rock or direct, where the applied stresses produce changes in fluid pressure (Figure 4).

Indirect hydromechanical coupling can be seen as particularly important in fractured rock masses because stress induced alterations in permeability can be up to several orders of magnitude and irretrievable (Min et al. 2004).

It is common conception that horizontal stress is the maximum principal stress at least in shallow bedrock (Şen & Sadagah 2002). Additionally, according to Şen & Sadagah (2002), the ratio of maximum to minimum principal stress value has notable influence on underground engineering designs.

Hydraulic properties fluctuate easily depending on the mechanical loading conditions on the rock which means that the hydraulic characteristics are almost completely coupled to the mechanical behaviour of rock fractures (Noorishad & Tsang 1996, Lee & Cho 2002).

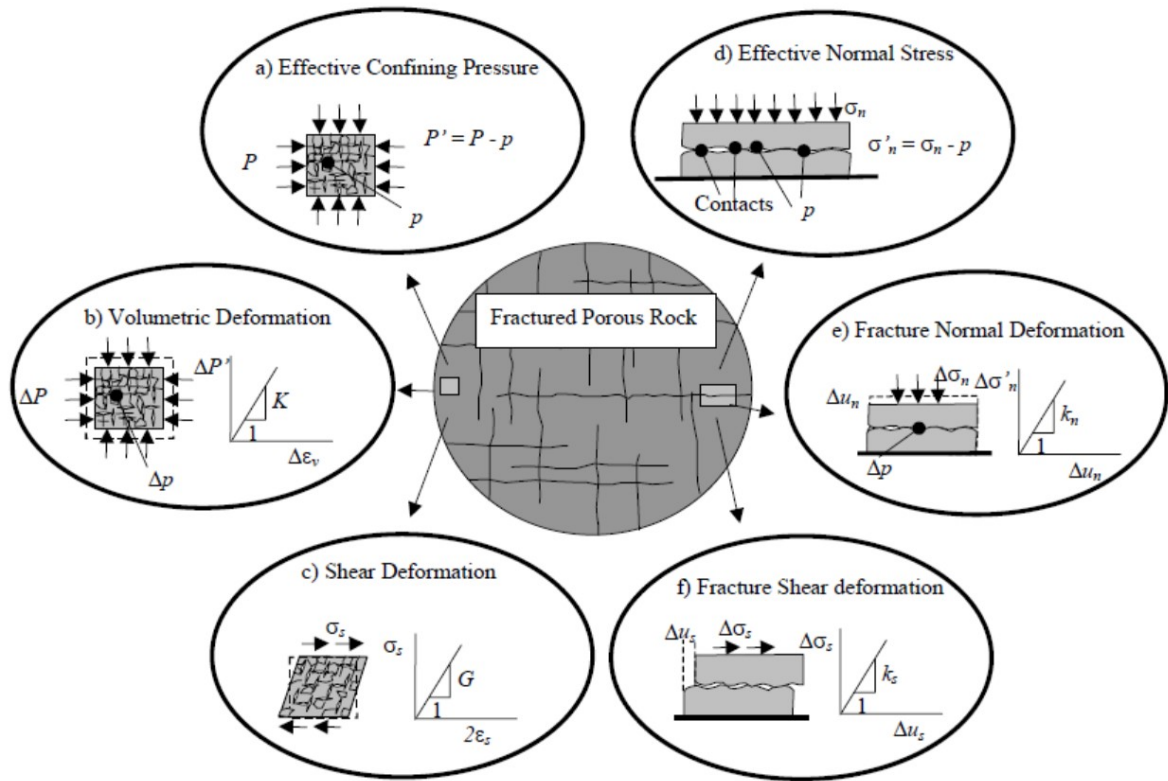


Figure 4. Schematic overview of a fractured rock mass comprising of porous matrix and macrofractures (Rutqvist & Stephansson 2003).

According to Lee & Cho (2002), the relation between mechanical aperture and hydraulic aperture is fairly linear under normal loading but as the normal stress increases and the mechanical aperture grows smaller, the corresponding hydraulic aperture diverges from the linear development which is concluded to be caused by more tortuous flow paths at high stress levels.

Dilation and gouge production from asperity degradation are two factors that influence the hydraulic behaviour of fractures under shear deformation (Lee & Cho 2002). Displacements caused by shearing and following dilation may increase the permeability by two orders of magnitude according to Lee & Cho (2002).

4.2 Hydromechanical behaviour of rock fractures

The geometry of the fracture system and the magnitude and orientation of in situ stress are the main factors controlling the ability of a fractured rock to transport fluid and since the existing stress field can vary due to underground activities or natural geological processes, it is important to understand how fracture permeability varies as a function of normal or shear stress (Raven & Gale 1985). Raven & Gale (1985) states that existing data suggests that increased fracture hydraulic conductivity at maximum normal stress increases with cross-sectional fracture area. To properly model the function of fracture networks, transport properties and structure of single fracture must be fully understood. According to Plouraboué et al. (1995), fracture aperture and roughness of the fracture walls are the key parameters affecting the fracture permeability and the structure of the flow field inside the fracture. Friction, wear and gouge formation are important factors related to accurate description of the fracture surfaces and thus the flow inside the fracture (Plouraboué et al. 1995).

Raven & Gale (1985) concludes that the roughness of the fracture surfaces is a major factor that determines the variations in fracture-flow-rate relations and especially this in mind, more work is needed on measurement of fracture roughness and coupling that data with load-deformation and stress-permeability tests. Comparison between measured values and predicted data sets by Zimmermann & Bodvarsson (1996) suggest that accurate predictions of fluid conductivity through rock fractures can be made by combining the results from the perturbation data with the tortuosity data.

Fractures are encountered in all rock terrains and the geometry of fractures varies and changes constantly due to the deformation which can cause the fracture to dilate, close or shear. Mohanty & Hsiung (2011) state that since the hydrological properties change due to the deformation, there is mechanical-hydrological coupling between the rock stress and hydrological properties of fracture. Mechanical-hydrological process means that the mechanical stress affects fluid flow in the fracture and the fluid pressure affects the mechanical condition meaning for instance the effect of fluid pressure build up on rock deformation (Mohanty & Hsiung 2011). There are several models for studying the behaviour of fracture networks but since the flow characteristics of fracture network is governed by single fractures, more work is needed to understand the behaviour of a single fracture and fracture permeability can be regarded as the most important parameter in that field according to Mohanty & Hsiung (2011) with fracture permeability being mostly studied as a function of normal stress with few studies concentrating on shear stress. Mohanty & Hsiung (2011) concluded that fracture permeability decreases with increasing normal stress whereas with shear stress the results are more complex. Shearing results in gouge formation and fracture dilation which are competing effects so the fracture permeability might not change too much.

5 Research material and methods

5.1 Methodology

In order to investigate the hydraulic properties of rock joints, real situations existing in the field, such as different rock joint roughness, non-identical stress conditions, a wide variety of water pressures and flow directions should be considered. Uotinen et al. (2020) and Torkan et al. (2021) created an experimental laboratory test set up for investigating the water flow inside a rock fracture with simulated real-life conditions. The experimental workflow is as follows: investigating fracture morphology using a profilometer measurements with photogrammetry and water flow tests. The calculations were verified by comparing the predictions based on roughness and the measurements from the water flow tests (Uotinen et al. 2020). The experimental tests were conducted in the civil engineering laboratory at Aalto University during 2020 and 2021 at a temperature of approximately 25° C, and the density and dynamic viscosity of water, $\rho = 0.997 \times 10^3 \text{ kg/m}^3$ and $\mu = 0.89 \times 10^{-3} \text{ Pa} \cdot \text{s}$, respectively. Last phase of the experimental workflow for investigating the hydraulic properties of rock joints is the numerical simulation which is presented in Chapter 6.

5.2 Research material and sample preparation

The research material used in the flow tests is Finnish Kuru grey granite with the average density of $2\,670 \text{ kg/m}^3$. The sample material is fairly homogeneous and isotropic. The blocks are separated to two rock slabs with horizontal fracture. Altogether 12 rock blocks with the size of $250 \times 250 \times 110 \text{ mm}$ including the fracture were manufactured for the RAKKA project. Sample number 05 was used for this thesis. Table 2 presents the data sheet for the rock sample with sample ID and sample information.

Table 2. Data sheet of the rock sample used for steady state flow tests and numerical modelling.

Sample	Size (mm)	Mass (kg)
05	$250 \times 250 \times 110$	16,5

The rock block has a horizontal mechanically induced tensile fracture. The sample production is described according to Dzugala (2016). The manufacturing of the rock block is made in 5 steps. The fracturing is made by wedging and the first step is to drill a line of holes for the wedges in the line where the projected fracture should be. The drilling is made with handheld drill bit with the distance between the holes being approximately 15 cm (Dzugala 2016). Second step is to position 10 cm wedges to the holes and hammer them in. Wedges are hammered to the holes with rubber hammer creating the initial crack. According to Dzugala (2016), the direction of the propagation of the initial crack gives indication of which wedges should be hammered in deeper. In step 3 and 4, after the initial crack is propagated through the rock block, wedges are removed, and the block is cracked manually in two parts. The last step is to saw the rock block to desired dimensions. The parts affected by drilling and wedging are cut off at this stage.

The manufacturing process of the rock samples creates very fine rock dust and when it mixes with water used in drilling and sawing, it accumulates in the crevasses and cracks of the fracture surfaces. Rock dust, dirt and loose rock fragments can hamper the 3D photogrammetry process as well as the precise measuring of the JRC values. To prevent that, after the rock slab is separated for photographing and JRC measurements, the fracture

surfaces should be cleaned thoroughly by using strong brush and compressed air. Example of grey Kuru granite rock block is presented in Figure 5.



Figure 5. Kuru grey granite rock block 250 mm × 250 mm × 110 mm. Markings on the rock block are for photogrammetry purposes.

5.3 Photogrammetry

JRC (joint roughness coefficient) plays an important role when assessing the roughness of joints (Barton and Choubey 1977). Joint surface roughness can be defined for example according to undulation and irregularities of joint surface (ISRM 1978).

The procedure for investigating the fracture morphology using photogrammetry is a three-phase method based on the methodology created in KARMO II project to create a photogrammetric prediction of the joint roughness according to 3D model of the joint surface (Dzugala 2016, Kallio 2015, Sirkiä 2015). According to Uotinen et al (2020) and Torkan et al. (2021), the idea is to capture the whole fracture surface of the sample from every side with two dip angles of 30° and 60° and to reconstruct the fracture surface using the Structure-from-Motion photogrammetric method.

In the first phase, both slabs are in tight contact, and each sample is fitted with circular targets for photogrammetry (Figure 6a). Target-to-target distances are manually measured with a digital caliper with the resolution of 0.1 mm, resulting in an accuracy of +/- 0.2 mm. The camera should be positioned on a tripod in a fixed position and each sample half is photographed using a revolving table by taking 40 photographs per revolution (Figure 6b and c). This process should be conducted for two dip angles of the camera (30° and 60°). According to Torkan et al. (2021), the photographs for this study were taken using Canon 5DS R DSLR camera and Canon 35 mm f/1.4L II USM objective.

Then, the sample half is flipped upside down, and the process is repeated. To improve the accuracy of the method, a 4×4 grid consisting of square cells each with 5 cm side length,

should be used. At each grid node a photo is taken, 25 images for each surface. This results in a full exterior 3D reconstruction of the sample pair. The model is oriented and scaled using the measured distances between the circular targets. Each set of photographs is processed into a 3D model using the Reality Capture software (Figure 6d). The images should be aligned using the default settings and the dense 3D point cloud of the sample should be reconstructed using the Normal detail mode. The result of processing the images is three 3D models, one for the bottom, one for the top and one for the pair.

After this stage, the data of both halves will be placed in the same coordinate system according to the circular targets. Finally, the physical aperture distribution is calculated with the coordinated data of the top and bottom halves with CloudCompare software (Figure 6e and f). The point cloud should be saved as a .xyz file and import into CloudCompare v2.10.1 software. The physical aperture distribution is calculated to extract the roughness profiles. For this purpose, the Extract sections -function is useful and it enables to extract cloud sections along polylines. Uotinen et al. (2020) extracted three parallel profile pairs in both X and Y directions from 3D point clouds of the bottom and the top fracture surfaces.

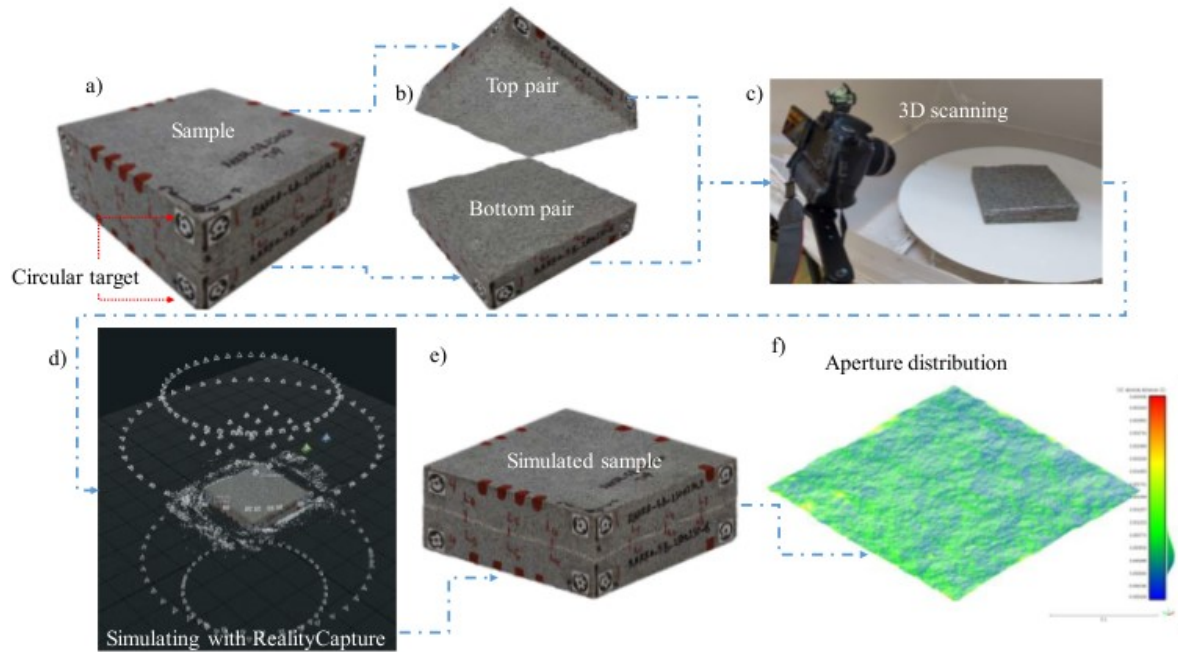


Figure 6. Photogrammetry and measurement procedures of fracture morphologies (Torkan et al. 2021).

5.4 Water flow tests

To be able to study the hydraulic properties of rock fractures and to validate the results of numerical analysis, a pilot test set up for flow-stress test was constructed. First prototype of the experimental laboratory set up was created by the author in the summer of 2019. The idea was to measure the flow in controlled environment through rock blocks of varying size from 25×25 cm ($0,00625 \text{ m}^3$) up to 1×1 m ($0,5 \text{ m}^3$) with varying water pressures and with possibility to include stress factor. Initially, the idea was to create the prototype test set up for the small rock block and then scale the set-up size for the bigger rock blocks.

The aim was to seal the fracture and conduct water through it in a controlled manner. The most important consideration for the flow-stress test was the sealing against water leakage

during the test, also allowing dilation to some extent when increasing the water pressure. In order to fulfil these experimental requirements, elastic tape with elastic glue was used to seal the sides of the rock block and elastic rubber to seal the outlet and inlet sides. Aluminium blocks were crafted to inlet and outlet -sides of the rock block and they were tightened against the rock with screws and bolts. Air release valve was installed to the aluminium block in the inlet side so the release of excess air in the tubes was possible. A digital balance with a precision of 0.01 g was installed to outlet side to measure the amount of water flowing through the fracture. Principle of the first prototype test is shown in Figure 7.

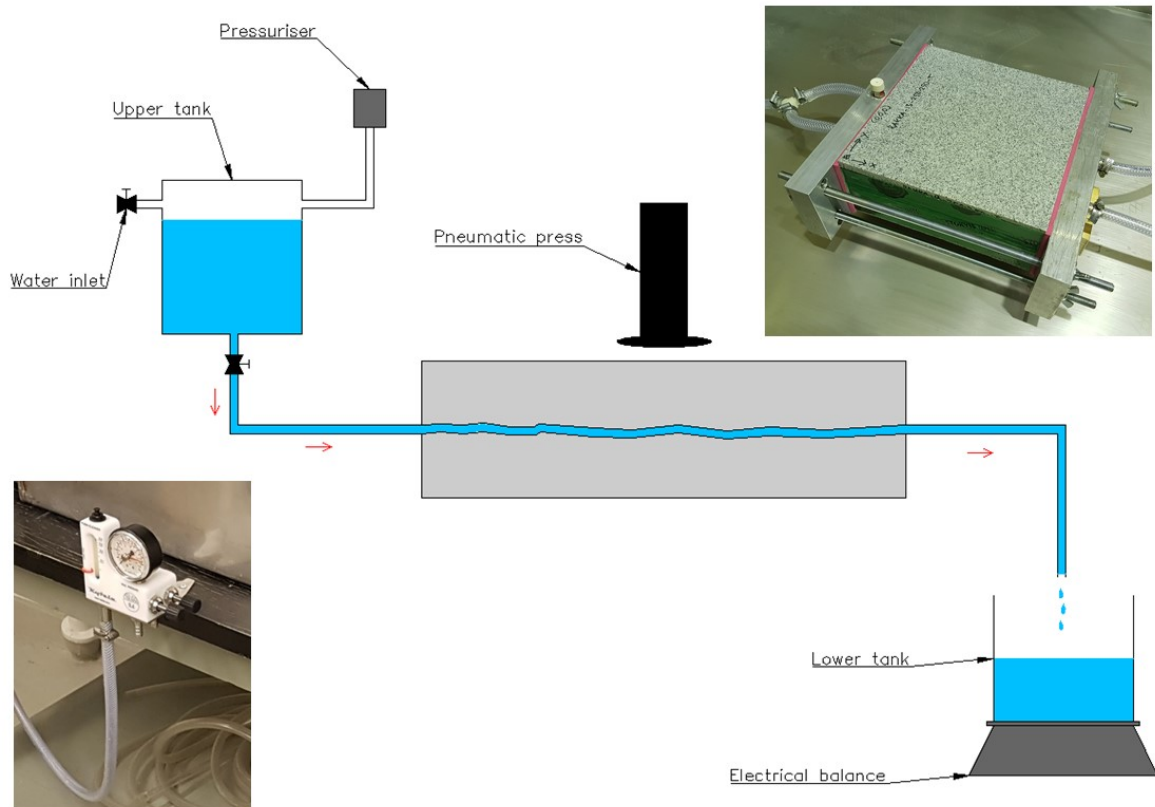


Figure 7. First prototype of the experimental laboratory set up on the right side and detail of the Kytölä pressure meter on the left with a sketch illustrating the principle of the experimental test.

First experimental laboratory set up was unsuccessful and the execution of the flow-stress test failed. The sealants leaked and the tightened aluminum blocks did not allow any movement. The lessons from the failed first prototype were utilized in creating the second prototype of the laboratory test set up.

The methodology regarding the second prototype and the steady state flow test is described according to Uotinen et al. (2020) and Torkan et al. (2021). To set up the steady state flow test, a laboratory test shown in Figure 8 was manufactured by Uotinen et al. (2020) and Torkan et al. (2021). The laboratory test set up was designed to investigate flow paths to multiple directions as in the actual conditions. The flow test set up comprise of a hydraulic jack unit, a data logger, a water tank, air compressor, adjustable air regulator, a pressure transducer, a steel plate, self-designed frame, water collector and a digital balance.

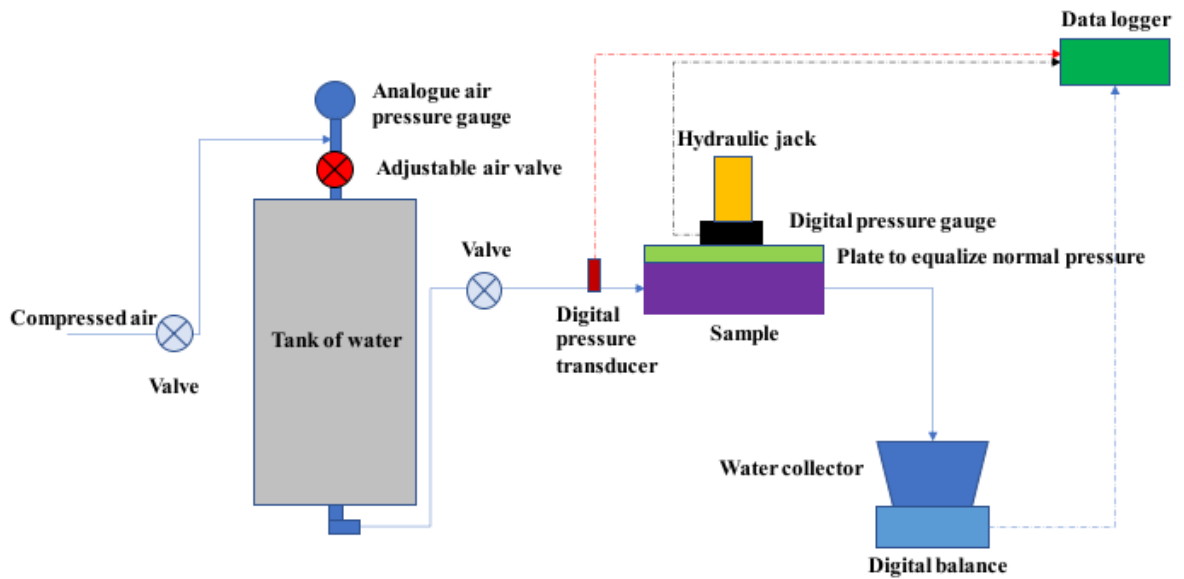


Figure 8. Schematic illustration of the hydraulic test circuit (Torkan et al. 2021).

Hydraulic jack unit is used to apply normal pressures on test sample and a data logger to record the data acquired. A steel plate was used to equalize normal pressures on the top surface. Air compressor and an adjustable air regulator apply constant water pressures to one side of the fracture from the water tank. A pressure transducer was attached to the water inlet to measure the inlet water pressure. The discharge water was collected to water collector and measured by a digital balance with a precision of 0.01 g. Ten water pressures were chosen to conduct these tests, ranging from 5 kPa to 50 kPa with 5 kPa intervals.

Figure 9 presents a diagram of a self-designed frame that was designed to seal the lateral sides of the sample. This frame can control pathways of inlets and outlets in preferred directions. The internal faces of the frame were covered by the rubber to avoid leakage of the sample but also to provide freedom of movement. The inlets and outlets were controlled by valves to be selected water flow directions. Silicon glue and tape were used to seal the corner of the sample to prevent the connection between sides. To detect amounts of vertical movements of the fracture after applying normal stress, four LVDTs (linear variable displacement transformer) were installed around the sample as shown in Figure 10.

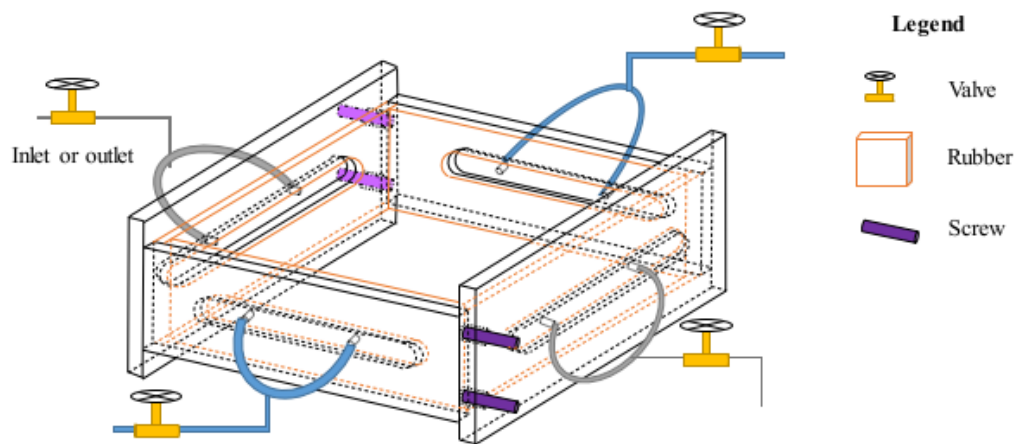


Figure 9. Diagram of the self-designed frame to test the water flow (Torkan et al. 2021).

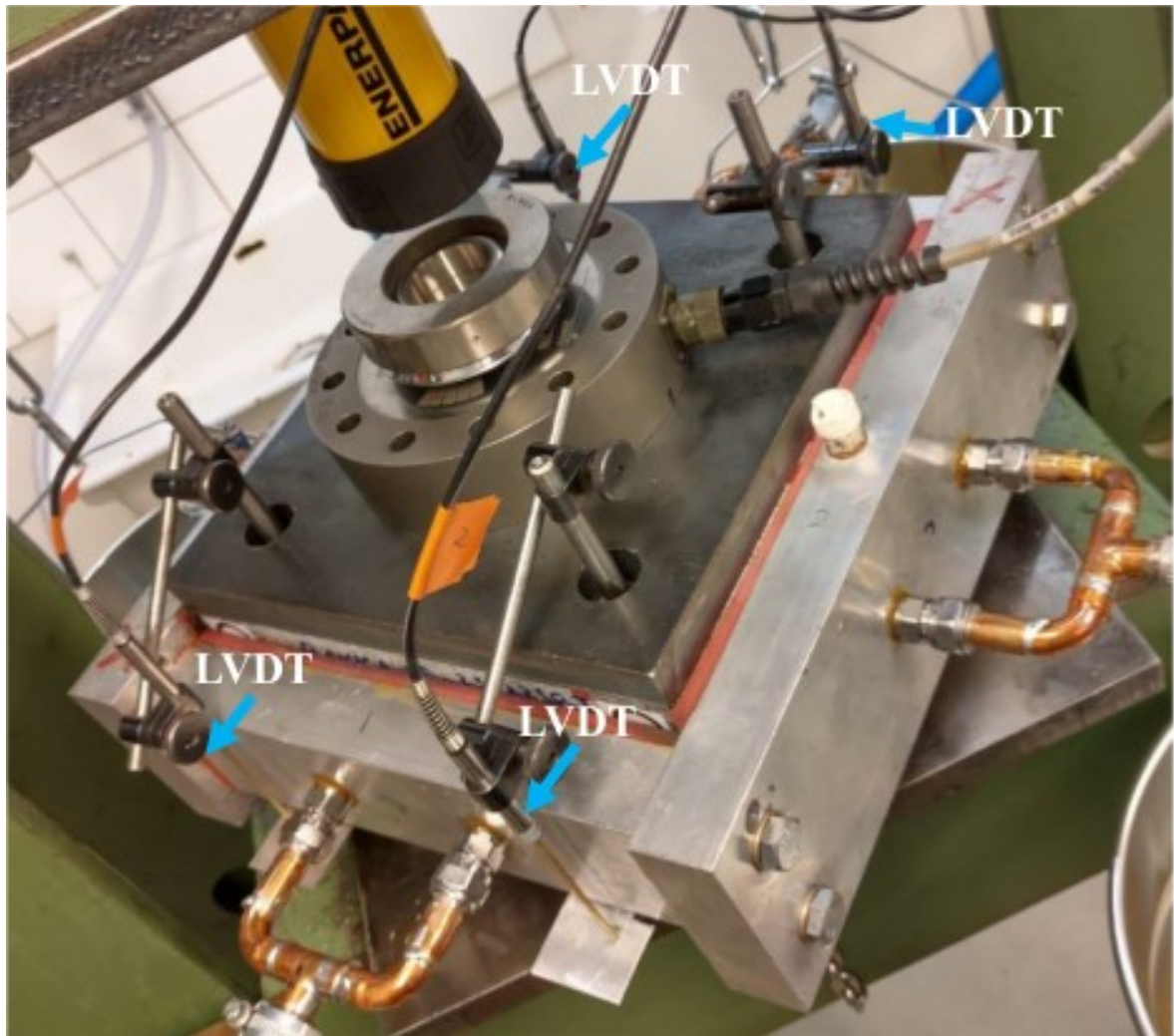


Figure 10. Self-designed water flow test frame and the locations of LVDTs (Torkan et al. 2021).

6 COMSOL Multiphysics simulation model

A numerical model was developed for the rock sample using the COMSOL Multiphysics software version 6.0[®] (COMSOL 2021) to perform the fluid flow analysis. COMSOL Multiphysics is a simulation software especially suited for simulating and analyzing complex problems in physics and engineering. COMSOL uses a Finite Element Method (FEM) to evaluate models providing a useful tool in exploring the fluid flow in rock fracture.

COMSOL is a modular programming platform and the necessary interlinked equations describing the physical problem can be formulated by ‘writing’ the equations and linking necessary solver modules. In the next chapters, the COMSOL model used in this work, the modelling parameters and modules used are described. The basic model used in the thesis is a solid model that represents the fluid-filled rock fracture for which the fluid flow is modelled. The modelling modules in COMSOL are called physics interfaces. In this case, the fracture has own parameters and physics. The features relevant to the present work are included here and a more complete description of COMSOL and the modules used are found in the COMSOL Reference Manual.

6.1 Model tree and definitions

The building of the COMSOL model begins with defining the geometry of the problem object that is going to be solved. The geometry can be for instance 2D, 3D, cone or block. The analysis type which can be time-dependent, stationary etc. is also defined. After defining the geometry and the analysis type, all physics and parameters required for actual modelling can be defined using a so-called model tree. An illustration of the model tree for the fluid flow problem in this work is shown in Figure 11.

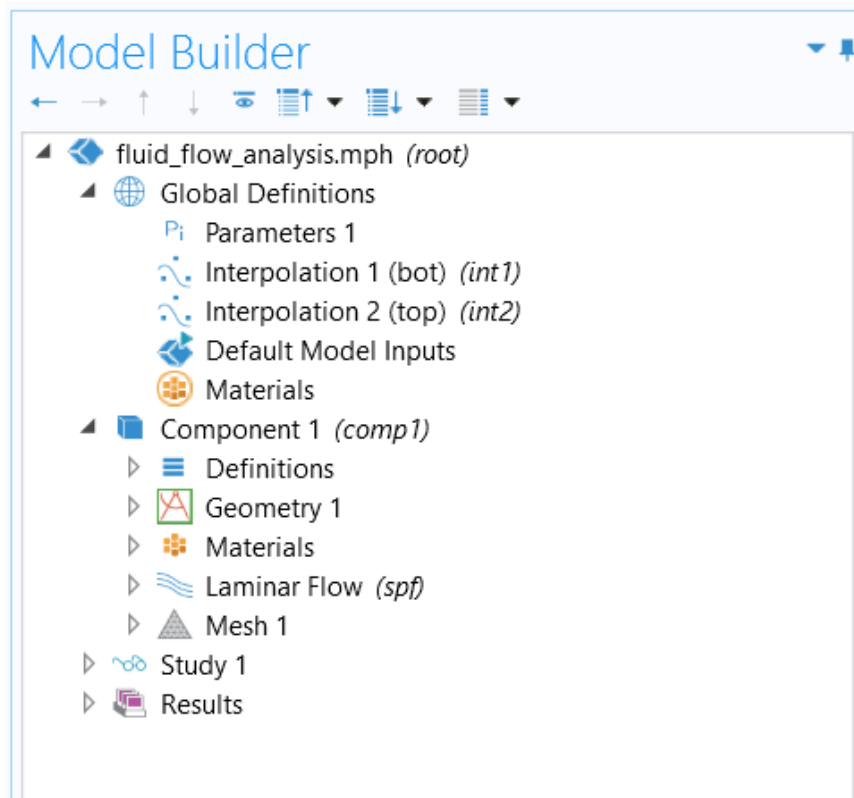


Figure 11. COMSOL Model tree (Model Builder) for this thesis fluid flow analysis.

The whole modelling process is controlled through the Model Builder window. The Model Builder window defines the model tree, and the model tree includes the necessary functions and operators to create and solve the models and present the results. According to COMSOL (2021), the model tree helps to define the data structure for the model object, which stores the state of the model including settings for geometries, numerical mesh, physics models, boundary conditions, studies, solvers, post-processing and visualizations.

The Global Definitions node and the Results node are the two default nodes in the model tree in COMSOL. The Global Definitions node includes a Materials sub-node. In the Global Definitions node, all common parameters, variables, functions and couplings, used in the physical models, are defined. In addition, values and functional dependencies of material properties, forces, geometries, and other relevant features, which are used throughout the models, can be defined here. Under the Component node, the specifics of a certain physical component can be defined, and it can also include component material properties. There can be multiple Component nodes in the COMSOL model. The main difference between the Global and the Component node definition is that the Global node applies for the entire model and the Component node for the component in question only. A special feature in COMSOL is a probe function, which enables to provide results during the simulations. The probe can be defined to any (x,y,z)-point in the mode, and it is useful for checking whether the results are sensible or not, enabling to interrupt the calculations, if necessary.

After the simulation is executed, the solution can be accessed through the Results node. The Results node includes needed tools for processing the output data, e.g. graphical presentations. In practical terms, creating the models in COMSOL begins by defining the Global Definitions, and then moving to the Component nodes and finally to the Results node.

6.2 Geometry

First step in building the COMSOL model is defining the model geometry. The model geometry was defined according to the pre-processed point cloud data from the photogrammetry analysis presented in section 5.3. The point density of the point clouds is 1 mm. Building the model geometry starts with creating an interpolation surface by adding an Interpolation function under Global definitions node (Figure 12). The point cloud text files containing the x,y,z-coordinates of the top and bottom surface are imported under the Definition headline. Data source is set to File and the decimal separator is set according to the separator used in the file. Data format is spreadsheet. The Interpolation functionality will automatically guess that the data is on the form $z = f(x, y)$ and that the first two columns in the file represent the x- and y-coordinates, respectively, and that the third column represents the function value, which we will interpret as the z-coordinate of a function surface. Hence, number of arguments is set to 2, corresponding to the x- and y-coordinates, respectively. The Function name is automatically set to int1 and the Position in file setting 1 means that the function value for int1(x,y), representing the z-coordinate, will be given by the first column following the input argument columns. Interpolation function was created for both, top and bottom surface of the fracture.

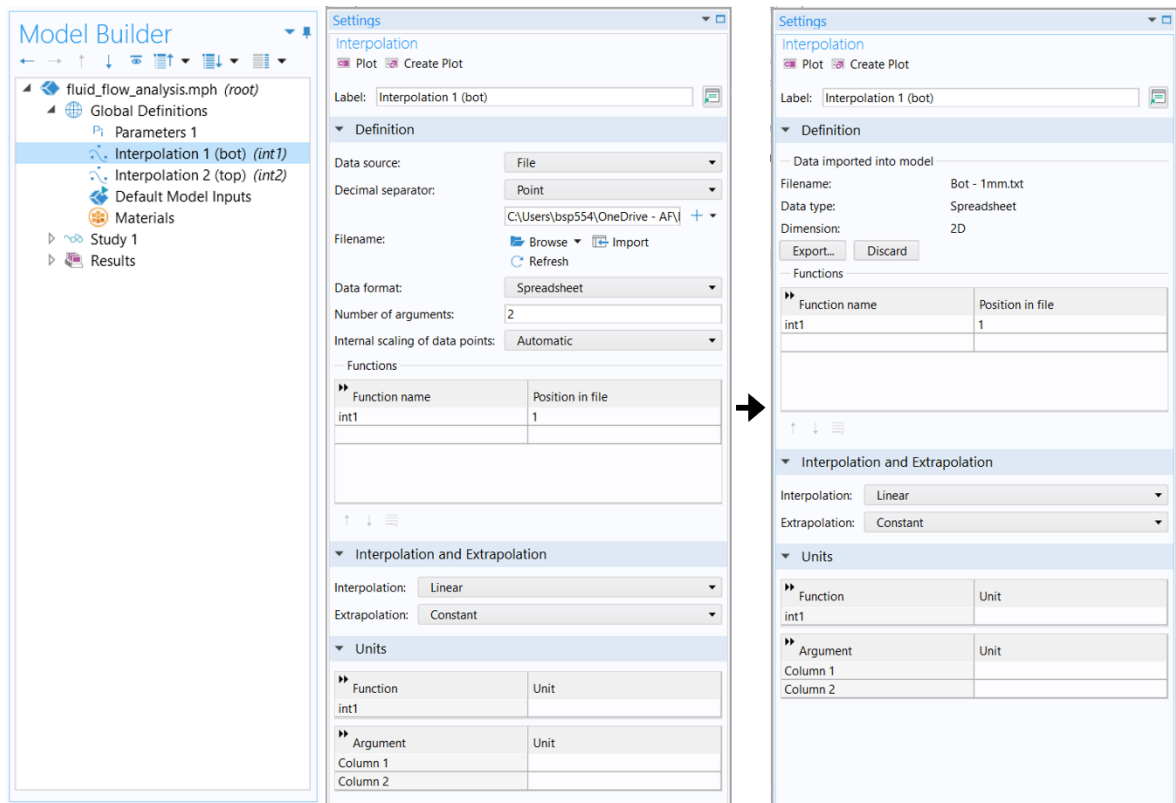


Figure 12. The Interpolation function of the bottom surface of the fracture defined by the point cloud. Right side of the Figure shows the imported point cloud in the Interpolation tab.

After the interpolation functions were defined, the geometric representation for top and bottom surfaces are created by adding Parametric surface under Geometry in Component node (Figure 13). Expressions $s1$ and $s2$ represent the x- and y-coordinates, respectively and $int1(s1,s2)$ represent the z-coordinate. Minimum and maximum values were set to define the extent of the point cloud.

To get a better representation of the surface, the maximum number of knots was increased to 100 from the default of 20 (Figure 13). Maximum number of 100 knots means that the rectangular area will be divided into, at maximum, 100 pieces in both parameter directions, creating patches. The algorithm starts by dividing the whole area into a smaller number of patches and then increasing the number of patches where the error is large. By allowing a larger number of knots, the relative error between the patch placements and the actual data points is decreased. The algorithm tries to reach the set relative tolerance of $1.0E-6$ by adding more knots. The higher the number of knots, the better the approximation of the surface can be and smaller relative error, but the computational time increases also.

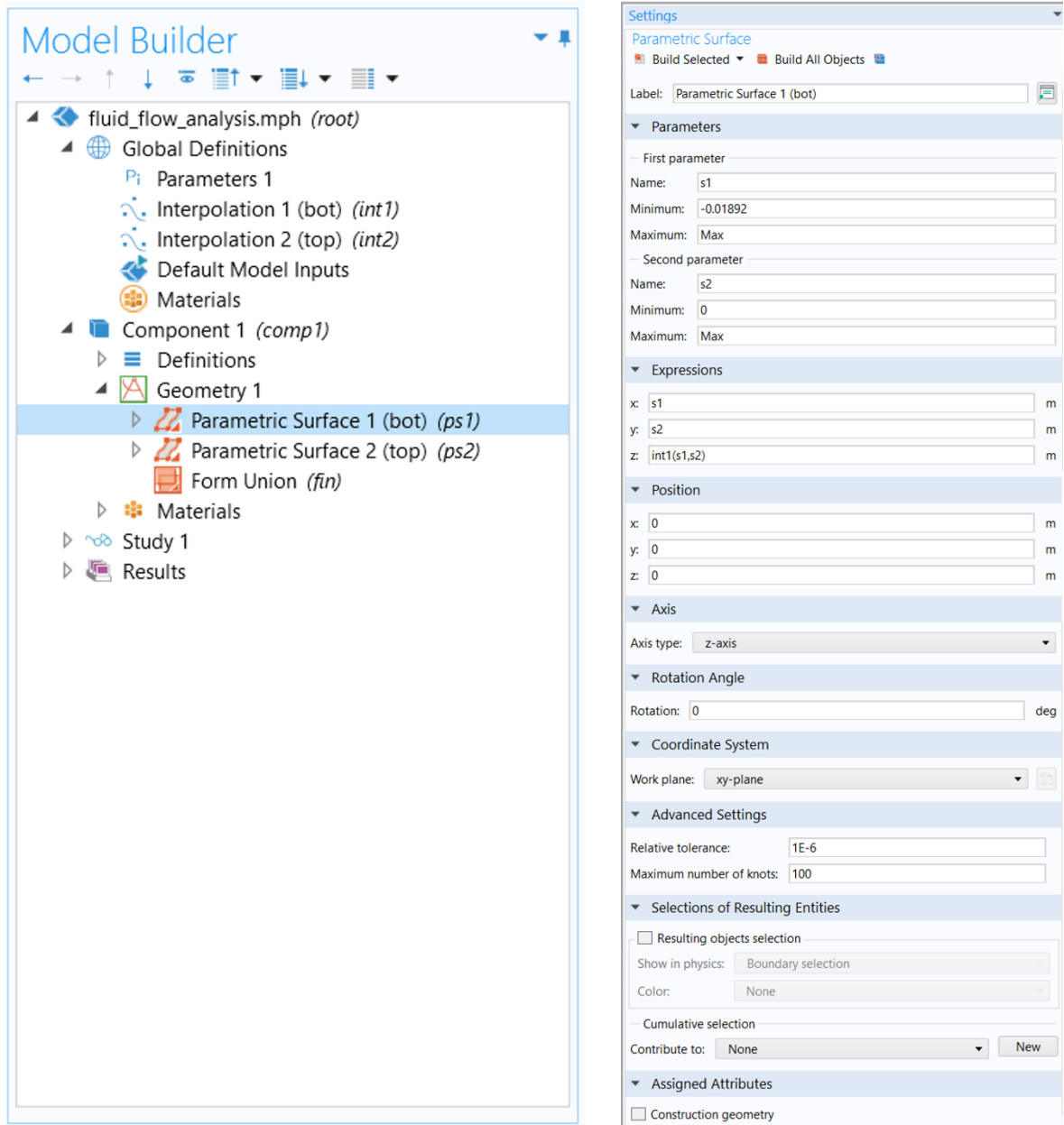


Figure 13. The Parametric Surface settings for the bottom surface of the fracture based on the point cloud interpolation function.

Parametric surface was created for both, top and bottom surface of the fracture. Figure 14 illustrates the two interpolated fracture surfaces. By changing the colors of one surface, it is possible to inspect the contact zones of the two fracture walls.

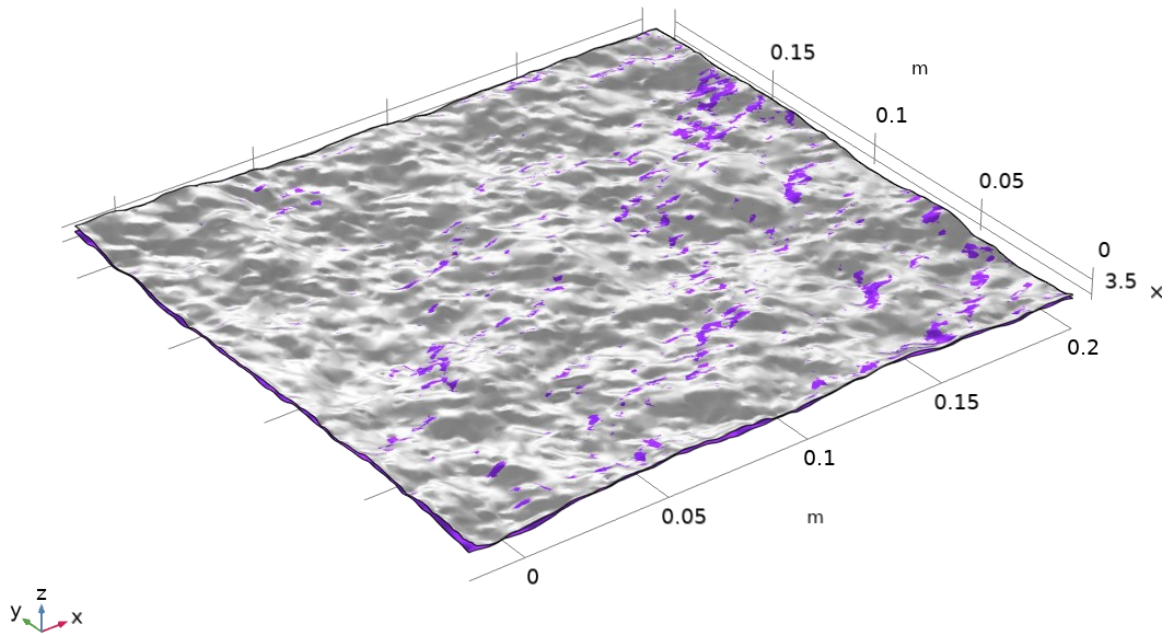


Figure 14. Parametric surfaces representing the bottom and top surfaces of the fracture. Bottom surface is colored purple to indicate the contact zones of the two fracture walls.

The next step in construction of the fracture geometry is to create a work plane for defining the fracture confined by the two fracture surfaces in 3D (Figure 15). The properties defining the location of the work plane are defined in Settings window. Plane type was set to Quick and the plane representing the work planes local coordinate system was set as xy-plane with no offset in the direction of z. Practically, the work plane is a plane that is set to locate under the fracture surface with corresponding coordinate system as the fracture.

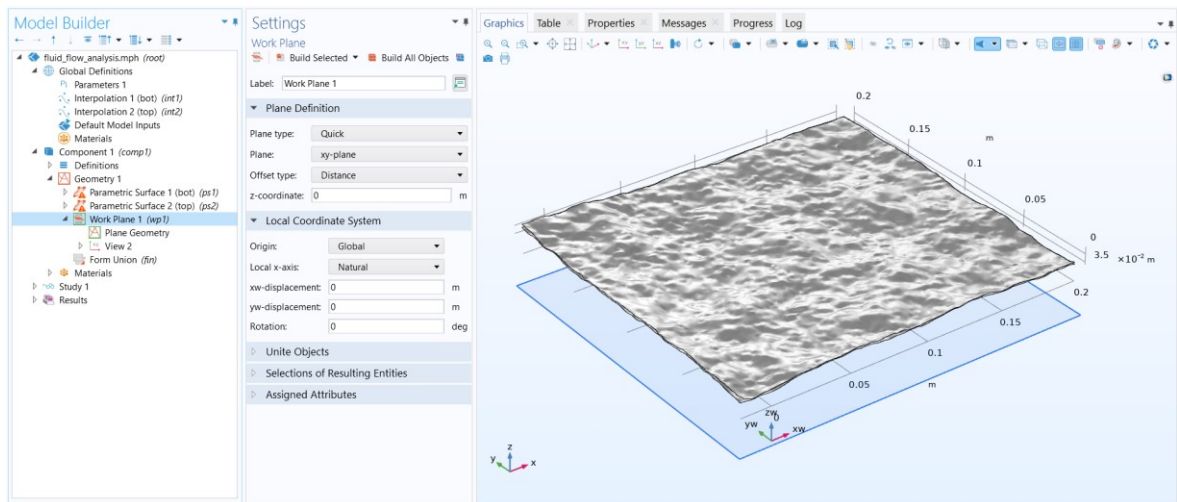


Figure 15. Creation of the work plane.

The geometry sequence for a work plane is defined and created under Plane Geometry node (Figure 16 and Figure 17). First, open curve polygon was defined according to the coordinates in x- and y-direction. Then, linear array of the polygon was created with Array. The desired geometry object that will be duplicated is selected as input. Array type was linear and the displacement between the linear polygons was set as 0,011 m (Figure 17). Last step was to unite the created polygons with Union. The geometry sequence was defined in similar manner for both, x- and y-directions.

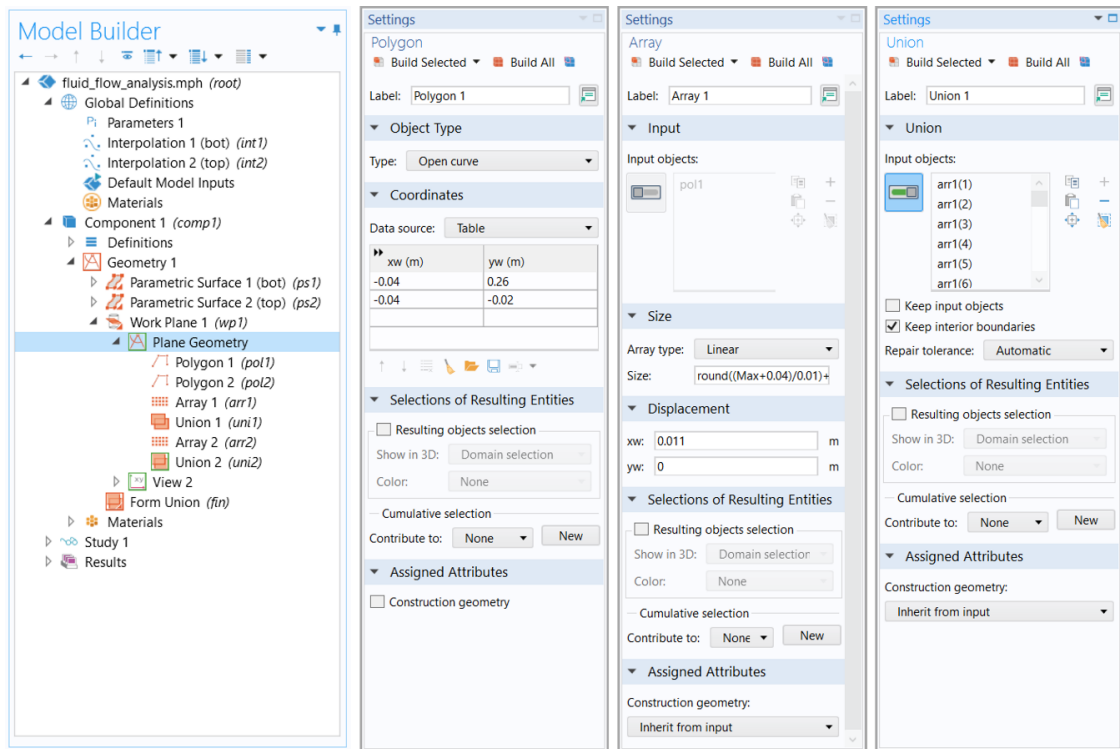


Figure 16. Creation of the geometry sequence for the work plane in the direction of y-axis.

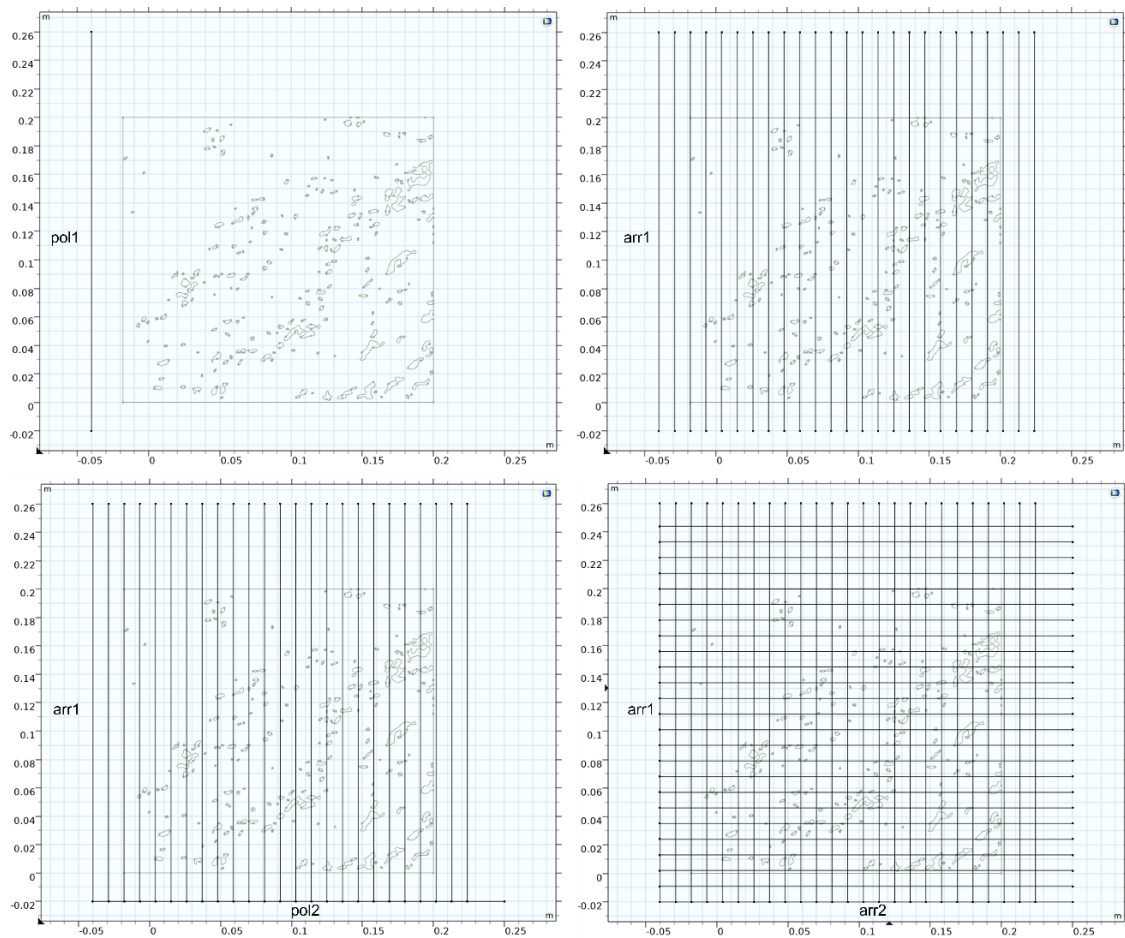


Figure 17. Creating the geometry sequence for a work plane with linear array in order to create block-shaped 3D object around the fracture. Projected fracture in grey.

Next, the united arrays of polygons from the work plane were extruded into 3D objects (Figure 18). The extrude distance from the work plane was set to 0,1 m so it reached over the fracture surfaces.

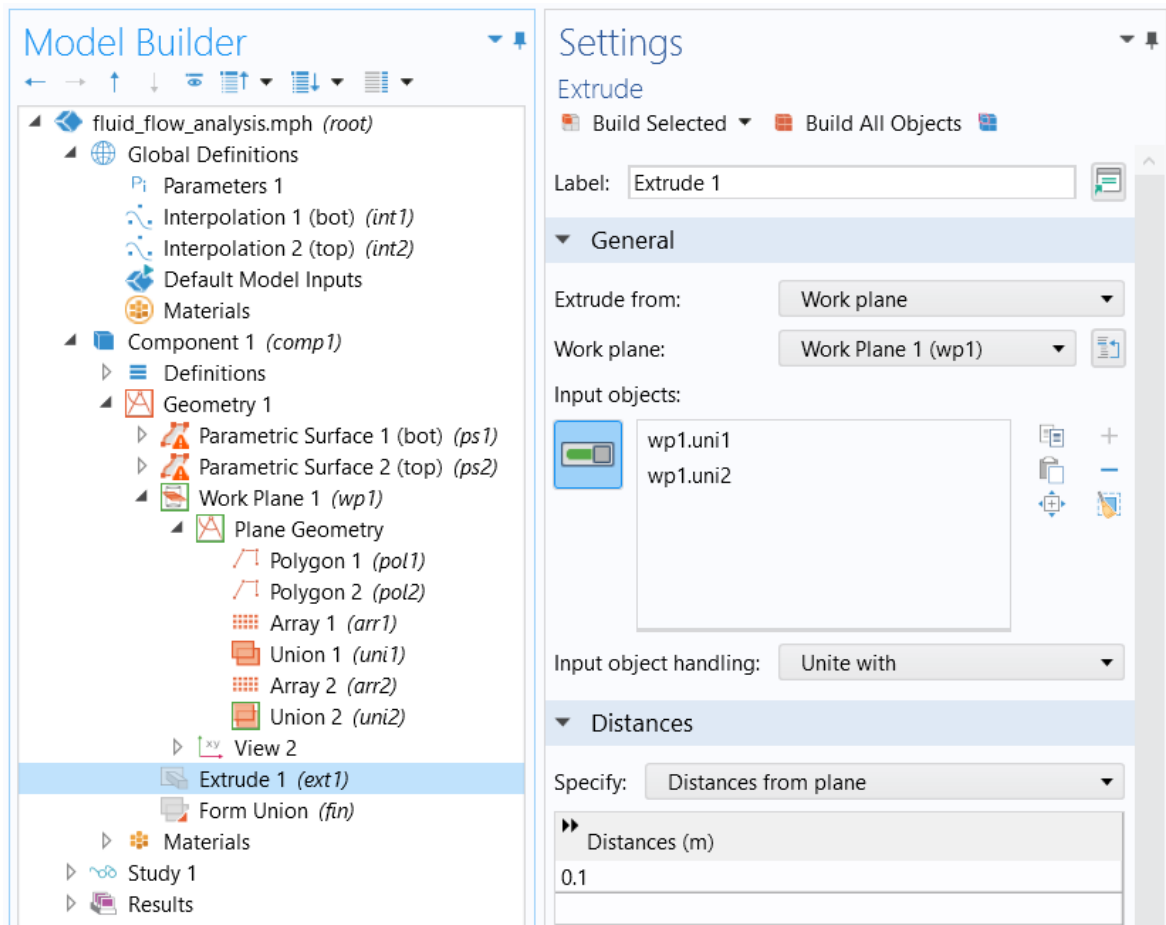


Figure 18. Extrude node in the model tree with the settings according to the model.

The graphic illustration of the Extrude operation before extruding is presented in Figure 19a. Figure 19b presents the graphic illustration of the Extrude operation after extruding.

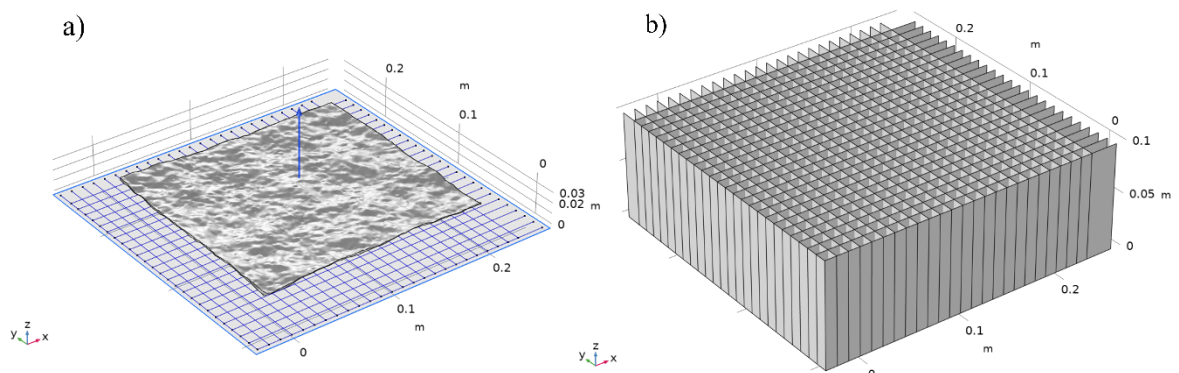


Figure 19. Graphic illustration of the Extrude operation a) before extruding and b) after extruding.

The Partition objects node provides a way to partition geometry objects as a Boolean operation. The Partition objects operation was used to divide the parametric surfaces to smaller domains by using the extruded geometry created in previous section (Figure 20).

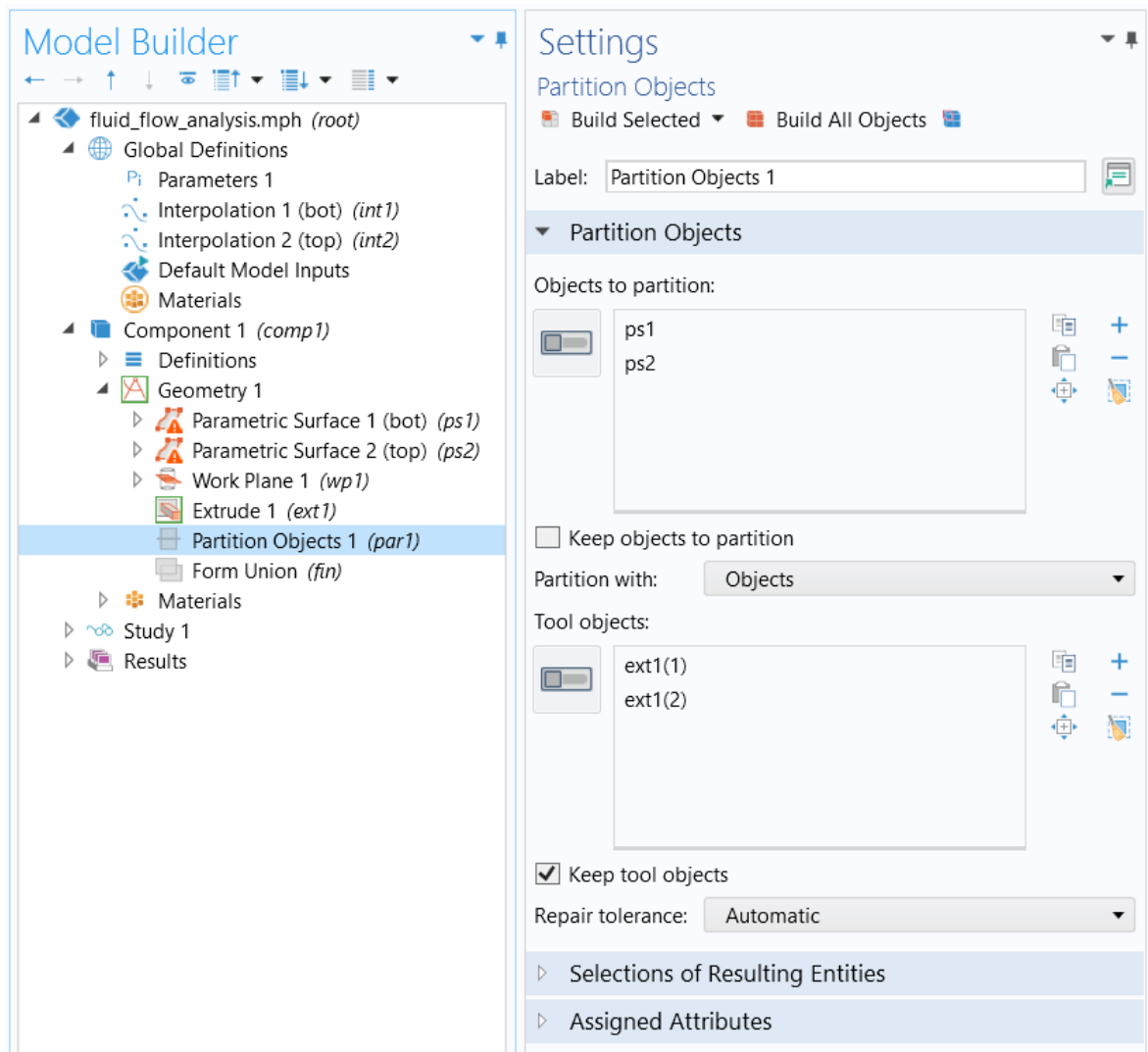


Figure 20. Partition objects node in the model tree with the settings according to the model.

Figure 21 presents the partitioned parametric surfaces that are divided into smaller domains.

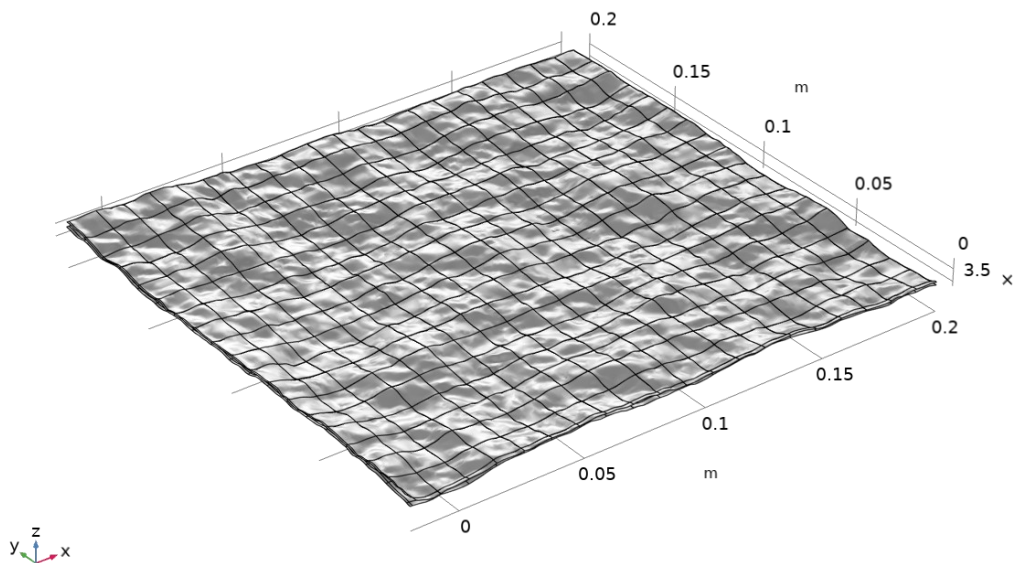


Figure 21. Graphic illustration of the partitioned parametric surfaces.

After Partition objects -operation, Union -operation was used to unite the partitioned parametric surfaces as one geometry (Figure 22).

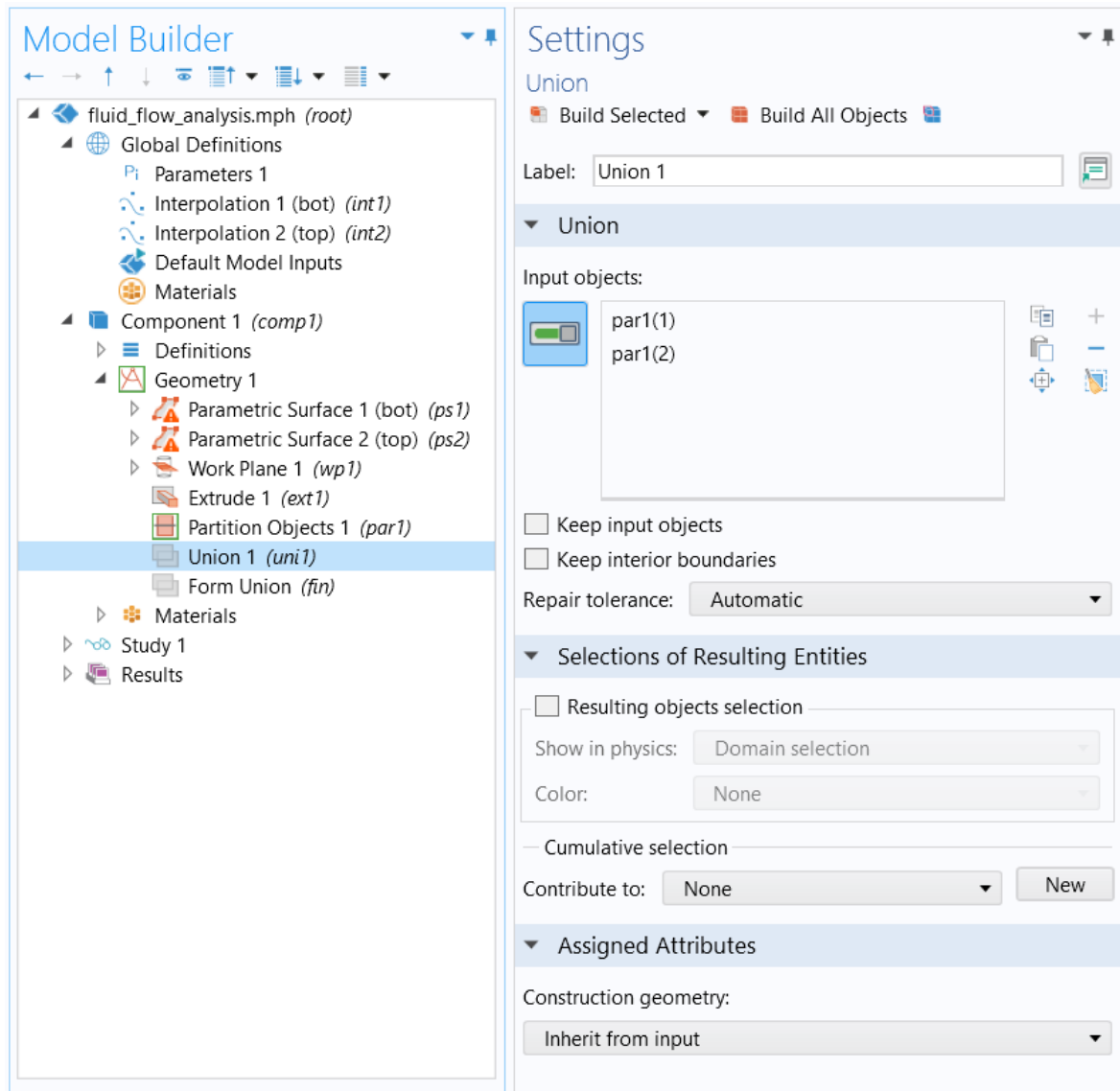


Figure 22. Union node in the model tree with the settings according to the model.

Block operation is used to create a block around the geometry. Solid block with the size and the shape as stated in Figure 23, was created around the united fracture geometry. Position of the block was defined as corner according to the x- y- and z- coordinates. Figure 24 presents the finished block.

Figure 24. Graphic illustration of the created block with united parametric surfaces visible.

Convert to Solid node unites and converts different geometry objects to a single solid object. In this thesis, Convert to Solid operation was used to convert the uni1, that comprise the parametric surfaces divided into domains, and the block solid, blk1, to one solid geometry csol1 (Figure 25).

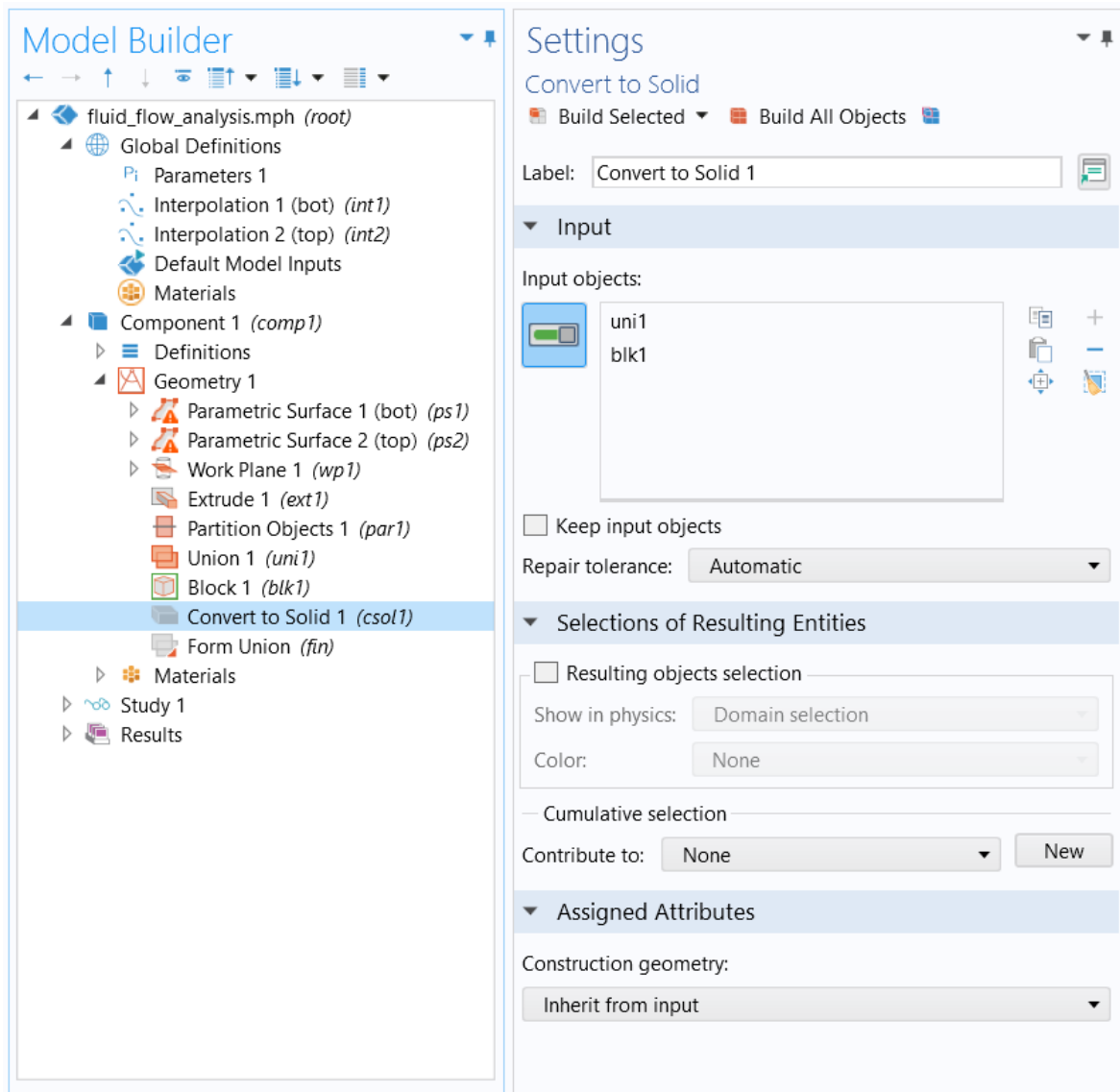


Figure 25. Convert to Solid node in the model tree with the settings according to the model.

Delete entities operation is used to delete desired objects or geometric entities from objects. After Convert to Solid operation, all irrelevant geometric entities were deleted from the model (Figure 26). Irrelevant, or excess, geometries were the solid block outside the fracture surfaces and the solid pieces representing the contact areas. Delete entities operation may also be used to fix meshing problems (see chapter 6.5).

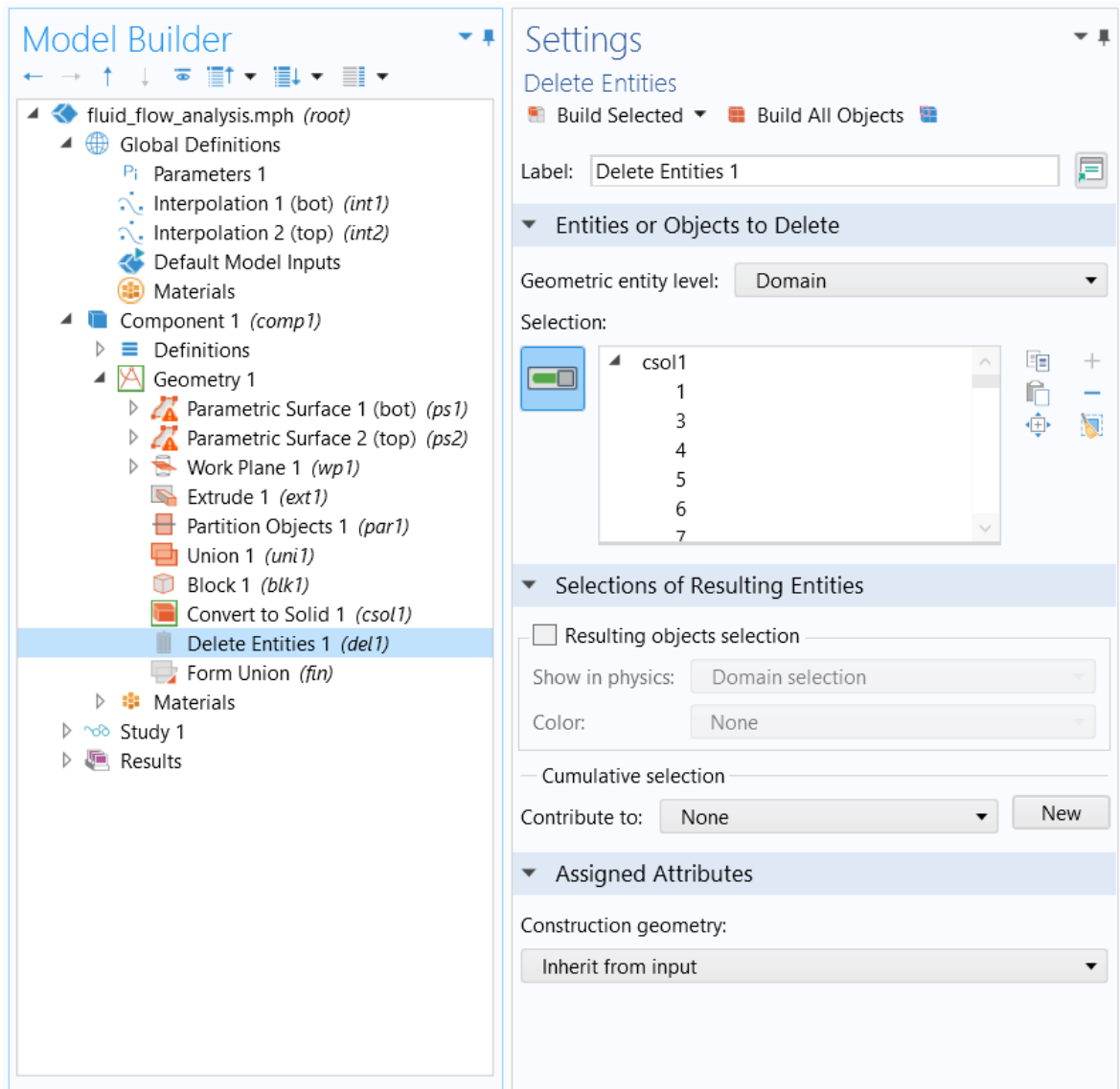


Figure 26. Delete entities node in the model tree with the settings according to the model.

The csol1 geometry converted in previous step comprise of several different solid objects, or in this case solid domains. These domains were the two sides of the solid block outside the fracture, the solid domains representing the contact zones inside the fracture and the solid representing the fracture volume. Figure 27 presents step by step how the excess entities are deleted and only the solid model representing the fracture remains for further processing.

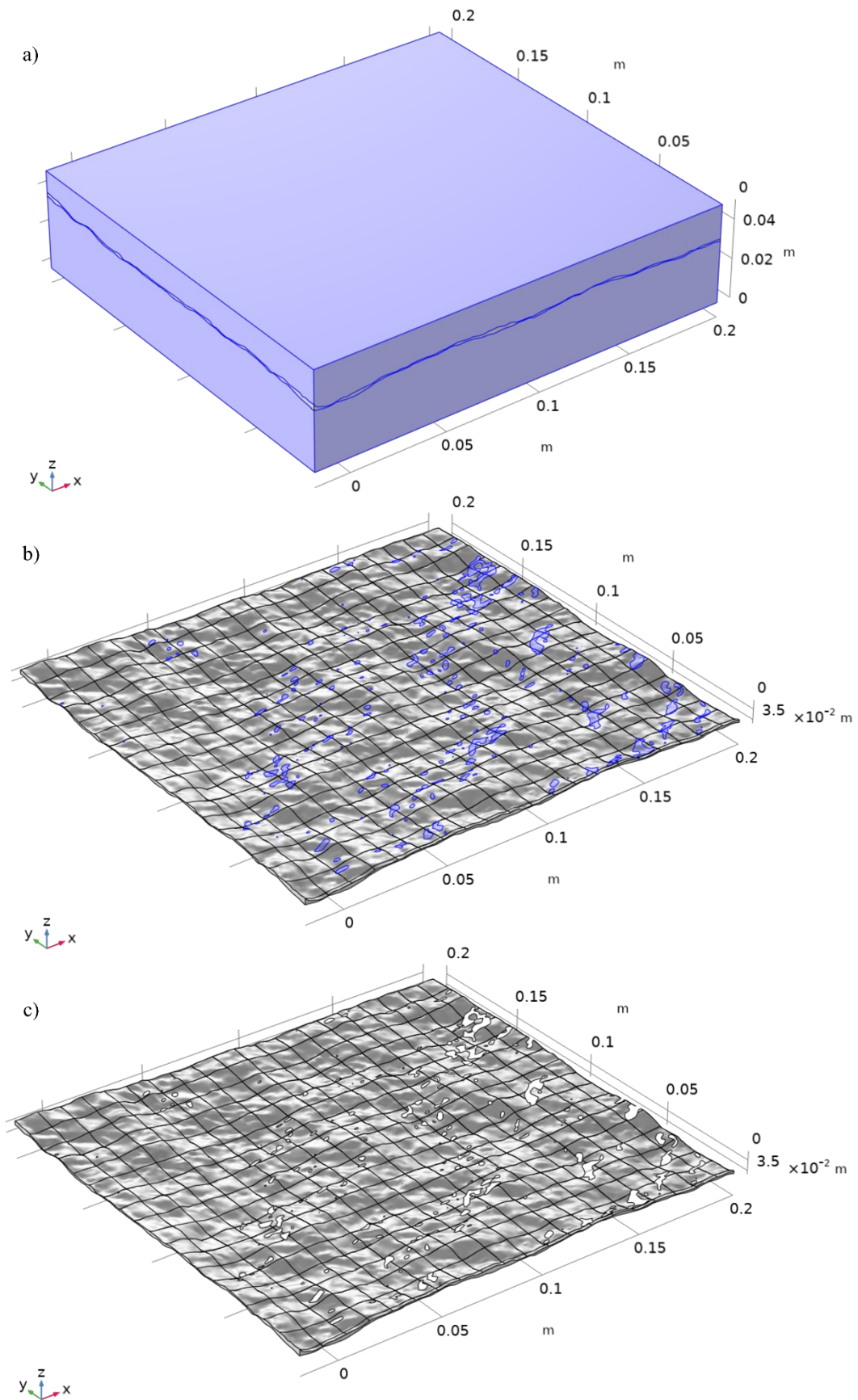


Figure 27. a) Block before deleting entities around the fracture. b) Fracture solid before deleting the purple contact zones. c) Finished solid fracture model with excess entities deleted.

The Partition objects operation was used second time to divide the fracture solid to smaller domains by using the extruded geometry created in previous section (Figure 28).

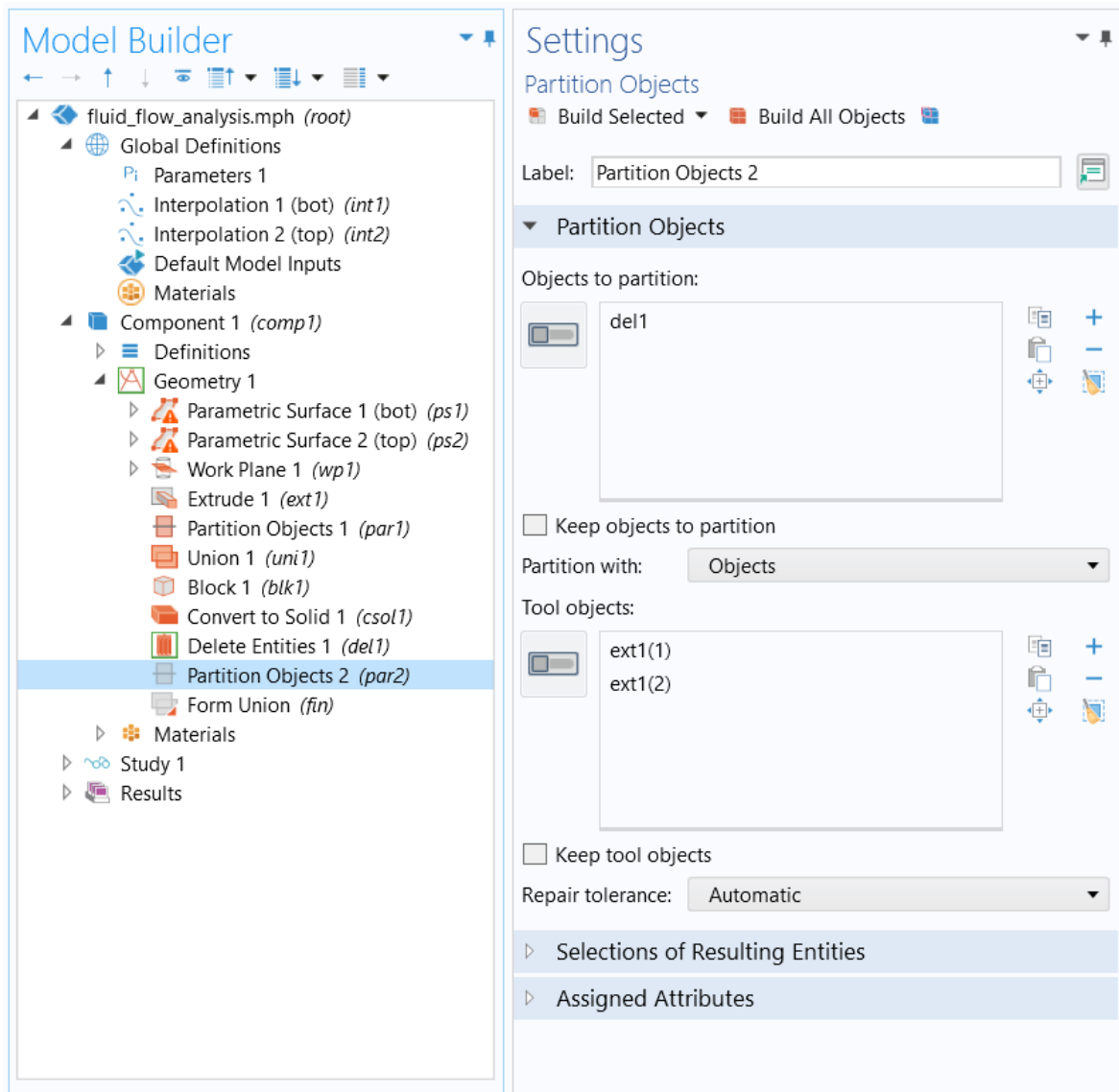


Figure 28. Partition objects node in the model tree with the settings according to the model.

To unite the geometry, COMSOL Multiphysics evaluates the geometry sequence from the top down (Figure 29). The final node in the geometry sequence before any virtual operations, the Form Union/Assembly node, determines how to form the geometry that is used for meshing and analysis possibly after also applying virtual operations (COMSOL 2021). There are two methods to form the geometry, which also determine the name of the node: Form Union or Form Assembly. The default method is to form a union. The software then forms a union from all geometry objects that the geometry sequence contains or creates. The union is divided into domains separated by boundaries according to the participating geometry objects. By default, COMSOL Multiphysics ensures continuity in the physics interface fields across interior boundaries (COMSOL 2021).

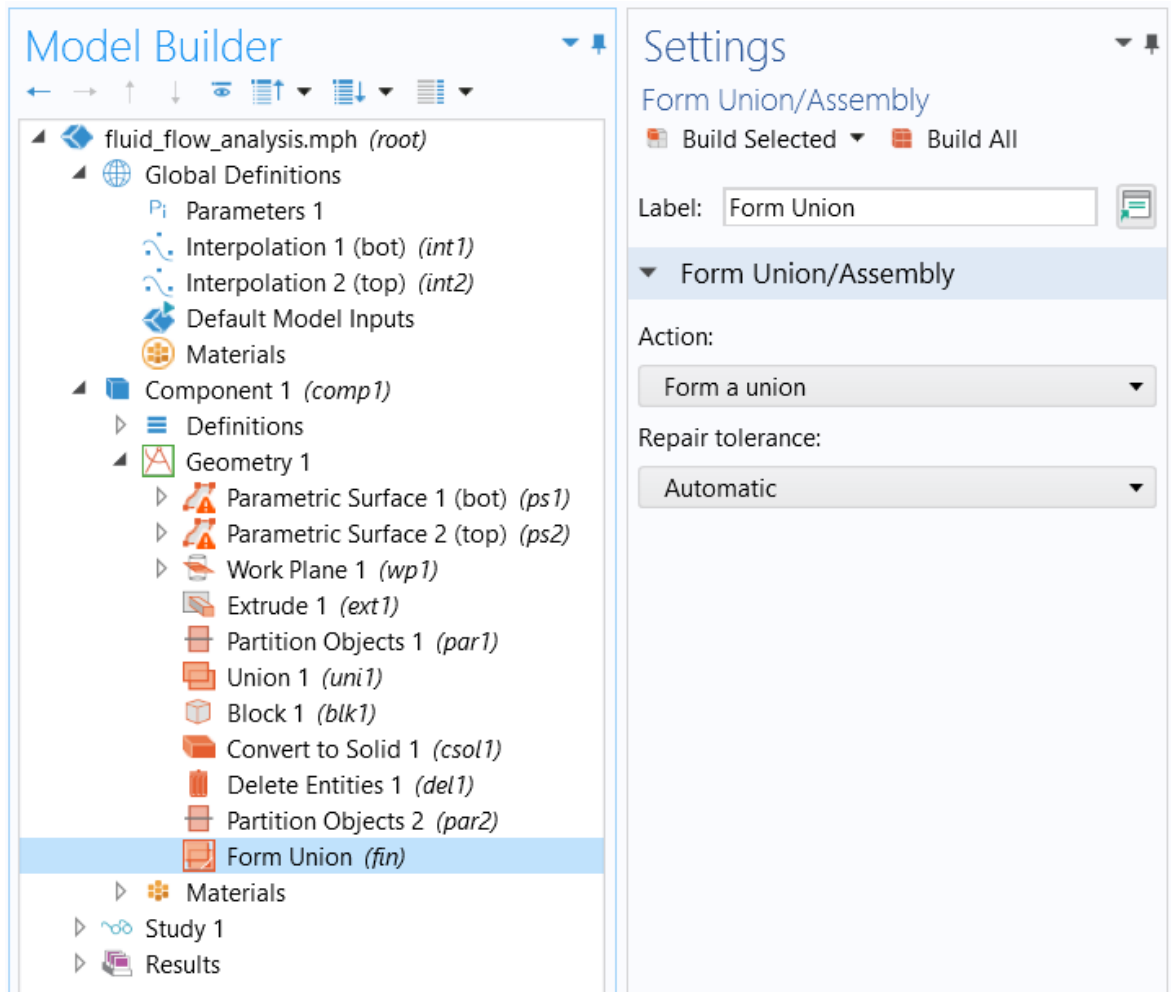


Figure 29. Form union node in the model tree with the settings according to the model.

Last step is to create Mesh Controlled Domains for more precise control of the mesh in specific regions of the geometry (Figure 30).

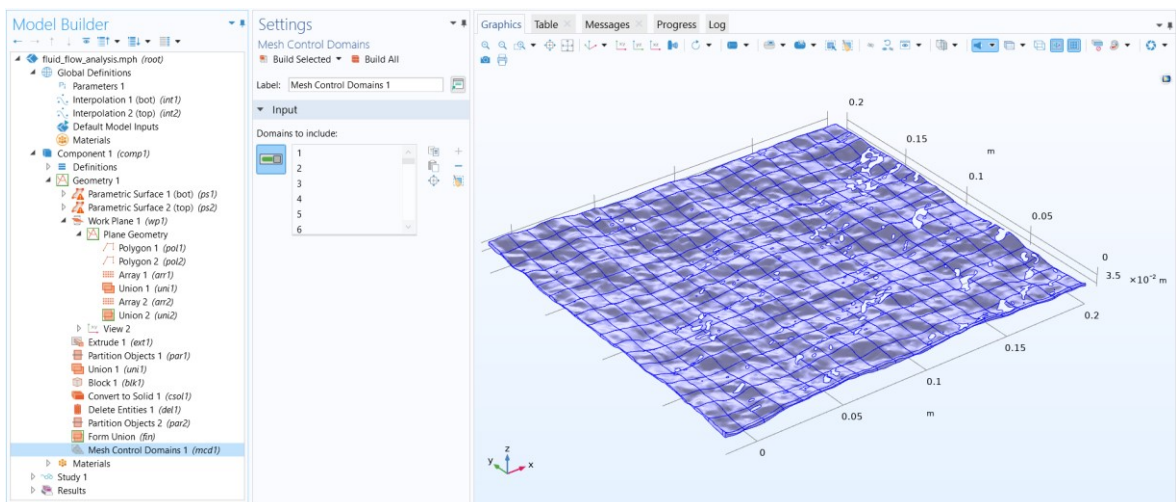


Figure 30. Mesh Control Domains node in the model tree and the creation of mesh control domains.

Figure 31 presents the finished geometry of the fracture ready for meshing.

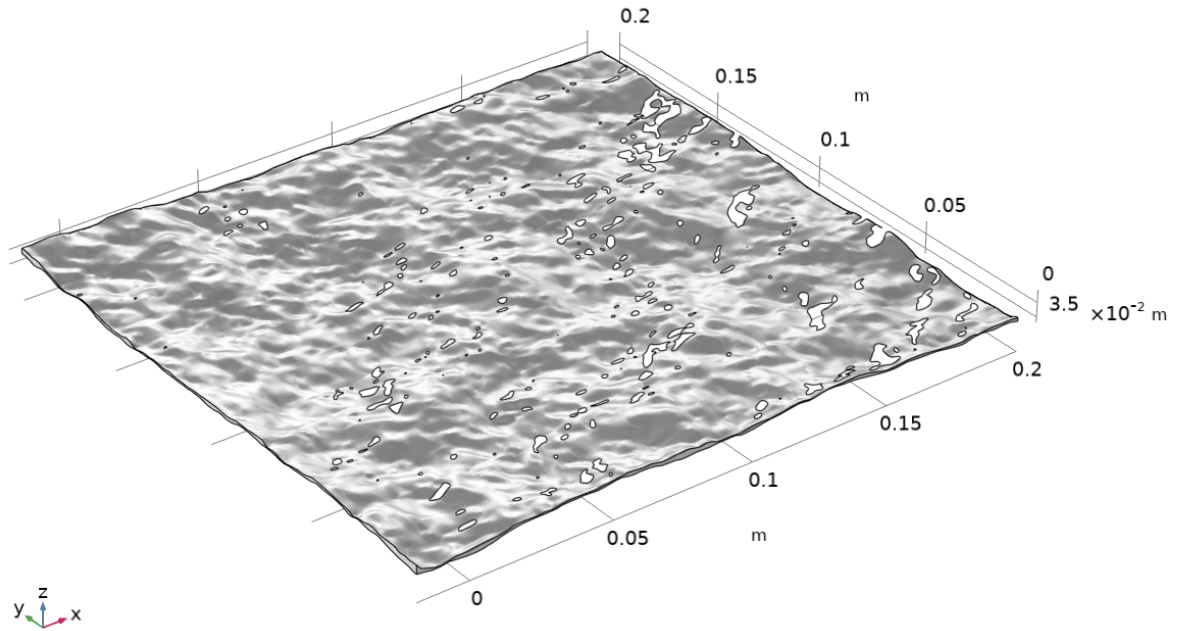


Figure 31. Finished geometry of the fracture.

6.3 Materials

Materials are added under the Materials node (Figure 32). Added materials can be predefined or user-defined and they include a number of physical properties with the values, expressions and functions to describe them. Since this thesis investigates fluid flow in rock fracture, the sole material to be added was water.

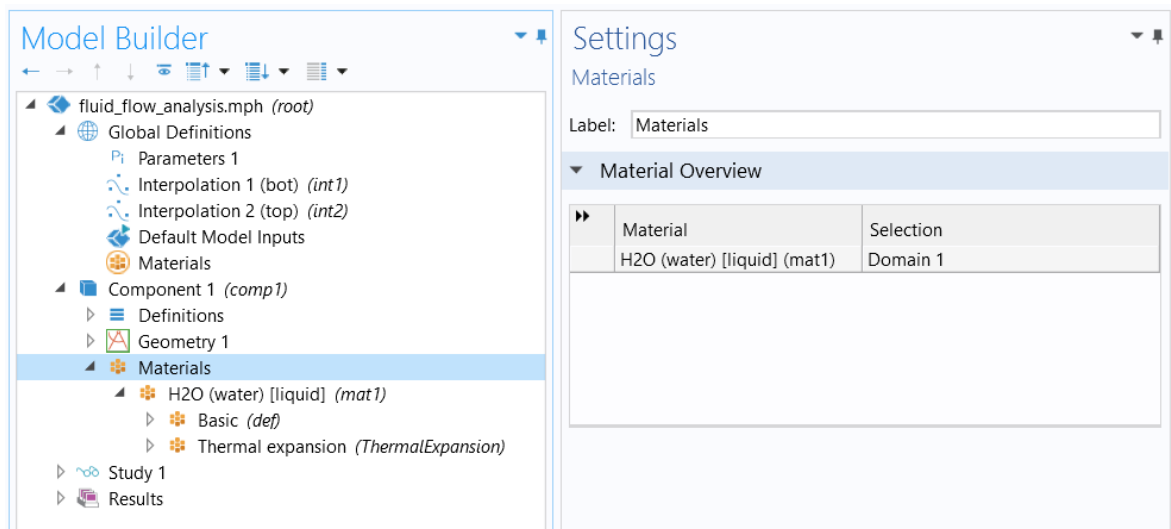
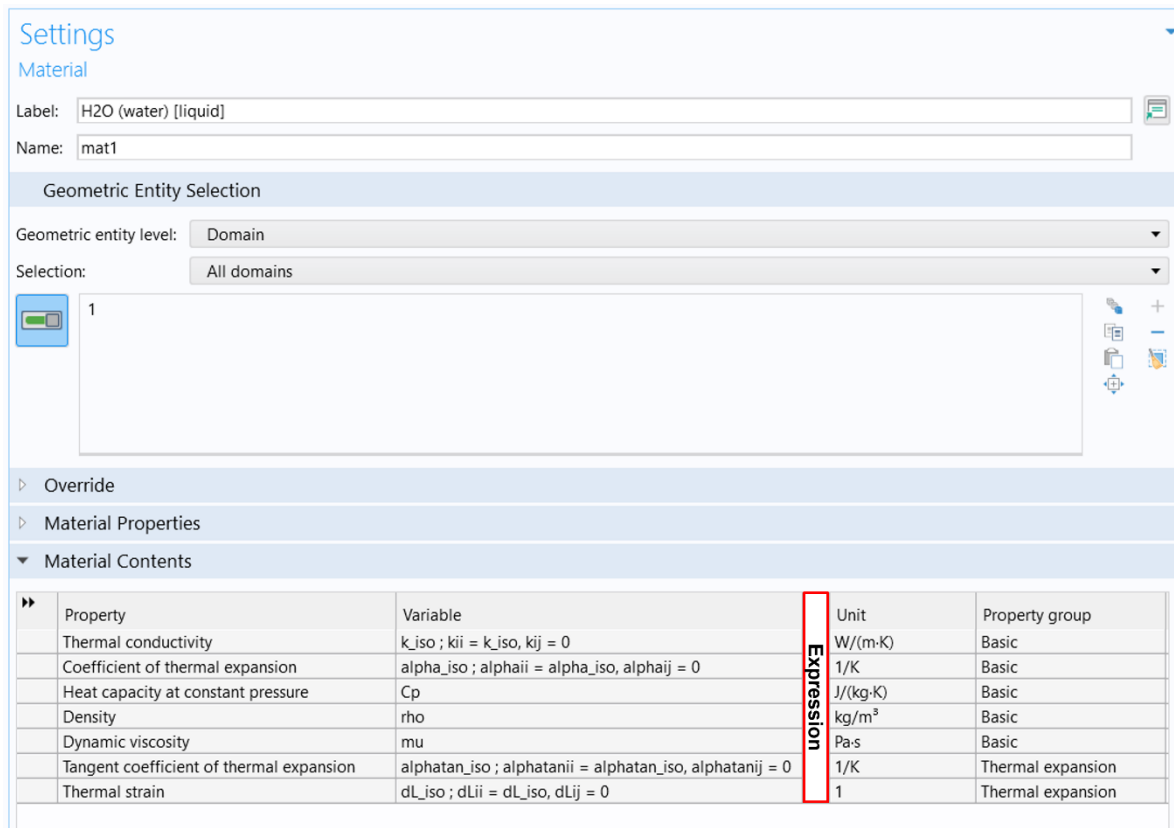


Figure 32. Materials-node in the Comsol model tree with the settings tab illustrating that the selected material is assigned for the whole fracture domain.

The basic property group defining material properties of water included input properties of temperature and volume reference temperature that describe the output properties thermal conductivity, coefficient of thermal expansion, heat capacity at constant pressure, density and dynamic viscosity. User-defined property group was added to define the thermal

expansion of water with input properties of temperature and volume reference temperature that describe tangent coefficient of thermal expansion and thermal strain (Figure 33).



Settings
Material

Label: H2O (water) [liquid]
Name: mat1

Geometric Entity Selection

Geometric entity level: Domain
Selection: All domains

1

► Override
► Material Properties
▼ Material Contents

Property	Variable	Expression	Unit	Property group
Thermal conductivity	k_{iso} ; $k_{ii} = k_{iso}$, $k_{ij} = 0$		W/(m·K)	Basic
Coefficient of thermal expansion	α_{iso} ; $\alpha_{phaii} = \alpha_{iso}$, $\alpha_{phaij} = 0$		1/K	Basic
Heat capacity at constant pressure	C_p		J/(kg·K)	Basic
Density	ρ		kg/m ³	Basic
Dynamic viscosity	μ		Pa·s	Basic
Tangent coefficient of thermal expansion	α_{phatan_iso} ; $\alpha_{phatanii} = \alpha_{phatan_iso}$, $\alpha_{phatanij} = 0$		1/K	Thermal expansion
Thermal strain	dL_{iso} ; $dL_{ii} = dL_{iso}$, $dL_{ij} = 0$		1	Thermal expansion

Figure 33. General settings for water. Expressions of properties are presented more detail in Figure 35 and Figure 36.

Piecewise functions were used to specify the basic properties of water as well as thermal expansion properties of the water. A Piecewise function is created by splicing together several functions, each defined on one interval (COMSOL 2021). The definition of argument, extrapolation and smoothing methods as well as the functions and their intervals are needed to define each piecewise function. The piecewise function is a function of one variable with different definitions on different intervals, which must not overlap or have any holes between them (COMSOL 2021).

9 piecewise functions were used to define basic properties of water and thermal expansion was defined with 2 piecewise functions (Figure 34)

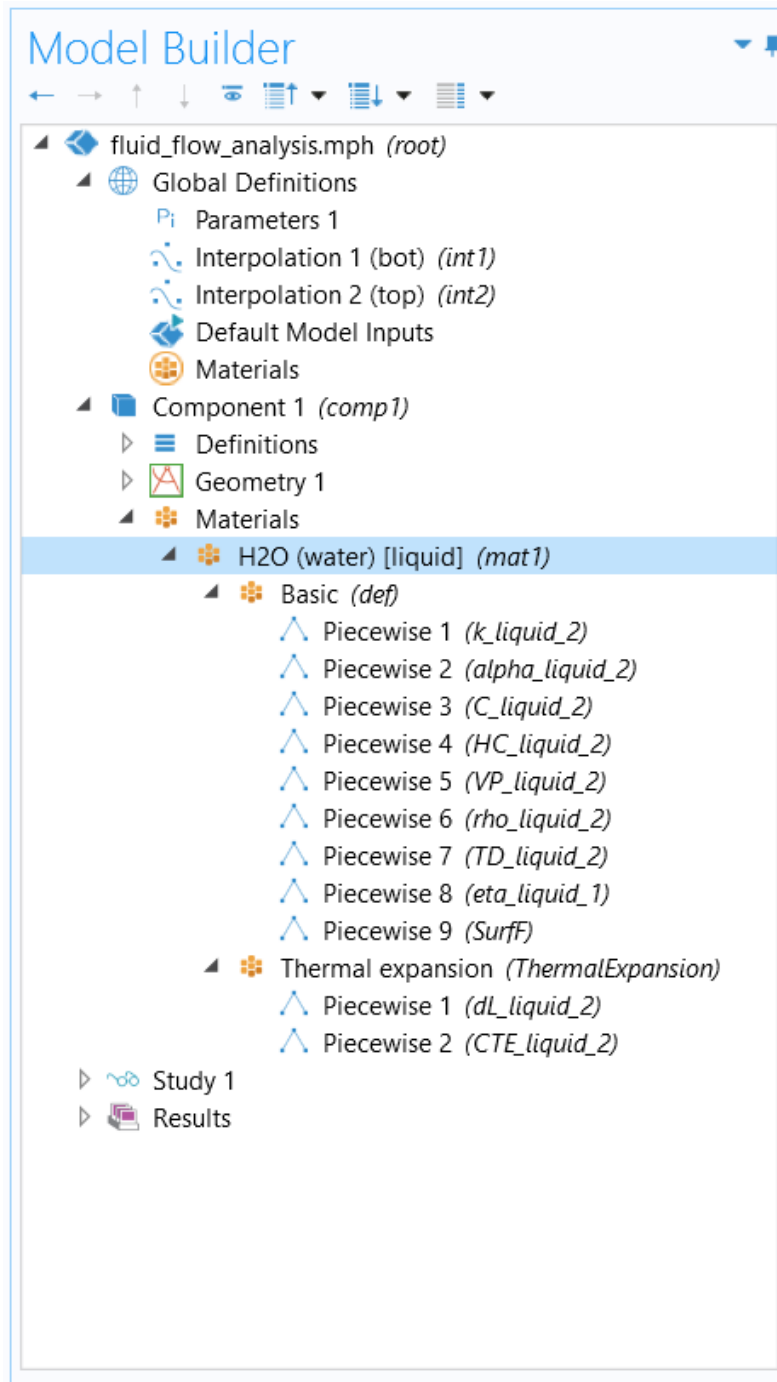


Figure 34. Basic and Thermal expansion property groups defining the Material (water). The labels of the functions describing the properties is shown under Basic property groups and Thermal expansion property groups sub-branch. The function name is shown in brackets.

Example of how the piecewise functions are used to describe the basic properties of water is shown in Figure 35 and in Table 3. Example of how the piecewise functions are used to describe the properties of thermal expansion of water is shown in Figure 36 and in Table 4.

Settings

Basic

Label: Basic

Name: def

▼ Output Properties

Property	Expression
Thermal conductivity	$k_{\text{liquid_2}}(T[1/K])/W/(m^2K)$
Coefficient of thermal expansion	$(\alpha_{\text{liquid_2}}(T[1/K])/(1/K) + (Tempref-293[K]) \cdot f(\text{abs}(T-Tempref)) > 1e-3, \alpha_{\text{liquid_2}}(T[1/K])/(1/K) - \alpha_{\text{liquid_2}}(Tempref[1/K])/(1/K)) / (T-Tempref, d(\alpha_{\text{liquid_2}}(T[1/K])/(1/K), T)) / (1 + \alpha_{\text{liquid_2}}(Tempref[1/K])/(1/K) \cdot (Tempref-293[K]))$
Heat capacity at constant pressure	$C_{\text{liquid_2}}(T[1/K])/J/(kg \cdot K)$
Density	$\rho_{\text{liquid_2}}(T[1/K])/kg/m^3$
Dynamic viscosity	$\eta_{\text{liquid_1}}(T[1/K])/Pa \cdot s$

Expression:

▼ Model Inputs

Physical quantity	Variable
Temperature	T
Volume reference temperature	Tempref

▼ Local Properties

Name	Expression	Unit	Description
HC	$HC_{\text{liquid_2}}(T[1/K])/J/(mol \cdot K)$	$J/(mol \cdot K)$	
VP	$VP_{\text{liquid_2}}(T[1/K])/Pa$	Pa	
TD	$TD_{\text{liquid_2}}(T[1/K])/m^2/s$	m^2/s	
SurfF	$SurfF(T[1/K])/N/m$	N/m	

Figure 35. Settings for the Basic property group of water.

Table 3. Piecewise functions describing the Basic property group of water.

Function name	Start	End	Function
k_liquid_2	275	370	$-9.003748E-01 + 8.387698E-03 \cdot T^1 - 1.118205E-05 \cdot T^2$
alpha_liquid_2	273	283	$1.032507E-02 - 7.62815E-05 \cdot T^1 + 1.412474E-07 \cdot T^2$
	283	373	$-2.464185E-03 + 1.947611E-05 \cdot T^1 - 5.049672E-08 \cdot T^2 + 4.616995E-11 \cdot T^3$
C_liquid_2	293	373	$4.03584079E+03 + 4.92312034E-01 \cdot T^1$
HC_liquid_2	293	373	$7.26451184E+01 + 8.86161577E-03 \cdot T^1$
VP_liquid_2	280	600	$(\exp((-2.00512183E+03/T - 5.5657E-01 \cdot \log_{10}(T) + 9.89879E+00 - 1.11169009E+07/T^3) \cdot \log_{10}(10.0))) \cdot 1.3332E+02$
rho_liquid_2	273	283	$9.727584E+02 + 2.084E-01 \cdot T^1 - 4.0E-04 \cdot T^2$
	283	373	$3.4528E+02 + 5.749816E+00 \cdot T^1 - 1.57244E-02 \cdot T^2 + 1.264375E-05 \cdot T^3$
TD_liquid_2	273	333	$8.04E-08 + 2.0E-10 \cdot T^1$
eta_liquid_1	265	293	$5.948859E+00 - 8.236196E-02 \cdot T^1 + 4.287142E-04 \cdot T^2 - 9.938045E-07 \cdot T^3 + 8.65316E-10 \cdot T^4$
	293	353	$4.10191E-01 - 4.753985E-03 \cdot T^1 + 2.079795E-05 \cdot T^2 - 4.061698E-08 \cdot T^3 + 2.983925E-011 \cdot T^4$
	353	423	$3.625638E-02 - 3.265463E-04 \cdot T^1 + 1.127139E-06 \cdot T^2 - 1.75363E-09 \cdot T^3 + 1.033976E-012 \cdot T^4$
SurfF	274	568	$7.739832E-02 + 2.071003E-04 \cdot T^1 - 1.23147E-06 \cdot T^2 + 2.344068E-09 \cdot T^3 - 3.033107E-012 \cdot T^4 + 1.758716E-015 \cdot T^5$
	568	647	$-1.093735E+02 + 9.291756E-01 \cdot T^1 - 3.154159E-03 \cdot T^2 + 5.351438E-06 \cdot T^3 - 4.539449E-09 \cdot T^4 + 1.540327E-12 \cdot T^5$

Settings

Thermal Expansion

Label: Thermal expansion

Name: ThermalExpansion

▼ Output Properties

Property	Variable	Expression	Unit	Size	Info
Tangent coefficient of thermal expansion	alphaniso ; alphanii = ...	CTE_liquid_2(T[1/K])/[1/K]	1/K	3x3	
Thermal strain	dL_iso ; dLii = dL_iso, dLij = ...	(dL_liquid_2(T[1/K]) - dL_liquid_2(Tpref[1/K]))/(1 + dL_liquid_2(T[1/K]))	1	3x3	

Expression:

▼ Model Inputs

Physical quantity	Variable
Temperature	T
Volume reference temperature	Tpref

Local Properties

Figure 36. Settings for the Thermal expansion property group of water.

Table 4. Piecewise functions describing the Thermal expansion property group of water.

Function name	Start	End	Function
dL_liquid_2	273	283	$8.486158\text{E-}03 - 6.947021\text{E-}05 \cdot T^1 + 1.333373\text{E-}07 \cdot T^2$
	283	373	$2.32446637\text{E-}01 - 2.030447\text{E-}03 \cdot T^1 + 5.510259\text{E-}06 \cdot T^2 - 4.395999\text{E-}09 \cdot T^3$
CTE_liquid_2	273	283	$-6.947321\text{E-}05 + 2.666746\text{E-}07 \cdot T^1$
	283	293	$-1.363715\text{E-}02 + 8.893977\text{E-}05 \cdot T^1 - 1.43925\text{E-}07 \cdot T^2$
	293	373	$-2.03045\text{E-}03 + 1.102052\text{E-}05 \cdot T^1 - 1.3188\text{E-}08 \cdot T^2$

6.4 Physical model

Next step in compiling the model is to choose the physical model which for this thesis was Laminar flow model. The Laminar flow interface is used to compute the velocity and pressure fields for the flow of a single-phase fluid in the laminar flow regime (COMSOL 2021). Figure 37 presents the model tree for the physical model. The default nodes in Laminar flow are Fluid properties, Initial values and Wall. Inlet and Outlet nodes were also added. The Fluid Properties node adds the momentum and continuity equations solved by the physics interface and the node also provides an interface for defining the material properties of the fluid (COMSOL 2021). Initial conditions for a transient simulation or an initial guess for a nonlinear solver in a stationary simulation are defined in the Initial Values node (COMSOL 2021). The Wall node includes a set of boundary conditions describing fluid-flow conditions at stationary, moving, and leaking walls (COMSOL 2021). Inlet node is used on boundaries for which there is a net flow into the domain and Outlet node is used on boundaries for which there is a net outflow from the domain (COMSOL 2021). Suitable initial and boundary conditions are assigned also in the Physical model section and they can be assigned for the whole model or manually select the desired domains.

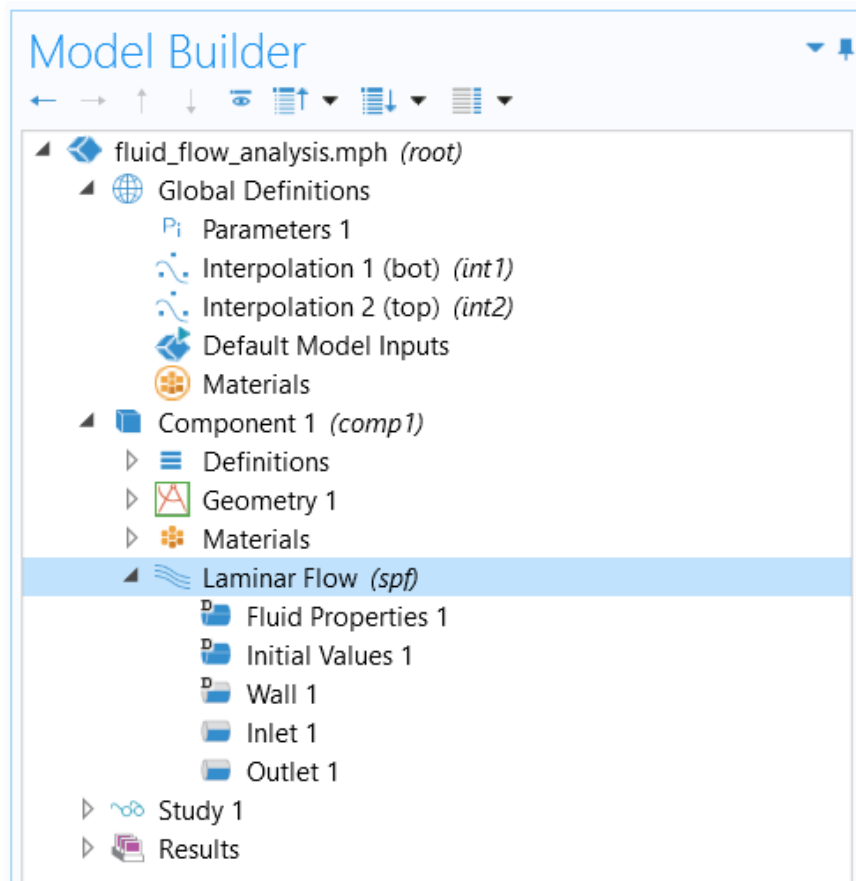


Figure 37. Physical model node in the model tree with the Fluid properties, Initial values, Wall, Inlet and Outlet nodes.

Figure 38 and Figure 39 present the settings for Fluid properties, Initial values, Wall, Inlet and Outlet nodes. Inlet and outlet boundaries were manually selected according to the flow direction (Figure 39). The top and bottom surfaces and the side boundaries of the fracture were defined as impermeable and non-slip boundaries and constant water pressure was applied along the inlet and zero pressure alongside the outlet (Figure 40).

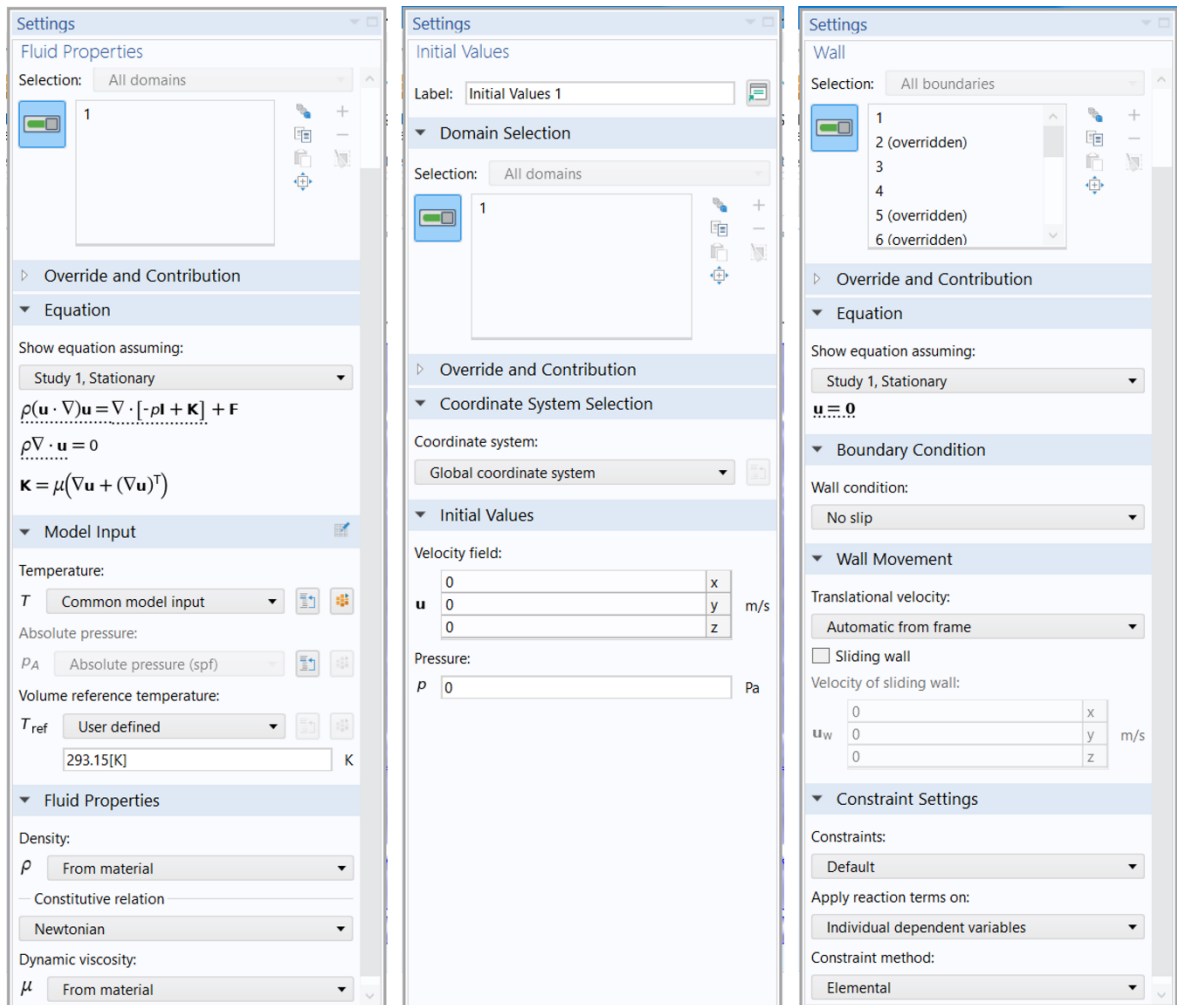


Figure 38. Settings for fluid properties, initial values and wall for this thesis fluid flow simulation.

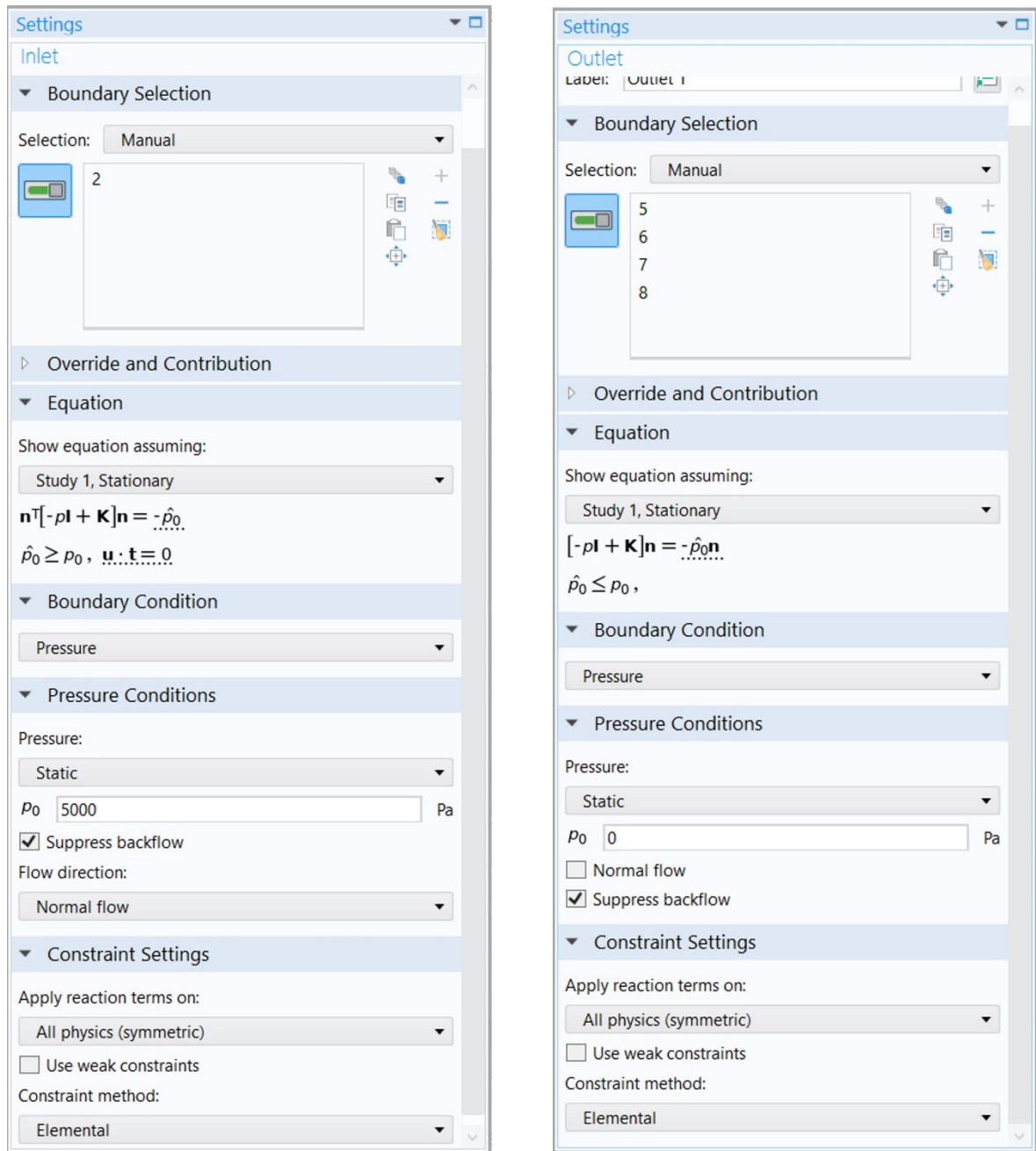


Figure 39. Settings for inlet and outlet for 5 KPa fluid flow simulation.

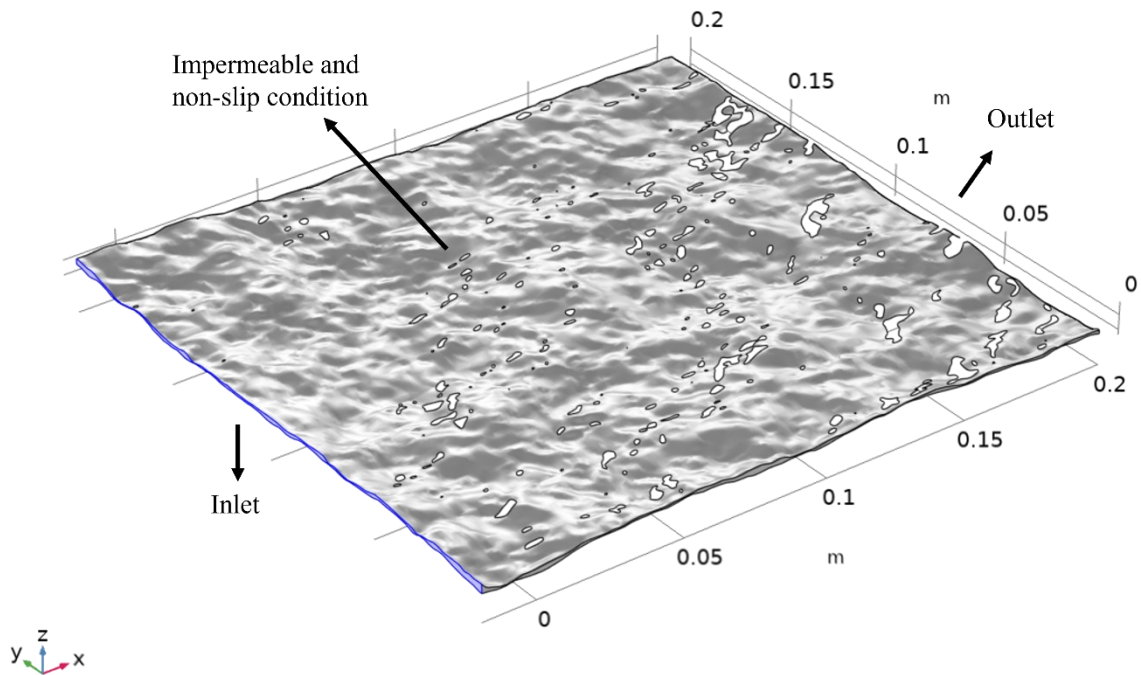


Figure 40. Boundary conditions for the fluid flow simulation with fluid flow along x-axis without normal stress. Inlet is marked with blue.

6.5 Meshing

Last step before the numerical simulation is meshing. Meshing is created under the Mesh node the model tree to enable a numerical solution of the problem. The mesh for this thesis was created by using automated ‘physics-controlled mesh’-option by COMSOL with the pre-defined element size ‘normal’ (Figure 41). Number of elements in the mesh was 1 291 592, maximum element size was 2.23×10^{-3} m and minimum element size was 1.43×10^{-5} m. The average element quality was 0.5226. For mesh quality measures, a quality of 1 is the best possible quality, indicating an optimal element in the chosen quality measure. Mesh quality of 0 represents a degenerated element with poor quality.

The selection of mesh element size is a compromise between precision and calculation time. More precise results may be achieved with finer mesh but with a cost of long calculation time. Mesh element quality may also be improved by deleting the poor zones next to contact areas but that would transform the model out of the real-life fracture that the modelling was trying to mimic. Detail of the finished mesh with element quality plotted on it, is presented in Figure 42.

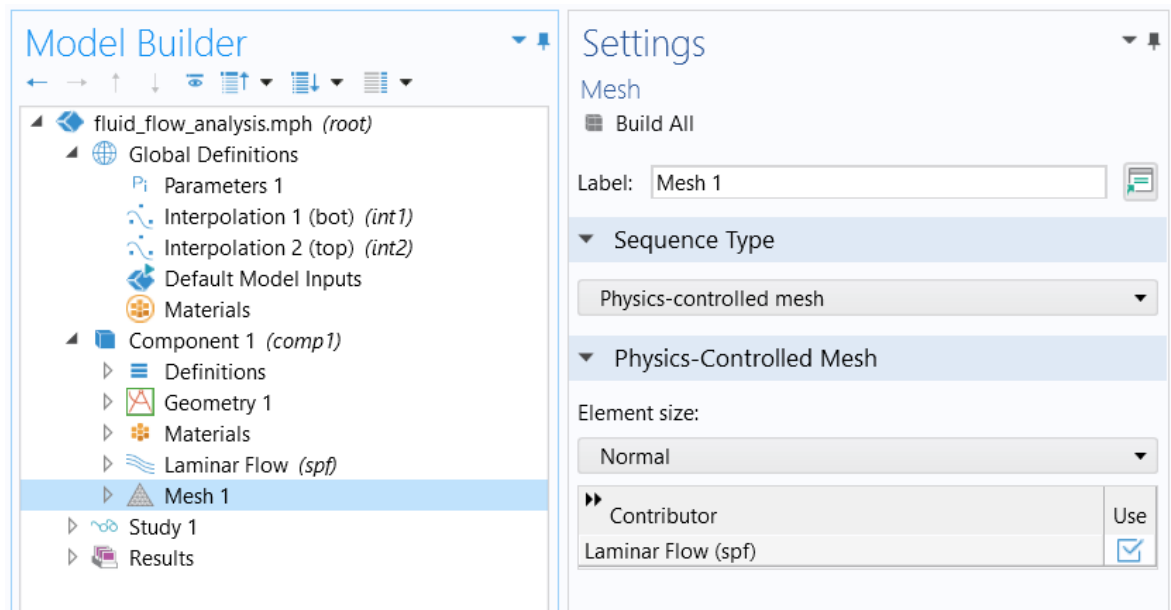


Figure 41. Mesh node in the model tree with the settings for the fluid flow simulation.

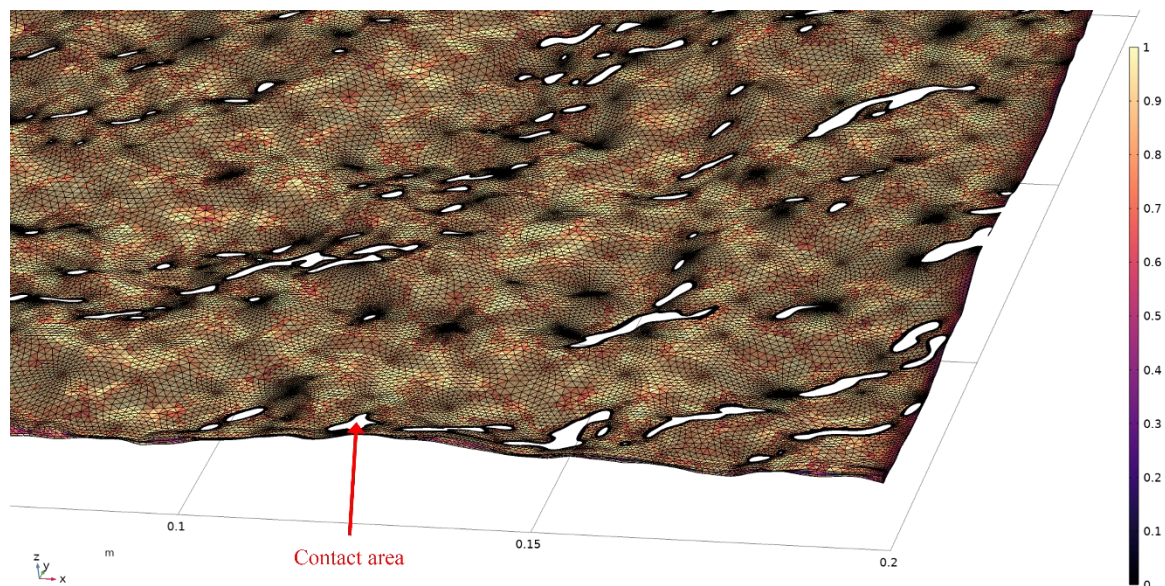


Figure 42. Detail of the normal-sized mesh with contact areas indicated with arrow. Quality of 1 is the best possible element quality and 0 represent poor quality.

Meshing is always dependent on the geometry and the quality of mesh may change when the geometry is altered. Intersections, sharp angles in the geometry or thin surfaces can create problems and errors to the meshing of the model. With physics-controlled mesh, over meshing can also create problems. The possible meshing problems can be fixed by deleting the problematic area and remeshing the model. The method of fixing the meshing problem starts by drawing a pre-defined shape such as cylinder over the problematic area. Then, a Boolean function can be used to delete the intersection between the 3D shape and the fracture surface after which the geometry can be meshed again. COMSOL has also automatic Mesh repair -function that may help with the meshing problems.

6.6 Solver

The solutions for the models created in COMSOL are predominantly produced either with stationary or time-dependent solver. The solver settings can be modified to affect for instance the computation error, maximum number of iterations or iteration termination conditions. Also, the numerical data in the simulations can be selectively saved based on what outcomes the user needs. Stationary solver with default solver settings was used for this thesis (Figure 43).

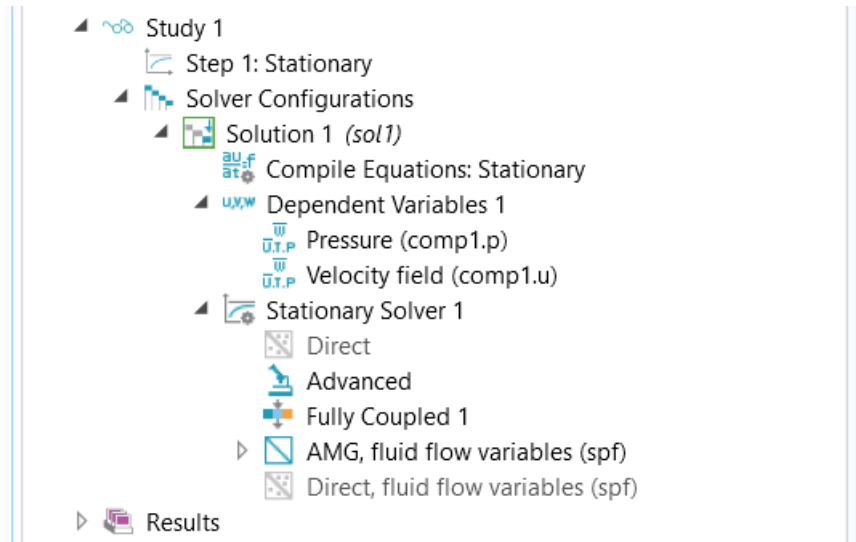


Figure 43. Study node and the Stationary solver for this thesis in the model tree of COMSOL.

The results from the numerical simulations are automatically presented and post-processed in COMSOL although it is also possible to create almost an unlimited number of user-defined graphs and tables. Various numerical values can be calculated based on the results of the numerical simulations and all numerical data can be stored in a text document, which can be obtained, for example, in Excel for processing. The results acquired in this thesis are discussed more detail in the Section 7.

7 Simulation results

The main results from the fluid flow simulations for this thesis are presented and discussed in this section. The results of 20 fluid flow simulation are presented in section starting from validating the model, which is followed by hydraulic aperture of the fracture, fluid flow velocity inside the fracture, streamlines and finally pressure contours. The experimental work by Torkan et al. (2021) was used as a reference case for validating the results of the numerical simulation. Tabulated results are provided in Appendix A.

The contact areas are important factor governing the route and the behaviour of the fluid flow inside the fracture. The flow regime itself is governed by the pressure gradient combined with the morphology of the fracture. With rock sample 05, the contact zones are spread mainly on the lower right side and the center of the fracture (Figure 44). The distribution of the contact areas would suggest that the flow through x-axis would concentrate on the upper side of the fracture and the flow through y-axis would concentrate on the center of the fracture. The effects of the contact areas are more thoroughly discussed in Chapters 7.4 and 7.5.

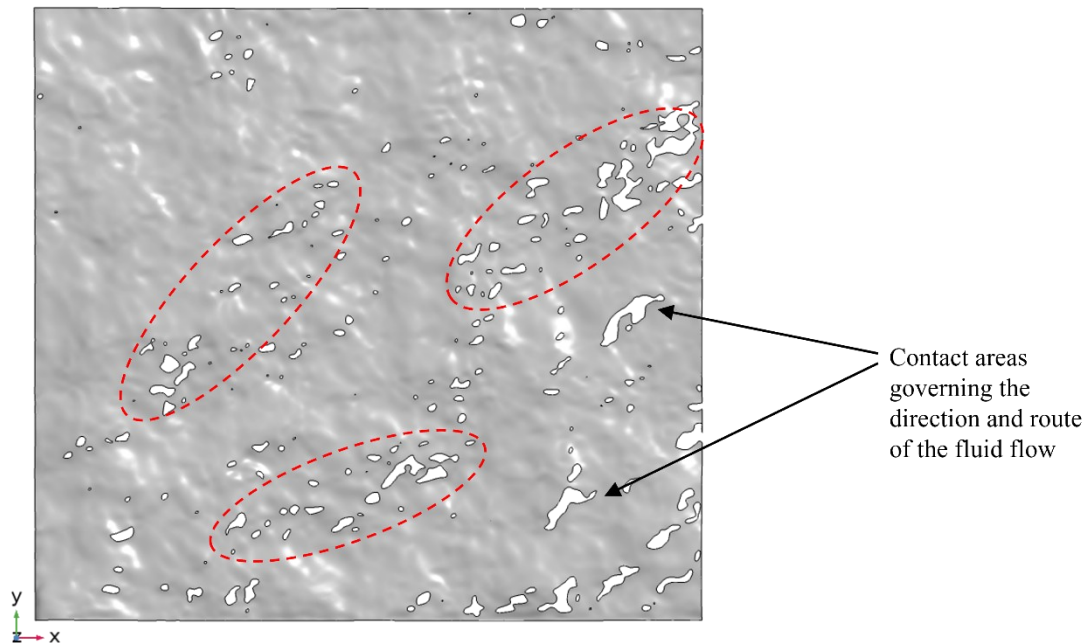


Figure 44. Fracture from bird perspective with contact areas indicated as white. Red dashed lines and black arrows are indicating the main zones that govern the route and behaviour of the fluid flow.

7.1 Validation of the numerical simulation model

Figure 45 and Figure 46 illustrate the pressure gradient as a function of flow rate at 0 MPa normal pressure with fluid flow through y-axis and x-axis, respectively. The relationship between the pressure gradient (∇P) and flow rate (Q) is polynomial. It means the fluid behaviour is nonlinear and rather than being laminar, the flow behaviour is turbulent and the data acquired from the simulation fits to the Forchheimer equation. There is very good positive correlation between the numerical simulation data and the experimental data by Torkan et al (2021). The correlation with fluid flow through x-axis seems to be slightly better than the correlation with fluid flow through y-axis. The correlation coefficient with fluid flow through y-axis is 9.9862E-01 and the correlation coefficient with fluid flow through x-axis is 9.9916E-01.

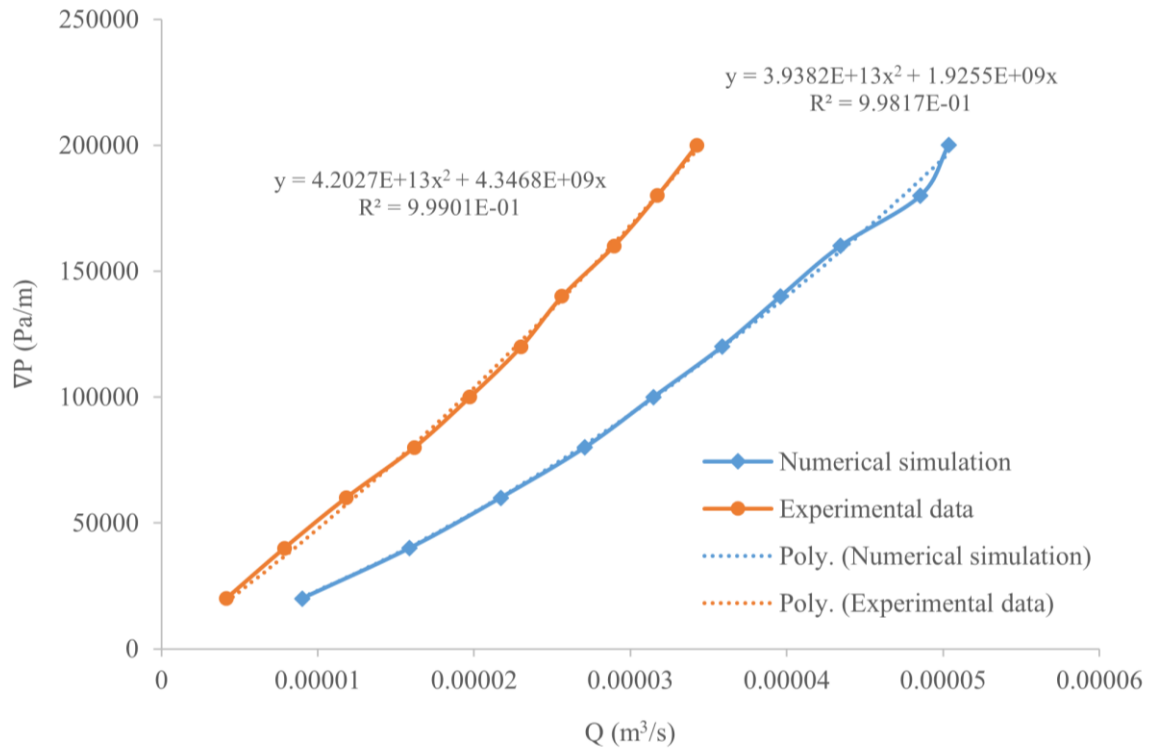


Figure 45. Outflow rate with fluid flow through y-axis at 0 MPa normal pressure compared with the experimental data. Dotted curves represent the results fitted with the Forchheimer equation. Numerical simulation in blue, experimental data by Torkan et al. (2021) in orange.

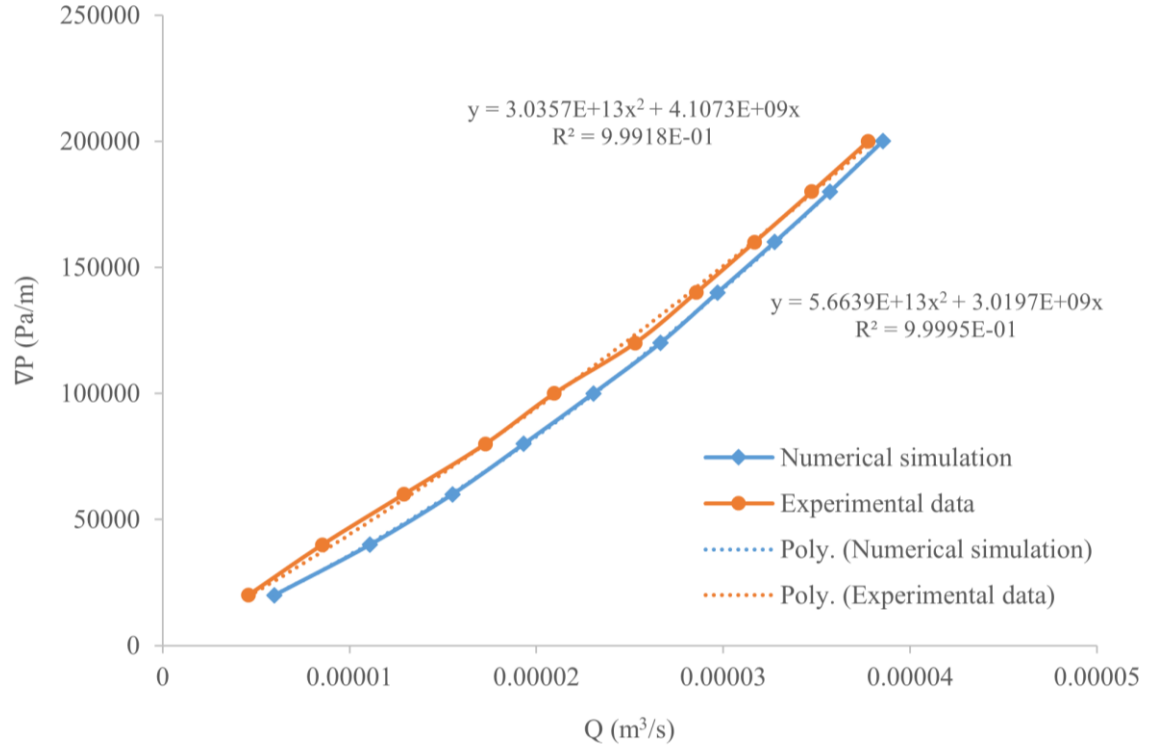


Figure 46. Outflow rate with fluid flow through x-axis at 0 MPa normal pressure compared with the experimental data. Dotted curves represent the results fitted with the Forchheimer equation. Numerical simulation in blue, experimental data by Torkan et al. (2021) in orange.

7.2 Physical and hydraulic aperture

The initial physical aperture obtained from the photogrammetry was 0.3309 mm. Table 5 presents the coefficients in the Forchheimer equation and the average hydraulic aperture with fluid flow through y-axis and x-axis. The hydraulic aperture acquired from the experimental data by Torkan et al. (2021) is presented for comparison. The coefficients in the Forchheimer equation were gained by using best-fit regression and the correspond to the coefficients by Torkan et al. (2021).

Table 5. Parameters obtained from Forchheimer equation for flow in fractured samples. E_h is the hydraulic aperture and a and b represent the coefficients in the Forchheimer equation. Hydraulic aperture acquired from the experimental data by Torkan et al. (2021) is presented for comparison.

	Numerical simulation			Experimental data
	a (kg/m ⁵ s)	b (kg/m ⁸)	e_h (mm)	e_h (mm)
Through y-axis	1.92135E+09	3.94529E+13	2.39168E-01	2.14201E-01
Through x-axis	3.01970E+09	5.66392E+13	2.14837E-01	2.18285E-01

Figure 47 presents the hydraulic aperture of the Sample 05 with fluid flow through y-axis and x-axis with inlet water pressures increasing from 5 kPa to 50 kPa with 5 kPa intervals. Hydraulic aperture decreases from 0.2679 mm to 0.2208 mm with fluid flow through y-axis as the inlet water pressure increases. Hydraulic aperture decreases from 0.2338 mm to 0.2019 mm with fluid flow through x-axis as the inlet water pressure increases. The hydraulic aperture with fluid flow through y-axis is approximately 0.0243 mm (11.26 %) larger than the hydraulic aperture with fluid flow through x-axis.

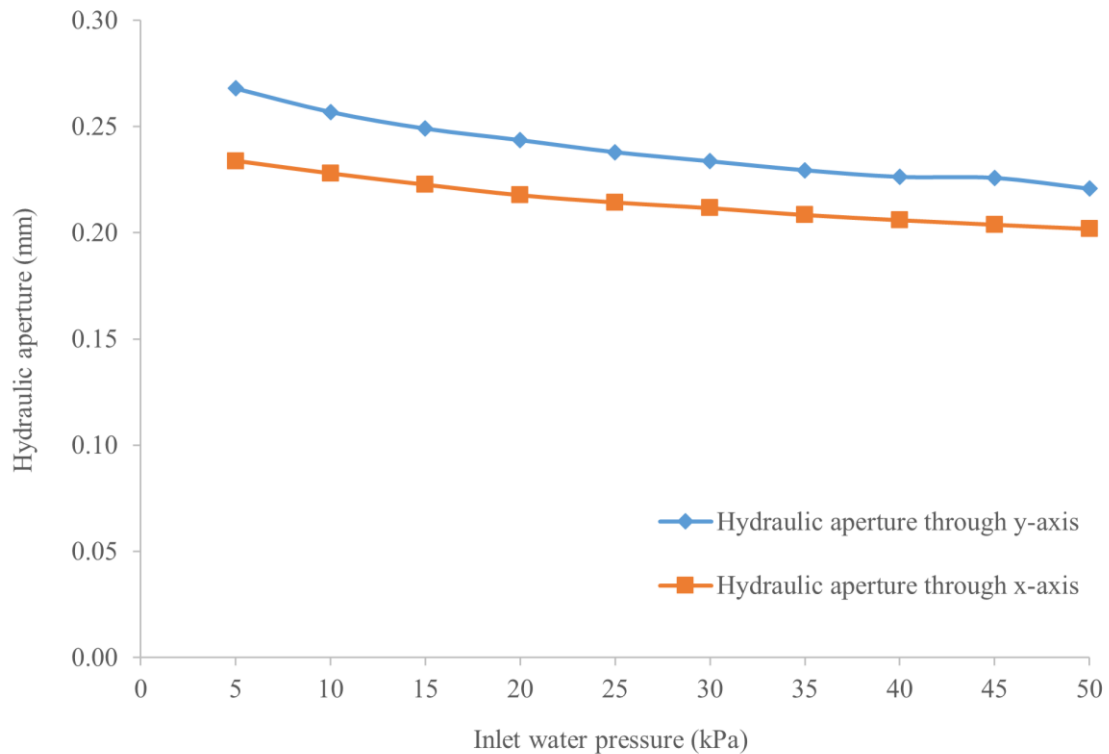


Figure 47. Hydraulic aperture obtained from numerical modelling, under increasing inlet water pressure. Fluid flow through y-axis in blue and fluid flow through x-axis in orange.

7.3 Flow velocity

Figure 48 presents the maximum fluid flow velocity inside the fracture during the flow simulation. The data is plotted separately with fluid flow through y-axis and x-axis with increasing water pressure from 5 to 50 kPa with 5 kPa intervals. The growth of flow velocity with the increase of water pressure is nonlinear. The increase in the maximum fluid velocity is faster at lower pressure gradients with fluid flow through both axes. The angle of curve of the fluid flow speed begins to transform more gradual as the pressure gradient increase.

The fluid flow velocity is faster with fluid flow through x-axis than with fluid flow through y-axis. Maximum fluid flow velocity is approximately 0.34 m/s (9%) faster with fluid flow through x-axis than with fluid flow through y-axis. Largest maximum fluid flow velocity variation is with inlet water pressures between 10 kPa to 25 kPa, after which the maximum fluid flow velocity difference begins to level.

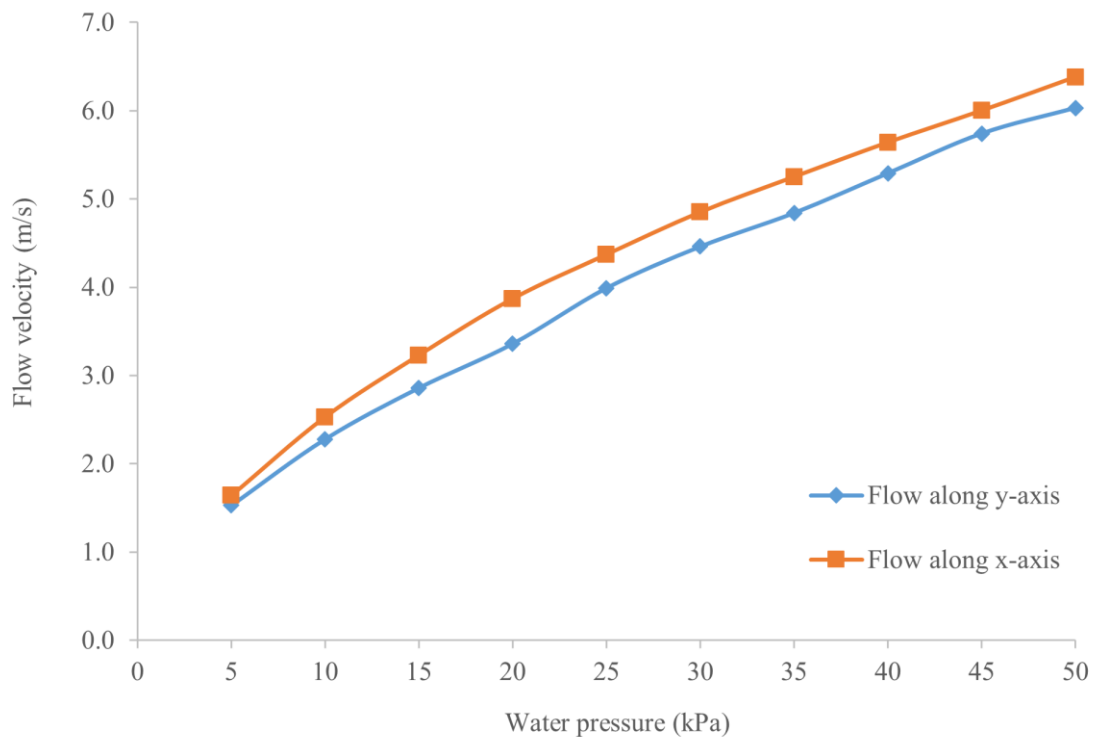


Figure 48. Maximum fluid flow velocity inside the fracture under increasing water pressure. Data form the fluid flow simulation. Fluid flow through y-axis in blue and fluid flow through x-axis in orange.

7.4 Streamlines

The simulated streamlines with fluid flow through x-axis and y-axis, under three different inlet water pressures, are depicted in Figure 49 and Figure 50. The streamline distribution develops channelization as the water pressure increases. The uniformity of the streamline distribution is also increased with the water pressure. The linearity of the streamlines generally increases with the water pressure. The contact areas inside the fracture affect the flow regime and the streamlines are more nonlinear around the contact areas. The channelization of the streamlines is more visible with fluid flow through x-axis (Figure 49) than with the fluid flow through y-axis (Figure 50). There is a minor channelization visible

with fluid flow through y-axis, but the majority of the channelization develops already when the 25 kPa inlet water pressure is achieved (Figure 50b), after which channelization almost decreases.

As suggested above, the flow through x-axis concentrates to the upper side of the fracture whereas the flow through y-axis concentrates in the center of the fracture. It would also seem that the contact areas are affecting the flow, especially with fluid flow through y-axis where the fluid flow is ‘pushed’ to the righthand side of the fracture by the contact areas. According to Chen et al. (2021), the streamlines form within the larger apertures and the locations of contact are the main cause of the deviations in the linear streamlines. Liu et al. (2021) studied the characteristics of fluid flow and solute transport in fracture model created on the basis of real fracture surface morphology data. One of the main results was that as the flow velocity increases, the fluid tends to flow to the dominant channel at the branch of the fracture and the fluid has different degrees of channeling (Liu et al. 2021).

Chen et al. (2021) studied flow characteristics in 3D rough rock fracture with geometry changes under different normal stresses using Navier-Stokes equation. Yin et al. (2020) studied fluid flow nonlinear fluid flow through rough fracture based on fractal theory and they concluded that the applicability of the Forccheimer equation is useful and practical method for describing the fluid flow through rough fractures.

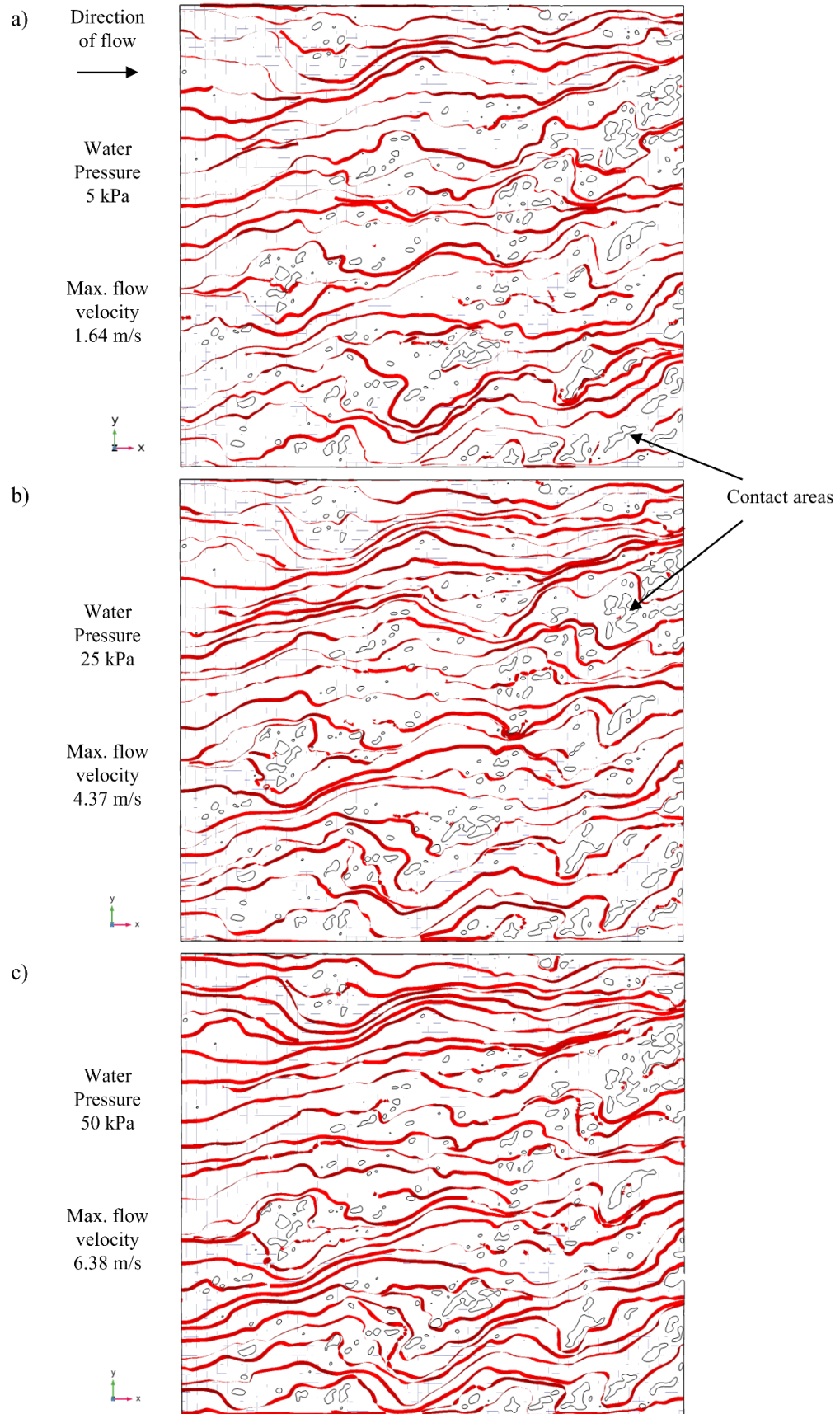


Figure 49. The simulated streamlines of the fluid flow with the flow through x-axis at inlet water pressures of a) 5, b) 25 and c) 50 KPa.

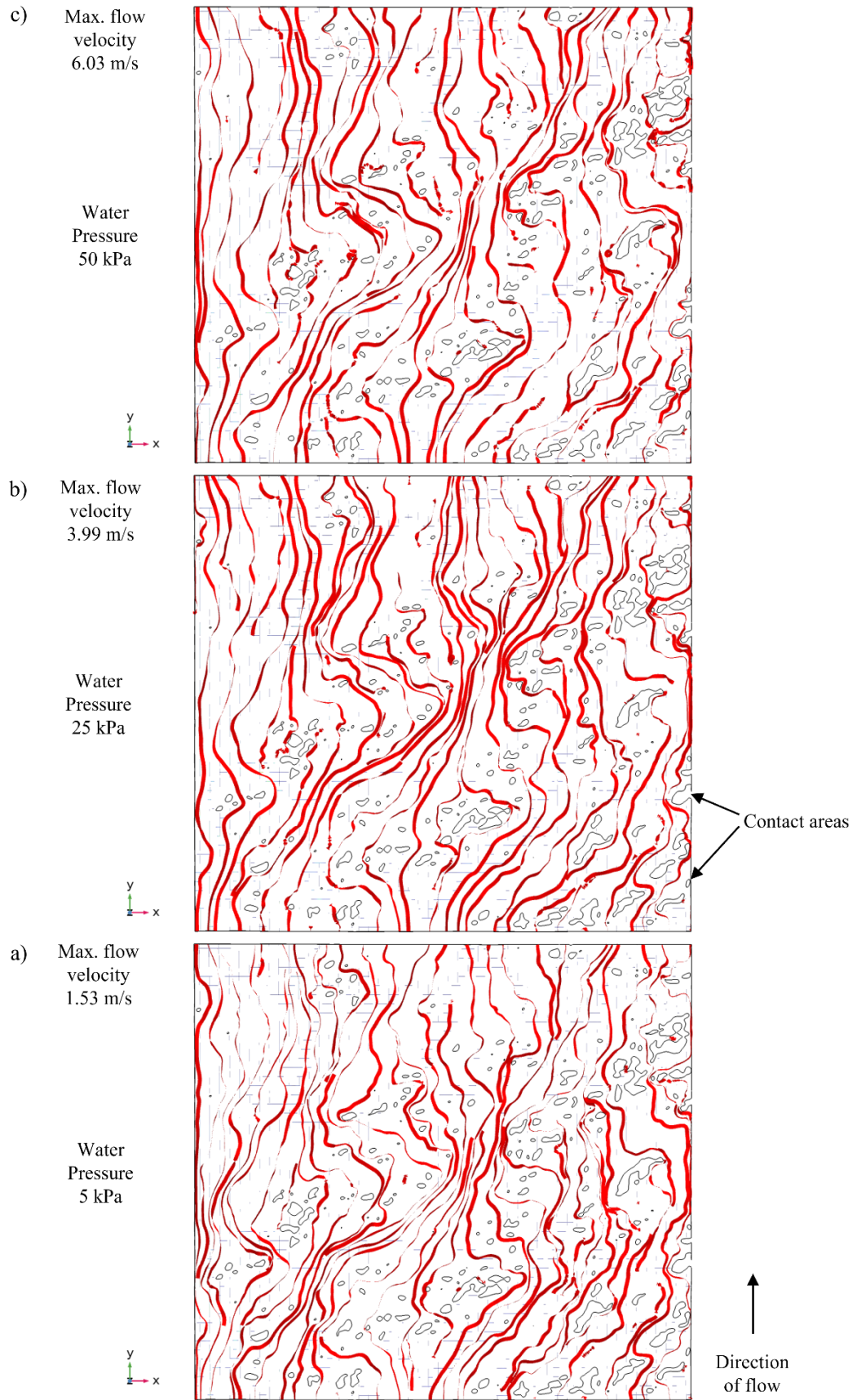


Figure 50. The simulated streamlines of the fluid flow with the flow through y-axis at inlet water pressures a) of 5, b) 25 and c) 50 KPa.

Figure 51 presents a detail of the streamlines around the contact areas with fluid flow through x-axis at inlet water pressure of 35 kPa. Although the fluid flow is laminar on larger scale, more detailed inspection reveals turbulent behaviour especially around the contact areas of the fracture. It would suggest that the contact areas of the fracture contribute highly to the flow regime inside the fracture.

Torkan et al. (2021) observed that after applying normal stress element to fracture with the fluid flow, the contact areas and void spaces increased which resulted in tortuosity behaviour of the fluid flow through the fracture. Applying normal stress to the fracture, decreases the physical aperture and creates new contact areas or enlarges the existing ones, blocking fluid flow and causing the streamlines to be more nonlinear. According to Torkan et al (2021), this illustrates that the fluid flow has nonlinear behaviour through a rough fracture.

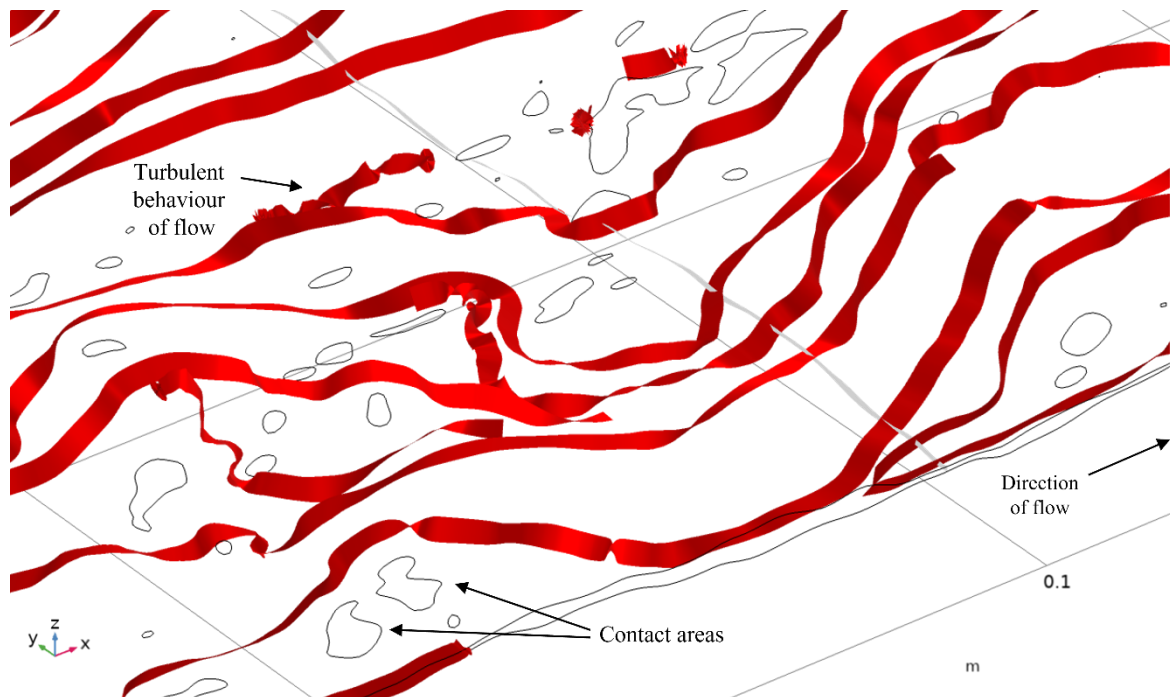


Figure 51. Detail of the turbulent behaviour of the streamlines around the contact areas with fluid flow through x-axis at inlet water pressure of 35 kPa.

7.5 Pressure contours

The simulated pressure contours with fluid flow through x-axis and y-axis, under three different inlet water pressures, are depicted in Figure 52 and Figure 53. The water pressure distribution along the fracture increases with the increase of water pressure. The nonlinearity of the pressure contours also increases with the water pressure.

Chen et al. (2021) discovered that higher inflow rates cause turbulent flow patterns that cause local fluctuation of water pressure although overall laminar regime still remains. The flow tests by Chen et al. (2021) were conducted in similar inlet water pressure conditions as the numerical simulations for this thesis.

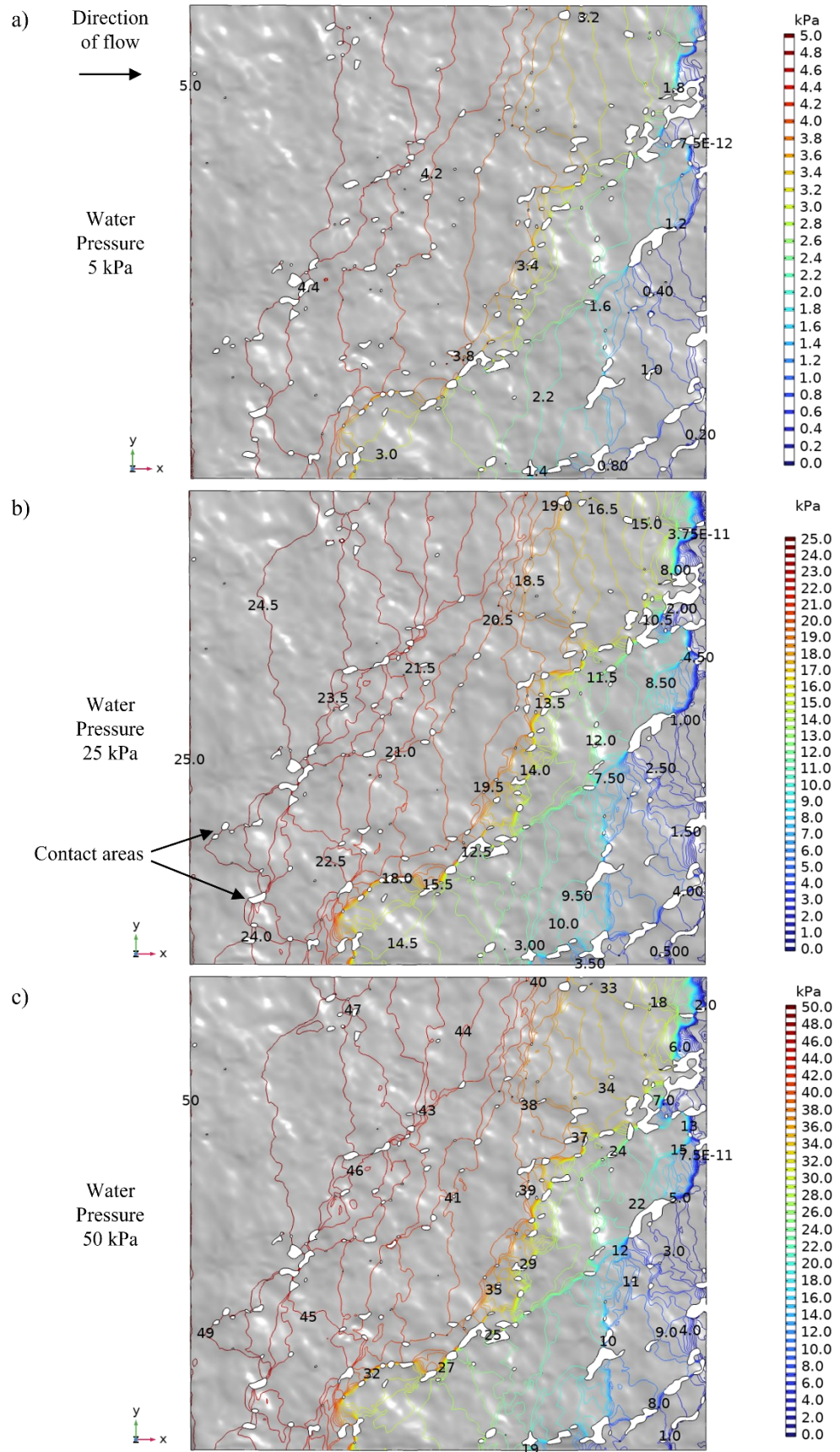


Figure 52. The simulated pressure contours of the fluid flow with the flow through x-axis at inlet water pressures of a) 5, b) 25 and c) 50 KPa.

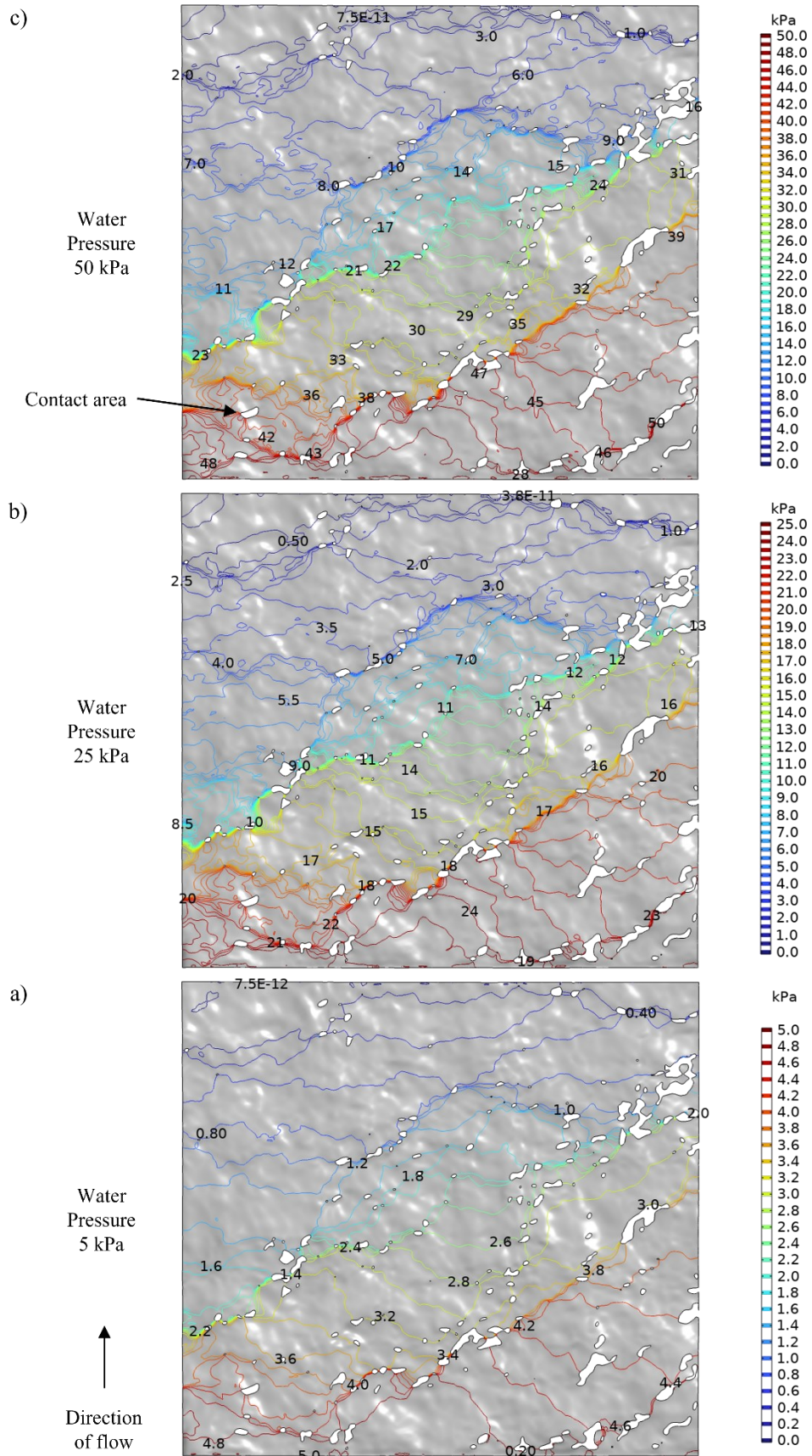


Figure 53. The simulated pressure contours of the fluid flow with the flow through y-axis at inlet water pressures of a) 5, b) 25 and c) 50 KPa.

Figure 54 presents a detail of the pressure contours in the inlet corner of the fracture with fluid flow through x-axis at inlet water pressure of 35 kPa. It is visible that the contact areas act as zones for the pressure to concentrate. The pressure accumulates on the inflow side of the contact area and after the contact area on the outflow side, the pressure starts to decrease until next more unified zone of contact areas is reached. Chen et al. (2021) concluded that the distribution of contact regions within fractures brings high water resistance and results in the reduced decay of the water pressure which is also seen in the results of this thesis.

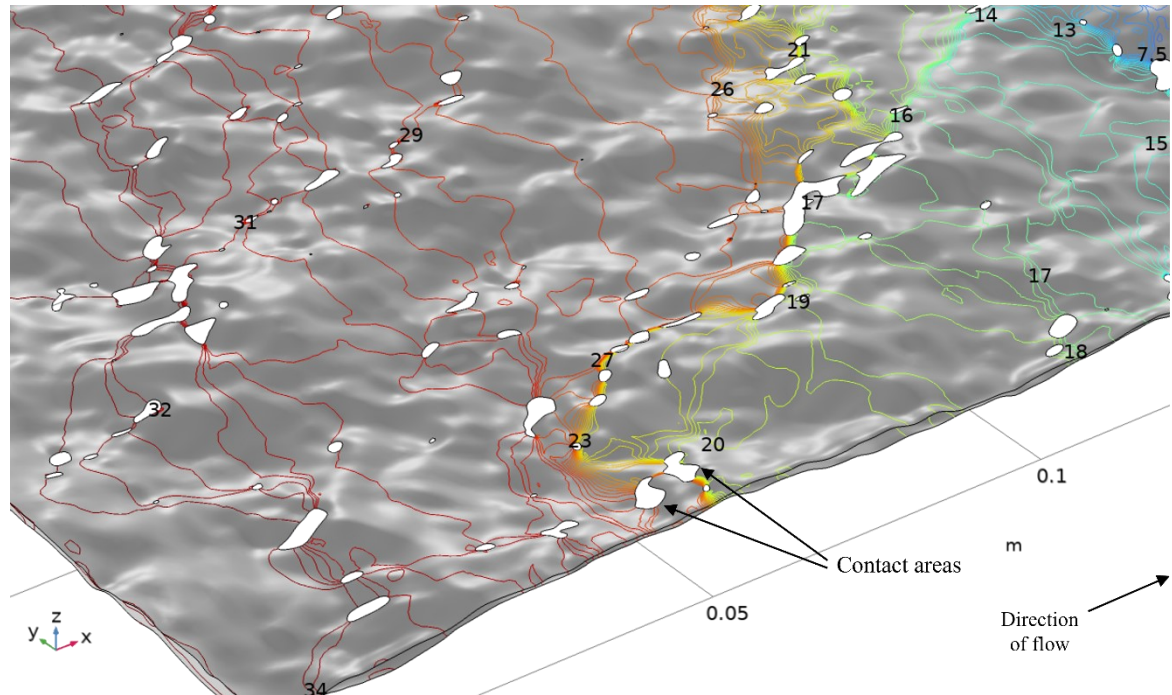


Figure 54. Detail of the behaviour of the pressure contours around the contact areas with fluid flow through x-axis at inlet water pressure of 35 kPa. The labels of the contours indicate the water pressure in kPa's.

8 Conclusion

The main objective of this thesis was to compare the influence of water pressure on fluid flow in rough rock fracture. The main study approach was numerical simulation. For that reason, a mathematical simulation model for fluid flow was created using the COMSOL Multiphysics software. A literature review preceded the numerical simulation. The second objective of this thesis was to compare the results of the numerical flow simulations with the experimental laboratory test results and validate the simulation model according to the laboratory results. Producing a repeatable workflow for numerical modelling of fluid flow in rock fractures was the third objective of this thesis. For that purpose, the workflow of creating the model for numerical simulation, was described in detail. Detailed description included the required steps in defining the geometry, the materials and the physical model with depiction of the meshing.

In this study, 20 fluid flow simulations were performed on fracture model created from photogrammetry of rock block with the size of $250\text{ mm} \times 250\text{ mm} \times 110\text{ mm}$, containing artificial tensile fracture. Finnish Kuru grey granite block was used as initial sample material. Fluid flow inside the fracture was simulated with fluid flow through x- and y-axis at increasing water pressure level. Simulated water pressures were from 5 kPa to 50 kPa with 5 kPa water pressure increment. Fluid flow simulations were carried away at normal stress conditions of 0 MPa. The numerical model was successfully verified against experimental laboratory work. Numerical data seems to correspond very well with the experimental laboratory tests which means that the fluid flow through rough fracture can be simulated by using numerical methods presented in this thesis. Hydraulic aperture calculated from the numerical simulation results corresponds also with the experimental data.

The numerical simulation results show that the relationship between water pressure gradient and the flow rate is nonlinear, indicating turbulent flow behaviour. The channelling effect of the fluid flow increases with the increase of water pressure. It means that the fluid flow moves more straightforwardly through the fracture when the water pressure and flow rate increases. Pressure distribution along the fracture also increases with the increase of water pressure. The scale of the variation of the measured pressures throughout the fracture grows larger with increased water pressure. The growth of fluid flow velocity inside the fracture with the increase of water pressure is nonlinear and the growth rate of the fluid flow velocity decreases as the inlet water pressure increases. Hydraulic aperture decreases also as the inlet water pressure increases. Hydraulic aperture is slightly larger with fluid flow through y-axis than with fluid flow through x-axis and the fluid flow velocity is slightly faster with fluid flow through x-axis than with fluid flow through y-axis.

The numerical simulation for this thesis was made for small-scale rock fracture. For further research, upscaling the simulation model to correspond the size of the rock fractures in bedrock would provide more accurate results to support in designing underground rock engineering applications. This thesis didn't consider the effect of normal stress to the fluid flow and fracture aperture. Also, higher water pressures were only shortly discussed. Therefore, especially normal stress and higher water pressure, corresponding the water pressure levels found in nature, should be taken in consideration in further studies.

Numerical simulation is a powerful tool when assessing the fluid flow properties of the bedrock. Numerical simulation can also be a useful when evaluating the hydraulic aperture of a fracture. As an overall assessment of the numerical simulation the fluid flow analyses

of this thesis indicates that it could be used to characterize to flow properties of fractured rock. The method presented in this thesis can be used as a tool in evaluating different methods and implementation of underground rock engineering applications.

References

- Baghbanan, A. & Jing, L. 2007.** Hydraulic properties of fractured rock masses with correlated fracture length and aperture. *International Journal of Rock Mechanics and Mining Sciences*, 44(5), 704-719.
- Barton, N. 1973.** Review of a new shear-strength criterion for rock joints. *Engineering geology*, 7(4), 287-332.
- Barton, N.R. & Choubey, V. 1977.** The shear strength of rock joints in theory and practice. *Rock Mechanics*. Vol. 10:1-2. S. 1-54.
- Barton, N., Bandis, S. & Bakhtar, K. 1985.** Strength, deformation and conductivity coupling of rock joints. In *International journal of rock mechanics and mining sciences & geomechanics abstracts* (Vol. 22, No. 3, pp. 121-140). Pergamon.
- Bear, J. 1972.** Dynamics of fluids in porous media. Courier Corporation.
- Boussinesq, J. 1868.** Mémoire sur l'influence des Frottements dans les Mouvements Réguliers des Fluids. [Thesis about the influence of friction within the steady flow of fluids]. *J. Math. Pures Appl*, 13(377-424), 21.
- Brown, S., Caprihan, A. & Hardy, R. 1998.** Experimental observation of fluid flow channels in a single fracture. *Journal of Geophysical Research: Solid Earth*, 103(B3), 5125-5132.
- Brown, S. R. 1987.** Fluid flow through rock joints: the effect of surface roughness. *Journal of Geophysical Research: Solid Earth*, 92(B2), 1337-1347.
- Chen, Y., Liang, W., Lian, H., Yang, J. & Nguyen, V. P. 2017.** Experimental study on the effect of fracture geometric characteristics on the permeability in deformable rough-walled fractures. *International Journal of Rock Mechanics and Mining Sciences*, 98, 121-140.
- Chen, Y., Selvadurai, A. P. S. & Zhao, Z. 2021.** Modelling of flow characteristics in 3D rough rock fracture with geometry changes under confining stresses. *Computers and Geotechnics*, 130, 103910.
- Comsol. 2021.** <https://www.comsol.com/> (accessed 30th December 2021).
- De Marsily, G. 1986.** Quantitative hydrogeology. Paris School of Mines, Fontainebleau.
- Detwiler, R. L., Rajaram, H. & Glass, R. J. 2000.** Solute transport in variable-aperture fractures: An investigation of the relative importance of Taylor dispersion and macrodispersion. *Water Resources Research*, 36(7), 1611-1625.
- Develi, K. & Babadagli, T. 2015.** Experimental and visual analysis of single-phase flow through rough fracture replicas. *International Journal of Rock Mechanics and Mining Sciences*, 73, 139-155.

Dzugala, M. 2016. Pull experiment to validate photogrammetrically predicted friction angle of rock discontinuities. MSc thesis. Aalto University. 116+6 p.

Esaki, T., Du, S., Jiang, Y., Wada, Y. & Mitani, Y. 1998. Relation between mechanical and hydraulic apertures during shear-flow coupling test. In Proceedings of the 10th Japan Symposium on Rock Mechanics, Osaka, Japan (pp. 22-23).

Hakami, E. & Larsson, E. 1996. Aperture measurements and flow experiments on a single natural fracture. In International Journal of Rock Mechanics and Mining Sciences & Geomechanics Abstracts (Vol. 33, No. 4, pp. 395-404). Pergamon.

Hakami E. 1995. Aperture distribution of rock fractures. Doctoral thesis, Division of Engineering Geology, Royal Institute of Technology, Stockholm.

Indraratna, B. & Ranjith, P. 2001. Hydromechanical aspects and unsaturated flow in jointed rock. Lisse;: AA Balkema publishers.

International Society for Rock Mechanics Commission on Standardisation of Laboratory and Field Tests. 1978. Suggested methods for the quantitative description of discontinuities in rock masses. Int. J. Rock Mech. Min. Sci. & Geomech. Abstr. Vol. 15. S. 319-368.

Ishibashi, T., Watanabe, N., Hirano, N., Okamoto, A. & Tsuchiya, N. 2015. Beyond-laboratory-scale prediction for channeling flows through subsurface rock fractures with heterogeneous aperture distributions revealed by laboratory evaluation. Journal of Geophysical Research: Solid Earth, 120(1), 106-124.

Javadi, M., Sharifzadeh, M. & Shahriar, K. 2010. A new geometrical model for nonlinear fluid flow through rough fractures. Journal of Hydrology, 389(1-2), 18-30.

Jing, L. 2003. A review of techniques, advances and outstanding issues in numerical modelling for rock mechanics and rock engineering. International Journal of Rock Mechanics and Mining Sciences, 40(3), 283-353.

Jing, L. & Stephansson, O. 2007. Fundamentals of discrete element methods for rock engineering: theory and applications, Vol. 85. Elsevier.

Kallio, P. 2015. Rakopinnan karkeuden mittaaminen fotogrammetrisesti. [B.Sc. thesis], Aalto University, School of Engineering, Espoo, Finland

Keller, A. 1998. High resolution, non-destructive measurement and characterization of fracture apertures. International Journal of Rock Mechanics and Mining Sciences, 35(8), pp. 1037-1050.

Kong, B. & Chen, S. 2018. Numerical simulation of fluid flow and sensitivity analysis in rough-wall fractures. Journal of Petroleum Science and Engineering, 168, 546-561.

- Krantz, R. L., Frankel, A. D., Engelder, T. & Scholz, C. H. 1979.** The permeability of whole and jointed Barre granite. In *International Journal of Rock Mechanics and Mining Sciences & Geomechanics Abstracts* (Vol. 16, No. 4, pp. 225-234). Pergamon.
- Lee, H. S. & Cho, T. F. 2002.** Hydraulic characteristics of rough fractures in linear flow under normal and shear load. *Rock Mechanics and Rock Engineering*, 35(4), 299-318.
- Li, B., Jiang, Y., Koyama, T., Jing, L. & Tanabashi, Y. 2008.** Experimental study of the hydro-mechanical behaviour of rock joints using a parallel-plate model containing contact areas and artificial fractures. *International Journal of Rock Mechanics and Mining Sciences*, 45(3), 362-375.
- Liu, X., Chen, D., Li, M., Li, Y. & Yang, X. (2021).** Characteristics of Fluid Flow and Solute Transport in Multicrossed Rough Rock Fractures Based on Three-Dimensional Simulation. In *IOP Conference Series: Earth and Environmental Science* (Vol. 861, No. 7, p. 072095). IOP Publishing.
- Louis, C. L. 1974.** Introduction to rock hydraulics. *BULL BRGM*, III, (4).
- Min, K. B., Rutqvist, J., Tsang, C. F. & Jing, L. 2004.** Stress-dependent permeability of fractured rock masses: a numerical study. *International Journal of Rock Mechanics and Mining Sciences*, 41(7), 1191-1210.
- Mohanty, S. & Hsiung, S. 2011.** An experimental investigation of single fracture flow behaviour under normal and shear loads. Prepared for: U.S. Nuclear Regulatory Commission Contract No. NRC-02-07-006. Center for Nuclear Waste Regulatory Analyses.
- Noorishad, J. & Tsang, C. F. 1996.** Coupled thermohydroelasticity phenomena in variably saturated fractured porous rocks--formulation and numerical solution. In *Developments in geotechnical engineering* (Vol. 79, pp. 93-134). Elsevier.
- Plouraboué, F., Kurowski, P., Hulin, J. P., Roux, S. & Schmittbuhl, J. 1995.** Aperture of rough cracks. *Physical review E*, 51(3), 1675.
- Qian, X., Xia, C., Gui, Y., Zhuang, X. & Yu, Q. 2019.** Study on flow regimes and seepage models through open rough-walled rock joints under high hydraulic gradient. *Hydrogeology Journal*, 27(4), 1329-1343.
- Raven, K. G. & Gale, J. E. 1985.** Water flow in a natural rock fracture as a function of stress and sample size. In *International Journal of Rock Mechanics and Mining Sciences & Geomechanics Abstracts* Vol. 22, No. 4, pp. 251-261. Pergamon.
- Rong, G., Yang, J., Cheng, L. & Zhou, C. 2016.** Laboratory investigation of nonlinear flow characteristics in rough fractures during shear process. *Journal of hydrology*, 541, 1385-1394.
- Rutqvist, J. & Stephansson, O. 2003.** The role of hydromechanical coupling in fractured rock engineering. *Hydrogeology Journal*, 11(1), 7-40.

Schrauf, T. W. & Evans, D. D. 1986. Laboratory studies of gas flow through a single natural fracture. *Water Resources Research*, 22(7), 1038-1050.

Schlichting, H. 1968. Boundary-layer theory: Translated by J. Kestin.

Schultz, R. A., Parashar, R. & Reeves, D. M. 2010. Cubic law with aperture-length correlation: implications for network scale fluid flow. *Hydrogeology Journal*, 18(4), 851-862.

Şen, Z. & Sadagah, B. H. 2002. Probabilistic horizontal stress ratios in rock. *Mathematical geology*, 34(7), 845-855.

Singh, K. K., Singh, D. N. & Ranjith, P. G. 2015. Laboratory simulation of flow through single fractured granite. *Rock Mechanics and Rock Engineering*, 48(3), 987-1000.

Singhal, B. B. S. & Gupta, R. P. 2010. Applied hydrogeology of fractured rocks. Springer Science & Business Media.

Sirkiä, J. 2015. Requirements for initial data in photogrammetric recording of rock joint surfaces [M.Sc. thesis], Aalto University, School of Engineering, Espoo, Finland.

Snow, D. T. 1965. A parallel plate model of fractured permeable media. Ph. D. Thesis, University of California.

Steele, A. & Lerner, D. N. 2001. Predictive modelling of NAPL injection tests in variable aperture spatially correlated fractures. *Journal of contaminant hydrology*, 49(3-4), 287-310.

Stoll, M., Huber, F. M., Trumm, M., Enzmann, F., Meinel, D., Wenka, A., Schill, E. & Schäfer, T. 2019. Experimental and numerical investigations on the effect of fracture geometry and fracture aperture distribution on flow and solute transport in natural fractures. *Journal of contaminant hydrology*, 221, 82-97.

Torkan, M., Uotinen, L., Nieminen, V. & Rinne, M. 2021. Photogrammetry based characterization of hydro-mechanical properties of a rock fracture. In *IOP Conference Series: Earth and Environmental Science* (Vol. 833, No. 1, p. 012019). IOP Publishing.

Tsang, Y. W. & Witherspoon, P. A. 1981. Hydromechanical behaviour of a deformable rock fracture subject to normal stress. *Journal of Geophysical Research: Solid Earth*, 86(B10), 9287-9298.

Tsang, Y. W. 1992. Usage of “equivalent apertures” for rock fractures as derived from hydraulic and tracer tests. *Water Resources Research*, 28(5), 1451-1455.

Uotinen, L., Torkan, M., Janiszewski, M., Baghbanan, A., Nieminen, V. & Rinne, M. 2020. Characterization of hydro-mechanical properties of rock fractures using steady state flow tests. *Eurock 2020: Hard rock engineering: Proceedings of the International Symposium of the International Society for Rock Mechanics*, Eurock 2020, Trondheim, Norway, 14-19 June 2020.

Van Golf-Racht, T. D. 1982. Fundamentals of fractured reservoir engineering. Elsevier Science. 732 p.

Wang, C., Jiang, Y., Luan, H., Liu, J. & Sugimoto, S. 2019. Experimental Study on the Shear-Flow Coupled Behaviour of Tension Fractures Under Constant Normal Stiffness Boundary Conditions. *Processes*, 7(2), 57.

Xiong, F., Jiang, Q. & Chen, M. 2018. Numerical investigation on hydraulic properties of artificial-splitting granite fractures during normal and shear deformations. *Geofluids*, 2018.

Yin, P., Zhao, C., Ma, J., Yan, C. & Huang, L. 2020. Experimental study of non-linear fluid flow through rough fracture based on fractal theory and 3D printing technique. *International Journal of Rock Mechanics and Mining Sciences*, 129, 104293.

Zhang, Z. & Nemcik, J. 2013. Fluid flow regimes and nonlinear flow characteristics in deformable rock fractures. *Journal of Hydrology*, 477, 139-151.

Zhao, J. & Brown, E. T. 1992. Hydro-thermo-mechanical properties of joints in the Carnmenellis granite. *Quarterly Journal of Engineering Geology and Hydrogeology*, 25(4), 279-290.

Zhao, Z., Jing, L., Neretnieks, I. & Moreno, L. 2011. Numerical modelling of stress effects on solute transport in fractured rocks. *Computers and Geotechnics*, 38(2), 113-126.

Zhao, Z. 2014. On the heat transfer coefficient between rock fracture walls and flowing fluid. *Computers and Geotechnics*, 59, 105-111.

Zimmerman, R. W., Chen, D. W. & Cook, N. G. 1992. The effect of contact area on the permeability of fractures. *Journal of Hydrology*, 139(1-4), 79-96.

Zimmerman, R. W. & Bodvarsson, G. S. 1996. Hydraulic conductivity of rock fractures. *Transport in porous media*, 23(1), pp. 1-30.

Zimmerman, R. W., Al-Yaarubi, A., Pain, C. C. & Grattoni, C. A. 2004. Non-linear regimes of fluid flow in rock fractures. *International Journal of Rock Mechanics and Mining Sciences*, 41, 163-169.

Zimmerman, R. & Main, I. 2004. Hydromechanical behaviour of fractured rocks. *International Geophysics Series*, 89, pp. 363-422.

Zou, L., Jing, L. & Cvetkovic, V. 2017. Shear-enhanced nonlinear flow in rough-walled rock fractures. *International Journal of Rock Mechanics and Mining Sciences*, 97, 33-45.

Appendix

A Tabulated results

. Fluid flow rate inside the fracture along y-axis.

Water pressure	Pressure gradient ∇P	Flow rate Q
kPa	Pa/m	m³/s
5	20 000	9.01E-06
10	40 000	1.59E-05
15	60 000	2.17E-05
20	80 000	2.71E-05
25	100 000	3.16E-05
30	120 000	3.59E-05
35	140 000	3.96E-05
40	160 000	4.34E-05
45	180 000	4.86E-05
50	200 000	5.04E-05

Table 6. Fluid flow rate inside the fracture along x-axis.

Water pressure	Pressure gradient ∇P	Flow rate Q
kPa	Pa/m	m³/s
5	20 000	5.99E-06
10	40 000	1.11E-05
15	60 000	1.55E-05
20	80 000	1.93E-05
25	100 000	2.30E-05
30	120 000	2.66E-05
35	140 000	2.97E-05
40	160 000	3.27E-05
45	180 000	3.57E-05
50	200 000	3.85E-05

Table 7. Fluid flow velocity inside the fracture along y-axis with increasing water pressures.

Water pressure	Flow velocity
kPa	m/s
5	1.53
10	2.28
15	2.86
20	3.36
25	3.99
30	4.46
35	4.84
40	5.29
45	5.74
50	6.03

Table 8. Fluid flow velocity inside the fracture along x -axis with increas water pressures.

Water pressure	Flow velocity
kPa	m/s
5	1.64
10	2.53
15	3.23
20	3.87
25	4.37
30	4.85
35	5.25
40	5.64
45	6.00
50	6.38

Table 9. Hydraulic aperture under increasing inlet water pressure through y-axis and x-axis.

Condition	Hydraulic aperture	
Inlet water pressure	e_h through y-axis	e_h through x-axis
kPa	mm	mm
5	0.2679	0.2338
10	0.2569	0.2280
15	0.2491	0.2227
20	0.2437	0.2177
25	0.2380	0.2143
30	0.2337	0.2116
35	0.2295	0.2085
40	0.2263	0.2060
45	0.2259	0.2039
50	0.2208	0.2019